BRNO UNIVERSITY OF TECHNOLOGY

VYSOKÉ UČENÍ TECHNICKÉ V BRNĚ

FACULTY OF MECHANICAL ENGINEERING

FAKULTA STROJNÍHO INŽENÝRSTVÍ

INSTITUTE OF MANUFACTURING TECHNOLOGY

ÚSTAV STROJÍRENSKÉ TECHNOLOGIE

ANALYSIS OF INCONEL 625 WELD LAYER PRODUCED BY MIG-CMT

ANALÝZA NÁVAROVÉ VRSTVY INCONEL 625 VYTVOŘENOU METODOU MIG-CMT

MASTER'S THESIS

DIPLOMOVÁ PRÁCE

AUTHOR — Bc. Daniel Chrást

AUTOR PRÁCE

SUPERVISOR — Ing. Jaroslav Kubíček, IWE

VEDOUCÍ PRÁCE

BRNO 2023

BRNO UNIVERSITY OF TECHNOLOGY
FACULTY OF MECHANICAL ENGINEERING

Assignment Master's Thesis

Institut:	Institute of Manufacturing Technology
Student:	**Bc. Daniel Chrást**
Degree programm:	Manufacturing Technology
Branch:	Manufacturing Technology
Supervisor:	**Ing. Jaroslav Kubíček, IWE**
Academic year:	2022/23

As provided for by the Act No. 111/98 Coll. on higher education institutions and the BUT Study and Examination Regulations, the director of the Institute hereby assigns the following topic of Master's Thesis:

Analysis of Inconel 625 weld layer produced by MIG–CMT

Recommended bibliography:

ASM Handbook Welding, Brazing and Soldering. Volume 6. 10th editon. Materials Park, Ohio: ASM International, 2016. ISBN 978-0871703828.

KOLEKTIV AUTORŮ. Materiály a jejich svařitelnost, 1. vyd. Zeross, Ostrava 2001, 292s. ISBN 80-85771-85-3.

KOLEKTIV AUTORŮ. Technologie svařování a zařízení, 1. vyd. Zeross, Ostrava 2001, 395s. ISBN 80-85771-81-0.

KOLEKTIV AUTORŮ. Navrhování a posuzování svařovaných konstrukcí a tlakových zařízení, 1. vyd. Zeross, Ostrava 1999, 249s. ISBN 80-85771-70-5.

KOLEKTIV AUTORŮ. Výroba a aplikované inženýrství ve svařování, 1. vyd. Zeross, Ostrava 2000, 214s. ISBN 80-85771-72-1.

ONDREJČEK, Peter. Zváranie ocelí v ochrane plynov taviacou sa elektródou, 1. vyd. ETERNA PRESS s.r.o. Bratislava 2003, ISBN 80-968359-5.

Deadline for submission Master's Thesis is given by the Schedule of the Academic year 2022/23

In Brno,

L. S.

Ing. Jan Zouhar, Ph.D. Director of the Institute	doc. Ing. Jiří Hlinka, Ph.D. FME dean

ABSTRACT

Inconel 625 to 16Mo3 base material welds are used in energy industry in waste incineration plants to increase lifetime of membrane walls. The welds are formed using MIG-CMT method. Macrostructure and microstructure analyses were carried out using Apreo 2 SEM microscope, and chemical composition analysis of welds was also carried out using iSpark OES spectrometer. Finally, analyses of selected mechanical properties, namely microhardness and ductility, were performed.

Key words

Inconel 625, mebrane walls, CMT, welding, microstructure, OES, SEM, microhardness, ductility

ABSTRAKT

Návary z materiálu Inconel 625 na základní materiál 16Mo3 slouží v energetickém průmyslu u spaloven odpadu pro zvýšení životnosti membránových stěn. Návarové housenky jsou vytvořeny pomocí metody MIG-CMT. Byly provedeny analýzy makrostruktury a mikrostruktury za použití SEM mikroskopu Apreo 2, dále byla provedena analýza chemické složení návarové housenky za použití OES spektrometru ISpark. Nakonec byly provedeny analýzy vybraných mechanických vlastností, konkrétně mikrotvrdost a tažnost.

Klíčová slova

Inconel 625, membránové stěny, CMT, navařování, mikrostruktura, OES, SEM, mikrotvrdost, tažnost

ROZŠÍŘENÝ ABSTRAKT

Tvorba odpadu patří k lidské existenci od nepaměti. Již vypalování hlíny do forem, ve které se v pravěku tvořily keramické nádoby, mělo první dopad na přírodu, jelikož keramické střepy se v archeologických vykopávkách stále nacházejí. S postupem času a pokroku přišlo lidstvo na to, jak zpracovávat jednotlivé kovy, mezi které patří měď a železo. V průběhu staletí se lidé naučili upravovat materiály do formy slitin, jako je bronz nebo ocel. Tyto materiály se v přírodě nevyskytují a došlo tak k další kontaminaci půdy pomocí kovů. Mezi materiály, které vydrží v přírodě nejdéle, patří sklo. Sklo se používá již dlouhá tisíciletí a je velmi inertní vůči vlivům, jež by ostatní materiály dokázaly rozložit. S pokrokem dokázalo lidstvo vytvořit sklo za pomoci chemických látek, které ještě prodlužují životnost skelného materiálu. Mezi největší objevy v materiálovém odvětví patří objev výroby a zpracování plastů. Jedná se o relativně nový materiál, první plast byl vyroben v roce 1907. Plasty jsou v dnešní době hojně využívány ve všech odvětvích průmyslu. Jejich výroba je levná, rychlá a relativně jednoduchá, proto plast patří k nejvíce využívaným materiálům na světě. Dopad na životní prostředí má však enormní, a to z důvodu jeho složité rozložitelnosti jak v půdě, tak ve vodě. V dnešní době pokračuje vývoj nových plastů, které mohou být degradabilní v přírodním prostředí, ale drtivá většina objemu plastu, jenž je produkován, velmi znečišťuje naši planetu. Mezi nové odvětví, které znečišťuje naši planetu, spadá elektronický průmysl. Elektronické zařízení obsahuje velké množství různých kovů a plastů, jež jsou těžko rozložitelné. Dále jsou používané nebezpečné látky jako je rtuť nebo kadmium, které mohou způsobit znečištění životního prostředí. Odpad, který lidstvo produkuje od svého vzniku, je biologický odpad ve formě odpadků vzniklých z potravin nebo vylučování.

V dnešní době se nakládá s odpadem různými způsoby. Ve vyspělých zemích, jako je například Německo nebo Dánsko, se ve velké míře spaluje odpad ve spalovnách a vzniklé teplo se využívá pro tvorbu elektrické energie. Česká republika patří mezi skupinu zemí, které odpad ukládají na skládkách a spalují v přibližném poměru půl na půl. V poslední řadě jsou zde státy, jako je například Malta, která veškerý odpad ukládá do zemních skládek.

Spalování odpadu není omezeno pouze na komunální odpad, ale zahrnuje i průmyslový a zdravotnický odpad a odpad z čistíren odpadních vod. Spalování odpadu při nízkých teplotách se provádí u běžného komunálního odpadu, zatímco nebezpečný odpad se spaluje při velmi vysokých teplotách, často v cementárenských pecích. Tento proces je důležitý z hlediska udržitelnosti, protože umožňuje využití odpadu jako zdroje energie a snížení potřeby fosilních paliv. Provoz spalovacích zařízení může být problematický kvůli rozmanitosti odpadu a agresivnímu složení spalin. Pro tento účel se používají kotle s membránovými stěnami, jež jsou schopné vyrábět páru pro turbíny. Prodloužení životnosti membránových stěn může být realizováno použitím korozivzdorných a žáruvzdorných ocelí. Dále může být životnost prodloužena použitím navařených niklových slitin.

Technologie navařování je modifikací technologie svařování. V případě této technologie dochází k nanášení přídavného materiálu na materiál základní. Děje se tak z několika důvodů. Ať už to je z důvodu zvýšení životnosti součástky z hlediska korozní odolnosti, žárové odolnosti nebo kvůli zvýšení odolnosti vůči mechanickému opotřebení. Nejčastěji se nanášejí materiály s výrazně odlišným chemickým složením nebo mechanickými vlastnostmi. Často používané jsou materiály na bázi neželezných kovů, jako například chrom, nikl nebo molybden. Tyto materiály se používají ve formě superslitin.

Základním požadavkem je minimální promísení obou materiálů, a tím dochází k zamezení degradace návarového materiálu. Mezi technologie, které se používají pro vytvoření těchto návarů, patří progresivní metoda MIG-CMT. Tato metoda oproti klasické metodě MIG používá modifikaci s názvem cold-metal-transfer. Tato modifikace svařování tavící se elektrodou v ochranné atmosféře kombinuje horkou fázi hoření oblouku, kdy se taví drát i ZM se studenou částí procesu, kdy se při kontaktu nataveného drátu s tavnou lázní snižuje intenzita proudu a drát se vrací do hubice. Tím je podpořeno oddělení kapky bez rozstřiku a s nízkou hodnotou vneseného tepla do svaru. Celý proces je řízen digitálně a zpětný pohyb drátu probíhá s frekvencí až 130 Hz. Rozdíl mezi technologiemi je v možnosti ovlivňování zředění. Celý proces navařování je řízen za pomocí zdroje, jenž je schopen všechny požadavky, které jsou požadovány pro správné navaření, splnit. Zdroje od firmy Fronius obsahují software schopný nastavit všechny potřebné parametry, jichž mohou být až desítky, takže dojde k minimalizaci natavení základního materiálu. Důležitý je kontaktní úhel mezi základním materiálem a návarem. Při vypouklém tvaru je návar vysoký, což může být příhodné pro zajištění velké tloušťky ochranného návaru. Pro rovnoměrné navázání svarových housenek je zapotřebí kontaktní úhel alespoň 115°. Pokud je úhel menší, tak není reálné vytvořit homogenní celistvý návar, jelikož je vytvářený návar příliš vysoký.

Spalování komunálního odpadu tvoří během procesu spalování velké množství různorodých prvků. Interakce návarové slitiny Inconel 625 s prvky, které jsou tvořeny během procesu spalování, je umocněna vysokými spalovacími teplotami, které mohou dosahovat hodnot až 600º C. Takto agresivní prostředí degraduje materiály vysokou rychlostí. Inconel 625 patří k superslitinám, které jsou pro takové prostředí vhodné. Procesem navařování dochází k teplotnímu ovlivnění jak návarové vrstvy, tak základního materiálu. Návarová vrstva je dvouvrstvá. Tento způsob je zvolen proto, že základním parametrem, který je hodnocen z hlediska použitelnosti ve spalovacích kotlích, je zředění návarové vrstvy železem. Železo má vysokou afinitu k prvkům, jako je síra, fosfor, chlor a dalším prvkům, které jsou tvořeny během spalování odpadu. Hranice dostatečného zředění povrchu železem se udává hodnotou 5 %. Toto zředění je dáno svařovacími parametry, jež jsou mezi sebou jednotlivě provázány. Hlavním parametrem je velikost tepelně ovlivněné oblasti. Hloubka této oblasti je řízena svařovacím proudem, dále rozkyvem, svařovací rychlostí a také chlazením. Chlazení je v tomto případě řešeno tak, že celý proces navařování probíhá již na membránových stěnách, které jsou připojeny na vodní okruh.

Výzkum v diplomové práci je zaměřen na analýzu dvou typů vzorků návarového materiálu Inconel 625. Jednotlivé vzorky byly navařeny na základní materiál 16Mo3. Navařování proběhlo na robotickém pracovišti ve firmě Šmeral s.r.o., kde byl simulován reálný proces navařování na robotickém pracovišti opatřený manipulačním zařízením, chladícím okruhem a samotným svařovacím zdrojem od firmy Fronius. Vzorky se od sebe navzájem liší parametry navařování. Jednotlivé parametry navařování nebudou zveřejněné z důvodu know-how vyvíjené technologie na VUT FSI.

Základním parametrem, jímž byly jednotlivé vzorky od sebe odlišeny, byly zmíněné parametry a také zředění povrchu železem. Tato rychlá chemická analýza byla provedena přímo na pracovišti krátkou chvíli po navařování přenosným spektrometrem od značky Thermo Scientific Niton™ XL3t XRF. Toto zařízení je velmi efektivní pro rychlou analýzu přímo na pracovišti nebo kdekoliv v terénu. Bylo zjištěno, že jednotlivé návary se pohybují s obsahem železa okolo 1 % a 5 %. Jelikož je zředění návarové vrstvy železem velmi důležitá část výzkumu a vývoje výroby ochranných návarových vrstev, bylo z nabitých znalostí rozhodnuto, že chemické složení bude ověřeno na laboratorním spektrometru od firmy Thermo Fisher ARL iSpark. Tento typ spektrometru byl zvolen z důvodu způsobu analýzy vzorků, které jsou dvouvrstvé a skládají se z odlišných materiálů. Spektrometr pracuje na principu optické spektrální analýzy, která je také vhodná pro vyhodnocování povrchů vzorků. Vzorek byl

upraven na brusce, kde byla odstraněna povrchová vrstva a vytvořena ploška pro utěsnění prostoru pro měření. Měřením bylo vyhodnoceno, že jednotlivé chemické obsahy se liší od zjištěných hodnot přenosným spektrometrem, kde nejdůležitější chemickou koncentrací byl obsah železa. Proběhlo statistické vyhodnocení, kde byly měřeny 4 vzorky a na každém byla provedena tři měření chemického složení. Ve vzorku, kde bylo původně změřeno 1 % železa se nacházelo 2,76 % železa a ve vzorku, kde bylo naměřeno 5 % přenosným spektrometrem, bylo v laboratorním prostředí naměřeno 4,79 % pomocí OES spektrometru.

Po získání informací o chemickém složení jednotlivých vzorků následovala analýza makrostruktury a mikrostruktury. Analýza makrostruktury měla za cíl vyhodnotit množství vad, které vznikly ve spojení s procesem navařování, dále byla vyhodnocena velikost tepelně ovlivněné oblasti. Celá makrostrukturní analýza proběhla na digitálním mikroskopu od firmy Keyence, kde došlo k vytvoření jednotlivých snímků. Byly zjištěny vady ve formě pórů, které jsou způsobeny technologií navařování a zvolenými jednotlivými parametry. Velikost tepelně ovlivněné oblasti dosahuje u vzorků s obsahem železa ve struktuře 1,37 mm a ve vzorcích s obsahem železa 4,79 % je velikost TOO oblasti 1,38 mm. Analýza mikrostruktury proběhla na skenovacím elektronovém mikroskopu Apreo 2 od firmy Thermo Fisher Scientific. Z analýzy makrostruktury byly zjištěny oblasti, na které se analýza mikrostruktury zaměřovala. Sledovala se mikrostruktura jak návarového, tak základního materiálu, a samozřejmě vady v materiálu. Vady byly sledovány z důvodu tvaru a potenciálního šíření během procesu užívání. Mikrostruktura Inconelu 625 měla dendritickou strukturu se specifickým protažením dendritických zrn ve směru odvodu tepla. Mikrostruktura oceli 16Mo3 v tepelně neovlivněném stavu je feriticko-perlitická struktura. Tepelným ovlivněním svařovacím procesem se v materiálu vytvořila na hranici mezi jednotlivými materiály směsná struktura, která je tvořená martenzitem, bainitiem, zbytkovým austenitem. Byla sledována postupná změna struktury materiálu v závislosti od vzdálenosti zdroje navařování.

Součástí analýz návarových vrstev Inconelu 625 jsou mechanické zkoušky. Jako první zkouška byla zvolena dle předchozích analýz chemického složení, makro a mikrostruktury, zkouška mikrotvrdosti. Mikrotvrdost byla vyhodnocena na dvou vzorcích rozdělených dle chemického složení. Vzorky byly zatěžovány váhou 100 g, jednotlivé vrypy jsou ve vzdálenosti 180 µm, prodleva mezi měřeními byla 10 s. Celá analýza byla vyhodnocena na přístroji LECO AMH55. Výsledkem bylo vytvoření map mikrotvrdosti, na kterých byly vyhodnoceny jednotlivé maximální, minimální a průměrné hodnoty tvrdostí jak základního materiálu, tak návarového materiálu. Jednotlivé hodnoty se od sebe příliš neliší, maximálně v hodnotách jednotek HV. V závislosti na získaných informacích z měření mikrotvrdosti a parametrů navařování můžeme vyhodnotit, že vzorky s vyšším obsahem železa v návarové struktuře dosahují i vyšších vnitřních napětí mezi jednotlivými vrstvami návarových vrstev.

Další mechanickou zkouškou byla tahová zkouška. Primárními hodnotami, které bylo potřeba zjistit, byly hodnoty meze kluzu a meze pevnosti. Testovány byly vzorky základního materiálu oceli 16Mo3 a vzorky základního materiálu 16Mo3 s návarem Inconelu 625. Vzorky byly nařezány a připraveny pro zkoušku tahem na plazmové řezačce. Byly vyhodnocovány od každého typu vzorku tři pokusy. Měření probíhalo na tahovém zařízení ZD40, které bylo opatřeno softwarem TIRAtest, které zapisovalo a vyhodnocovalo jednotlivé parametry tahové zkoušky. Zkušební vzorky byly opatřeny vrypy pro lokalizaci přetržení jednotlivých materiálů. Z tohoto důvodu byly relevantní výsledky meze kluzu a meze pevnosti a samotná tažnost materiálu nebyla vyhodnocována. Ze získaných hodnot byly vytvořeny tahové diagramy pro zjištění průběhů tahové zkoušky. Průměrná hodnota meze kluzu u oceli 16Mo3 dosahuje hodnot 405 MPa a hodnota meze pevnosti 525 MPa. U vzorků s návarovou vrstvou materiálu Inconel 625 dosáhla průměrná hodnota meze kluzu 497 MPa a hodnota meze pevnosti 654 MPa.

Informace nabyté z teoretické části a jednotlivých analýz jsou využity v dalším výzkumu a vývoji problematiky navařování Inconelu 625. Hlavním zaměřením výzkumné části práce byla analýza návarů vytvořených za využití parametrů navařování ve formě synergií, jež jsou doporučeny dodavatelem svařovacích zdrojů. Výsledky získané z analýzy chemického složení posloužily pro ověření správnosti použití jednotlivých svařovacích parametrů. Analýza makrostruktury posloužila pro zjištění, zda použité parametry vytvářejí návar o dostatečné kvalitě. Dále bylo možné zjistit množství a velikost vad a stanovit oblasti pro hodnocení materiálové mikrostruktury. Ta byla hodnocena především z toho důvodu, jak se daný materiál chová při dvouvrstvém navařování. Důležitou informací o mikrostruktuře navařované vrstvy byla změna tvaru jednotlivých dendritických zrn v závislosti na navařování a opakovaném vystavení materiálu tepelnému účinku. V základním materiálu byla sledována směsná struktura a přechod do základního materiálu, který byl bez tepelného ovlivnění, kde se nacházela feriticko-perlitická struktura. Byly sledovány také vady kvůli zjištění, v jaké formě se nacházejí a zda mají vliv na snížení životnosti návaru. Informace získané z analýz chemického složení a mikrostruktury materiálu byly použity ve zkoušce mikrotvrdosti. Byly vytvořeny mapy mikrotvrdosti, kde bylo zjištěno, že vzorek s vyšším obsahem železa ve struktuře, a tedy i za použití rozdílných parametrů, dosahuje většího vnitřního napětí, které bylo zjištěno vyšší tvrdostí na hranici mezi jednotlivými vrstvami Inconelu 625. Jednotlivé hodnoty mikrotvrdosti se od sebe navzájem příliš nelišily, šlo pouze o velikost a rozložení vnitřního napětí v materiálu. Jako poslední zkouška byla zvolena tahová zkouška. Zde bylo za úkol zjistit velikost meze kluzu a meze pevnosti základního materiálu a kombinace základního materiálu s návarem. Byly vytvořeny tahové diagramy, ze kterých bylo hned zjevné, že vzorky s návarovou vrstvou dosahovaly vyšších hodnot.

Na základně zjištěných údajů z teoretické rešerše a analýz lze pokročit ve vývoji a výzkumu v problematice zvyšování korozní odolnosti membránových stěn pomocí navařování materiálu Inconel 625. Informace budou využity pro hodnocení kvality jednotlivých návarů z hlediska použití svařovacích parametrů. Výsledky mohou být použity v dalším studování materiálové problematiky Inconelu 625 v závislosti na tepelných procesech, jako je například změna struktury v provozu, degradace materiálu po čase v provozu nebo v dalším výzkumu prodloužení životnosti membránových stěn spalovacích kotlů, kde z hlediska budoucnosti a ekologie je možnost velkého posunu vlivu na životnost materiálů využívaných v odvětví likvidace odpadu.

BIBLIOGRAPHY

CHRÁST, Daniel. *Analýza návarové vrstvy Inconel 625 vytvořenou metodou MIG-CMT* [online]. Brno, 2023 Dostupné z: https://www.vut.cz/studenti/zav-prace/detail/145685. Diplomová práce. Vysoké učení technické v Brně, Fakulta strojního inženýrství, Ústav strojírenské technologie. Vedoucí práce Jaroslav Kubíček.

AFFIDATIV

I declare that I have elaborated my master thesis " Analysis of Inconel 625 weld layer produced by MIG-CMT" independently using technical literature and other sources quoted throughout the thesis and listed at the end.

Brno, 20.5.2023

Bc. Daniel Chrást

ACKNOWLEDGEMENT

I would like to thank Ing. Jaroslav Kubíček IWE for supervision of my thesis, and to Ing. Martin Slaný Ph.D for preparation of samples. Next I would like to thank Mgr. Michaela Krchová, Ing. Eliška Jakubcová, Mgr. Ondřej Hrabina Ph.D. and Ing. Kamil Podaný Ph.D. for help with the experiment. Last but not least I would like to thank to my family, especially my brother Mgr. Petr Chrást for discussion about the interpretation of results.

TABLE OF CONTENTS

INTRODUCTION

Nowadays there is a great emphasis on waste management. Waste has been managed in several ways, the main ones being recycling, incineration and storage. In Czech Republic, there is still a slightly increasing trend in the amount of produced waste. On average, the amount of waste produced is above 300 kg per inhabitant per year. Incineration is a sensitive issue as it has been found that municipal waste has a good calorific value. Incineration has been used to dispose of approximately 20 % of the total volume of municipal waste. [1; 2]

Modern energy boilers are complex devices utilizing membrane wall systems. Water flows through the walls of the boiler and is converted into more usable steam by heating. As waste has been burned in the boiler, a very corrosive and erosive atmosphere has been created where temperatures can reach up to 600 ºC at the surface of membrane wall. Example of incineration plant is shown in the figure 1. The incineration process causes heavy wear of the membrane wall surface in the order of tenths of millimeters per year. To increase the lifetime of the membrane wall and thus increase the productivity of the process, heat resistant steels are used. To further increase the lifetime, methods of applying special materials to the membrane walls are used, including the welding of nickel superalloys. [1; 2]

Fig. 1 Example of incineration plant [1]

1 INTRODUCTION TO THE SOLVED PROBLEM

Waste generation occurs, for example, in households, cleaning, agriculture, construction, but above all in all industries. There are several ways in which waste can be managed. The first way is to recycle the material, then it is possible to use organic waste for composting. Waste that cannot be recycled is used in energy industry to generate heat in form of incineration. The last option, which people have been trying to avoid in recent years, is storage, because of high environmental and health impact. There are currently more than 400 incineration plants in the EU, treating more than 50 million tons of waste per year. The average calorific value of municipal waste ranges from 7 to 11 Mj/kg. Detailed calorific values of each type of waste material has been shown at table 1. [1; 2]

Table 1 Calorific value of waste components [1]

Type of waste	Calorific value [MJ/kg]
Paper	15,7
Plastic	32,7
Polyethylene	43,4
Polystyrene	38,0
Polyvinyl chloride	22,5
Textile	18,3
Food	3,2
Trash	6,0
Wood	12,4
Glass	0,2

Municipal waste incineration in Europe accounts on average for 20 % of the total municipal waste treatment. The amount of waste is increasing by 2 to 3 % per year. Up to 70 % of the energy recovered from waste incineration is used in the form of heat energy and the remaining 30 % in the form of electricity. The efficiency of waste incineration is around 15 %. Sources show that around 8.3 million tons of oil equivalent are saved annually in the EU by incinerating waste. Although efficiency is lower than conventional clean fuel incineration processes, thermal treatment of waste serves to gain energy outside the process itself. Therefore, waste incineration can be considered to reduce the consumption of primary energy resources. Research and development in energy industry foresees the invention of waste incinerators with efficiencies of up to 30 %. The main issue is the composition of municipal waste. This varies according to where the waste is produced, whether in family areas or industrial zones. Table 2 shows the number of chemical elements and their average content in the waste. [1; 2]

Table 2 Elemental composition of waste. [1]

Element	Quantity [%wt]	Element	Quantity [mg/kg]	Element	Quantity [mg/kg]
Carbon	18-40	Lead	100-2000	Cobalt	3-10
Hydrogen	1-5	Zinc	400-1400	Cadmium	1-15
Nitrogen	0.2-1.5	Copper	200-700	Mercury	1-15
Oxygen	15-22	Manganese	200-250	Arsen	2-5
Sulphur	0.1-0.5	Nickel	30-50	Selenium	0.2-1
Fluorine	0.01-0.035	Chromium	40-200	Thalium	<0.1
Chlorine	0.1-1	Vanadium	4-11	PBC	0.2-0.4

1.1 Water walls of incineration plants

The use of water walls in incineration plants began to increase the incineration performance and calorific value of boilers, while reducing heat loss and maintenance requirements. Another advantage is that the flowing water reduces the amount of refractory material used, as the water lowers the temperature of the walls. The water walls of the boilers can be responsible for the reduction of air leakage into the boiler space, thus improving the overall efficiency of the boilers. The diameters usually range from 30 to 70 mm. Several smaller diameter tubes have a larger functional heat transfer area per unit length than a comparable wall of larger diameter tubes. Another advantage is the possibility of using higher pressures at the same tube wall thickness together with a larger heat transfer surface. From a manufacturing point of view, tubes with thin walls are easier to manufacture and bend to the required shapes. Smaller tube diameters also require less water in the entire system. Disadvantages include a small amount of reserve water and control of the water level. Tubes are most made of low alloy steels, corrosion, and heat resistant steels. There are four basic types of incineration boiler water walls. [3; 4]

Tube and tile is the oldest type of boiler wall construction. This design provides poor maintenance and large heat losses. To maximize the efficiency of this design, spacing between tubes must be minimized. Tube and tile has been shown in the figure 2. [3; 4]

Studded tube consists of tubes with many pins, which serve for better heat conduction and especially for clamping the refractory material on the tubes as it has been shown in figure 3. It has been used in the high temperature parts of the boiler. Still not the best design solution as the flue gases can still permeate the structure and cause corrosion. [3; 4]

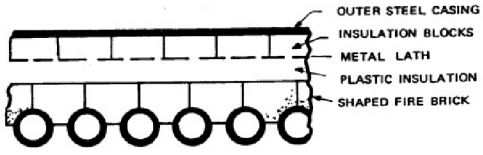

Fig. 2 Tube and tile. [3]

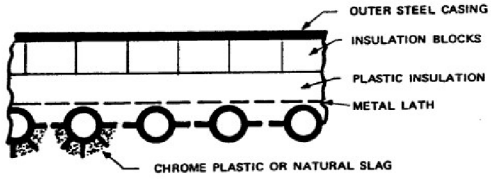

Fig. 3 Studded tube. [3]

Tangent tube has design solution that does not use refractory material on the inside of the boiler, but only as thermal insulation on the outside as shown in figure 4. The disadvantage is the repair in case of tangential wall failure because the tube must be completely removed. [3; 4]

Membrane walls are one of the best structural solutions because they do not transmit radiant heat and guarantee gas tightness and high heat transfer. It has been shown in figure 5. The overall construction of the walls consists only of welded tubes and membranes. It has been manufactured in blocks of 6 x 1 meter by TIG, MIG/MAG or SAW technology. The insulation layers are on the outside of the boiler. In practice, two types of membrane water walls are used. The first type is an assembly welded together from tubes and membranes that are between the tubes. The second type uses a different design of tubes that have a rolled fitting that are welded together. The disadvantage lays in the case of repair. To increase durability, such welding technologies are used where the resulting surface coating is more resistant to wear mechanisms. These are mainly chromium spraying or nickel-based austenitic materials. The welding process must have the lowest possible mixing and thermal influence. [3; 4]

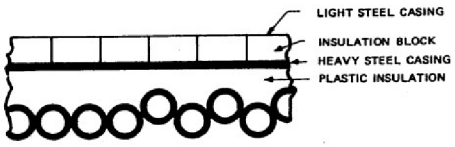

Fig. 4 Tangent tube. [3]

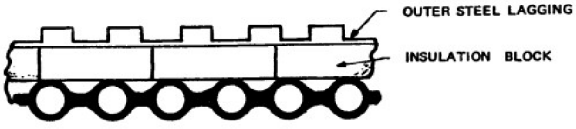

Fig. 5 Membrane wall. [3]

1.2 Corrosion of membrane walls

In general, corrosion is regarded as an undesirable wear process. Corrosion is a very complex process that brings several disciplines together such as chemistry, physics, metallurgy. A suitable corrosion resistant material must have sufficient corrosion resistance. This is determined by the corrosion lifetime, which determines the time when the metal is free from serious failures and defects. Generally, the corrosion wear interval is reported to be between 0,1μm and 0,1mm per year. Corrosion always and everywhere takes place. Zero corrosion resistance is only theoretical under realistic conditions. Corrosion generally deteriorates the mechanical and physical properties of the material. [5]

The incineration of municipal waste causes a lot of wear and tear on the boiler membrane walls. The wear occurs due to high temperatures and aggressive chemical environment. The wear is greater than in conventional boilers, since waste is burned which is very heterogeneous in composition (plastic, paper, biomass, industrial waste). The atmosphere therefore contains many chemical elements that are very reactive, such as sulfur, chlorine, phosphorus, and others. For this reason, the lifetime of membrane walls is greatly reduced. Even though the wear is very complex, thermal wear is the major contributor to the reduction in service life. Combined with chemical wear, carbon and low alloy steels degrade very rapidly. Corrosion occurs, leading to wall thinning, where the rate of thinning is in the range of 0,15-0,30 mm per year. The resulting service life of the membrane walls is therefore 6 to 9 months. For membrane walls of incineration boilers, corrosion is classified according to the corrosive environment, location and range of damage, type of chemical reaction and physical conditions and appearance and speed of appearance. [5; 6]

High temperature corrosion occurs at temperatures of 600 °C inside of the boilers. Figure 6 shown the high-temperature corrosion. Due to free chlorine content of the incineration process. The free chlorine forms ferric chloride on the surface of the material. As oxygen and sulfur are present in incineration process, the chlorine reacts with the oxygen and sulfur which diffuse out of the flue gas. The oxide forms away from the pipe and prevents the formation of a gas-tight protective iron oxide layer. Oxygen is consumed on the outer layers of the wall, such as scale and deposits. This creates a reducing atmosphere on the corrosion front, which then allows iron chloride to form on the pipe wall. The sulphation of the chlorides contained in the ash deposit then contributes to a sufficiently chloride partial pressure on the wall. Possible causes of high temperature corrosion are, for example, reducing conditions due to imperfect incineration, high chlorine content in the fuel, insufficient cooling of the tubes or high heat flux. High temperature corrosion range from 25-500 $nm\text{-}h^{-1}$. [5; 6]

The corrosion resistance of the material depends on the passivation layer, which suppresses anodic dissolution. The flue gas contains solid particles from elements that promote anodic dissolution as they mechanically disrupt the passivation layer. Hydromechanics describes the flow phenomena. Turbulent flow is known to cause higher corrosion-erosive effects than laminar flow. The amount of damage increases with increasing flow velocity of the medium. From Siemens AG research shows that the resistance to erosive corrosion of carbon and low-alloy steels used to produce membrane walls is increased by the addition of chromium, molybdenum and even copper. Also, chromium-rich coatings show greater resistance to erosive corrosion than nickel coatings. In the case of membrane walls, the flue gas is the flow medium, both in gaseous and solid state. As shown in figure 7 erosive corrosion has a large- scale character. [5; 6; 7]

Fig. 6 High temperature corrosion. [7]

Fig. 7 Erosive corrosion. [6]

Pitting corrosion is divided into two stages. The first is the growth stage and this is dependent on the concentration of halides and the more halides there are, the shorter the growth stage. The second is the propagation stage, which is easier with higher concentration of halides and oxides, elevated temperature, and low pH. In membrane walls, pitting corrosion is caused by defects in the materials from which the membrane walls, pitting corrosion is caused by defects in the materials which the membrane walls are made. Defects include material inhomogeneity in the form of precipitates and chemical compounds and inclusions. Resistance to pitting corrosion is increased by alloying with molybdenum, or by reducing the oxidation capacity of the environment and increasing the amount of nitrate. Nickel superalloys are among the materials resistant to pitting corrosion. From the point of view of the production technology, the most important cause of pitting corrosion is a roughly machined surface or the presence of scale. In general, pitting resistance is determined by calculating the **PRE** (pitting resistance equivalent) value. The standard value is **PRE 40**. The calculation of **PRE** is described in equation 1.1. When steel reaches this value, it is completely resistant to corrosion. Pitting has been shown in the figure 8 and 9. [5; 8]

Equation 1 **PRE** number [8]:

$$PRE = Cr + 3{,}3(Mo + 0{,}5W) + 16N \tag{1.1}$$

where: Cr – chromium [wt%]
Mo – molybdenium [wt%]
W – tungsten [wt%]
N – nitrogenium [wt%]

Fig. 8 Pitting [8]

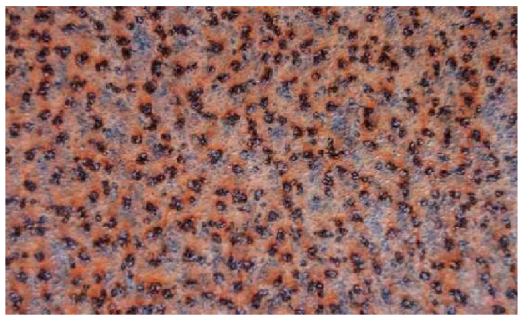

Fig. 9 Detail of pitting [8]

2 PRODUCTION OF MEMBRANE WALLS AND WELD OVERLAYS

Three methods are used to increase the corrosion resistance and thus extend the life of boiler membrane walls. The first and simplest way to extend the life of an incineration boiler is to completely replace the tubes and replace them with new ones. This option is not widely used, as replacement is very economically expensive and requires suspension of the incineration process for up to several months. The second option to extend the lifetime of the incinerator is to reduce the operating parameters such as the operating temperature of the incineration or the operating temperature of the steam. However, this results in a lower efficiency of the whole incineration process. Secondary circuits, such as the cleaning circuit, are also affected, as the elements that must be filtered out are not combusted perfectly. The third and most optimal way to extend the life of the boiler incineration walls is to create a passivation coating of nickel - based superalloys. Several methods can be used to create the layer. The first method is by manual welding with a coated electrode, more sophisticated methods are by MIG/MAG or CMT modification. The last way is to use thermal spraying. The MIG method is the most widely used of these methods, as it uses an inert gas environment and is also an easily automated method that achieves high productivity. [4; 9; 10]

As mentioned, high temperature, chemical heterogeneity of the waste and the associated high chlorine, sulfur, phosphorus, and salt content are the most important factors in the corrosion process. This significantly reduces the corrosion resistance of the membrane walls. Resistance is increased by the choice of appropriate materials. The most used materials are high chromium, molybdenum, or nickel-based superalloys. The nickel superalloys are the most widely used and complex type of alloy used in highly corrosive environments. Nickel superalloys are classified according to their use in industry. They are divided into structural alloys, with special physical properties, and refractory alloys. According to the method of production they are divided into cast steels, shaped steels and steels produced by powder metallurgy. Nickel superalloys achieve high values of strength, corrosion resistance, corrosion resistance at high temperatures. The most used nickel superalloys include Inconel, Nimonic, Hastelloy. [9; 10]

2.1 Production of membrane walls

Membrane walls are one of the best types of boiler water wall, but they are also difficult to manufacture. Membrane walls are consisting of tubes in which water flows and strips of sheet metal that connect the single tubes. The walls can be fitted with additional components, for example, for fuel or air supply to improve the incineration process. The production of membrane walls is most often carried out on automatic lines. Production on an automatic line must be variable because of the possibility of changing the dimensions of the uniform parts of the membrane wall. The width of the membrane wall is determined by the number of elements welded. The length is determined by the tube blank, which is most often supplied in 6 m lengths. If there are requirements for longer walls, the tubes are lengthened. In the first step, the surface and geometric preparation of the pipe is carried out on an automatic line. It is blasted and degreased to remove oxides, grease, and impurities. Next, a bevel is made on the wall for welding. Next, the strip elements are prepared, which are located between each pipe. This consists of cutting the required lengths and then blasting, degreasing, and then creating the bevels for welding. [9; 10; 11]

Welding is carried out on automatic lines, most often using the SAW method. This method is very easy to automate, fast and does not glare. Welding is most often done in the PA or PB positions. The movement of the membrane walls is by means of pulleys and conveyors. After welding one side, the other side is turned and welded. The welding machine has been shown in figure 10. If required, heat treatment is carried out after welding. The completely welded membrane walls are then checked by X-ray and visual inspection. [9; 10]

The membrane wall can be further bent and shaped in various ways. In case the walls are coated, the shape of the walls must be free of bends, if possible, for better automation of the process. TIG, MIG/MAG manual welding is only used for repairs or for finishing, as defects are more likely to occur with hand welding. [11]

Fig. 10 SAW welding of membrane walls. [11]

2.2 Production of protective layer

Technologies for the formation of a protective layer on the membrane walls of incineration boilers are divided into two main groups. The first group includes non-conventional technologies that use electric arc coating and high-speed spraying. The most used technologies include electric arc spraying and arc welding, the arc spraying technology is shown in figure 11. These technologies are characterized by their speed and angle of incidence. The parameters cause the formation of oxide inclusions and affect adhesion and porosity. The critical value for corrosion is a pore content of 10 %. Hot spray adheres to the material surface by Van der Waals forces as well as by chemical bonds of covalent and metallic type and by metallurgical processes. The second convection group for the formation of a protective layer on the walls of boiler membranes is the use of welding processes. [11; 12; 13]

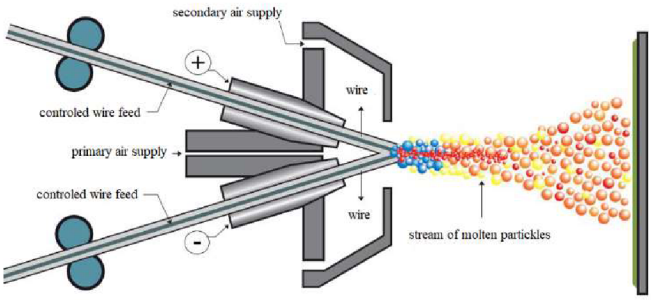

Fig. 11 Electric arc spraying [12]

The layer is formed using molten additive material. During welding, it is necessary to reduce the amount of dilution of the additive and base material. The amount of iron in the weld metal should be as low as possible, as iron reduces corrosion resistance of the material. The amount of iron can be reduced by the choice of suitable additive material, the welding position and by water circulation in the pipe walls. The advantages of welding are simple automation, formation of an any thick weld and good bonding to the base material by means of a metallic bond. The most used welding methods are laser, plasma, or electric arc welding. Electric arc welding is divided into MIG and MAG according to the type of active gas. A special form of MIG/MAG technology is the CMT (cold metal transfer) method. [14; 15; 16]

MIG/MAG - CMT is the most suitable method for welding materials onto membrane walls. This method is characterized by low heat input to the material. Three criteria are important for the formation of the coating. The first is a suitable welding device that meets the dynamic and kinematic requirements of the welding process. The equipment must be equipped with an electronic system for plotting the trajectory and identifying the necessary points. The second criterion is the choice of the correct method of laying the welds. Variability for different membrane walls must be observed. The most common and the most appropriate way is the choice of weld stacking, as shown in figure 12. The third criterion is the choice of the correct welding trajectory. The trajectory affects the rolling algorithm. This algorithm includes the dimensions of the tubes, the material to be welded and the weld itself. [15; 16]

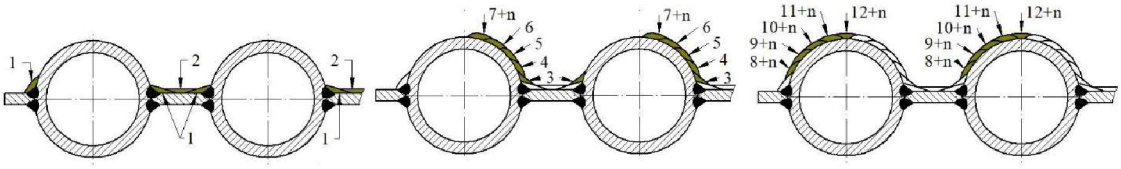

Fig. 12 Production process of protective layer.

2.2.1 MIG and MAG technology

MIG and MAG technologies belong to the fusion welding group. In these technologies, local heating is generated by means of an electric current. An electrode in the form of a wire is used as an additional material which is melted. The diameter of the electrode ranges from 0,6 to 1,6 mm, thus achieving a high current density. The electrode is moved by means of pulleys which are synchronized to prevent the electrode from slipping. The electric arc is connected by means of a contact line in the welding head. The contact line is made of copper and for technologies that use solid wire it is connected to the positive pole. For technologies that use tubular wire, the contact line is connected to the negative pole. The other pole is connected to the material to be welded. The shielding material is conveyed to the welding site by hoses and directed by the nozzle of the welding gun. In the MIG and MAG methods, slag is not formed on the weld metal during welding, so it is necessary to protect the welded material until it cools down to a low temperature. These methods allow welding material from 0,8 mm thick. The transfer of molten metal to the welding site varies according to the current delivered to the welding site. If the current value is low, the transfer is short circuited. As the current value increases, the transfer changes to shower transfer and at the highest current values the transfer is rotary. The whole MIG/MAG technology has been described in the figure 13. [15; 16]

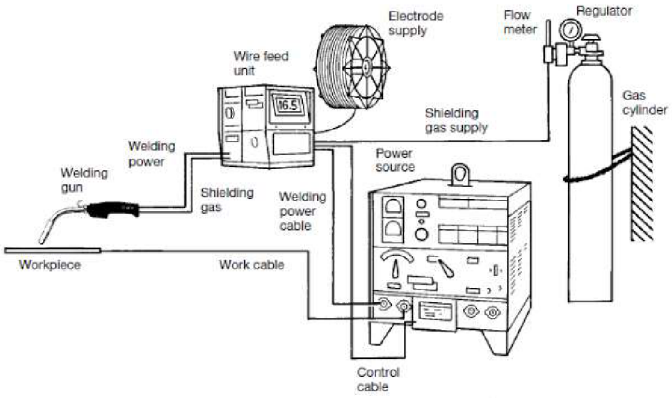

Fig. 13 MIG/MAG welding scheme [16]

MIG technology uses fusion arc welding with a melting electrode, which takes place in an inert gas environment. Argon, helium, or a mixture of these gases is used as the inert gas. This technology is suitable for welding non - ferrous metals and their alloys such as aluminum, copper, titanium. The use of helium causes an increase in the temperature of the electric arc. Pulse mode is the most frequently chosen technology for welding protective layers on the membrane walls of incineration plants. The shielding gas is a four-component mixture of argon and helium. To achieve a suitable layer, it is necessary to select the correct overlapping pattern and welding position. [15; 16; 17]

MAG technology belongs to the same group of welding technologies as MIG technology. Compared to MIG technology, MAG technology is characterized using an active environment. Most often carbon dioxide or a mixture of argon and oxygen is used. The use of carbon dioxide alone is more economically advantageous, due to the lower price. The disadvantage is the formation of oxide and carbides in the weld. Spatter occurs due to the high voltage of the electric arc. MAG technology is used for welding ferrous materials, more precisely non - alloy, and low - alloy steels. For welding high - alloy steels, a mixture of argon and carbon dioxide is used. [15; 16; 17]

2.2.2 CMT modification

The CMT welding method was developed by Fronius in 2005. The method is particularly exceptional because of the movement of the welding electrode, which performs an alternating back and forth motion. This specific movement was first used in 1997 for the spray less arc ignition. The principle of the welding cycle is divided into four parts, as shown in figure 14. In the first part, an arc is created by increasing the current and the welding wire is moved towards the material. As soon as contact is made, the current is reduced by electronic control. If the current is not reduced, the resistance would drop as in conventional methods, and this causes the end of the electrode to melt and unwanted spatter. After the welding material is joined with the filler material, the wire is pulled back into the welding head as shown in the third section where the drop of material is separated. In the last part, the current is increased again, where due to the small distance hopefully an arc is formed and the whole process is repeated. The whole process is repeated at a high frequency of up to 130 Hz. The whole cycle does not depend on a predefined current dependence. The process has a set one period that repeats after each short circuit signal is sent. This guarantees high weld quality as the length of the welding wire is well regulated, this is particularly important for manual welding. [16; 18; 19]

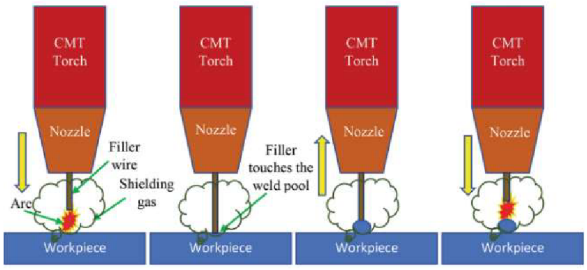

Fig. 14 Phases of CMT welding [18]

The advantage over other arc welding methods is the smaller heat affected area. The amount of heat input to the weld depends on the wire feed rate while keeping the other parameters constant. Furthermore, there is much less mixing of the base and additive material, where for CMT the mixing values are in the units of percent. This improves the quality of the filler layer because, as mentioned in previous chapters, the corrosion resistance of the material decreases as the mixing value increases. It has been found that a contact angle of at least 115° is necessary for uniform bonding of homogeneous welds. If the angle is in the range of 90° to 100°, no uniform layer is formed. CMT method has been divided by different welding processes: [16; 18; 19]

- CMT pulse - the welding process is modified by the addition of a phase where a lossless pulse transfer takes place. This phase follows the droplet separation. More heat is introduced into the weld joint. Any number of pulses can be added in this phase, depending on the amount of heat energy required. The more pulses are added, the larger the pores in the weld become. By making the pores larger, it is easier to reach the surface and cracks do not form. The length of the free end of the wire is the same as in the conventional CMT. [20]
- CMT advanced - this modification works with polarization of welding cycles. The polarity change occurs during the short-circuit phase while the arc remains stable. During the negatively polarized phase, the process achieves high melting performance and better joint bridging. The bridging value is up to several millimeters. During the positively polarized phase, a targeted heat gain and precise droplet transition is achieved. During the transition between polarities, zero current is crossed and the arc is extinguished. The ratio between the phases can be defined according to requirements. This modification guarantees high arc stability and very low heat input to the weld. The quality of the joints is very high. [21]
- CMT advanced pulse - the CMT Advanced Pulse process consists of a combination of CMT cycles with negative polarity electrodes and a pulse phase with positive polarity. During the negatively polarized phase of CMT, higher melt power is achieved with low heat input. During the polarity change to positive pulse cycle, a short circuit occurs. With the pulse phase, the user achieves a short-circuit-free droplet transition in addition to higher heat. The ratio between positive and negative cycle process is also freely selectable here. In this way, joining of high-strength steels can be carried out with sufficient melting power and low heat input. [22]

2.3 Heat resistant steels

Heat resistant steels are classified as structural steels and represent a very broad group of materials. These steels are suitable for long-term mechanical stresses at temperatures above about 500 °C. In addition to the high pressures, they must also resist material creep, but also have various requirements such as corrosion resistance or wear resistance in various aggressive environments. Refractory steels are mainly used in the power, chemical or nuclear industries, where they are used for the manufacture of rotors, boiler parts or, for example, nuclear reactor cladding. [23; 24]

A property of called creep occurs in heat-resistant steels. This phenomenon is defined as plastic deformation occurring under conditions of long-term stress at elevated temperature. Under such conditions the deformation becomes a function of temperature, time, and stress. Creep processes are significantly manifested above the homologous temperature of metals and their alloys ($\mathbf{T_G}$), which is about $\mathbf{0{,}4\ T_T}$, where $\mathbf{T_T}$ is the melting temperature of the metal or alloy. Creep is represented by a creep curve, which is a function of strain on time. The full creep curve consists of three main parts. The first part is characterized by a rapid rate of deformation, which soon stabilizes. In the second part, the rate of creep is constant and hence there is a linear increase in material deformation, and an equilibrium between strain hardening and material softening occurs. This part of the curve is the most important and most research focuses because it is the longest phase in time and is indicative of the lifetime of the material. The last part of the curve is characterized by an exponential increase in the strain rate and ends with the fracture of the material. In figure 15 all phases are then marked and illustrated. [23; 24]

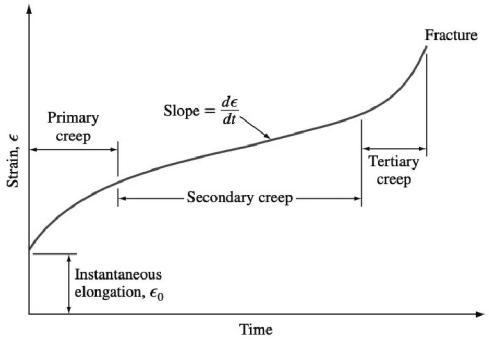

Fig. 15 Stages of creep [24]

Plastic deformation by creep has 2 basic mechanisms. Diffusion motion of atoms or dislocation motion. Diffusion creep occurs at low stresses but requires relatively high temperature. When loaded, one side of the grain stretches to form vacancies, and the other side of the grain compresses to form interstitial atoms. Diffusion then equalizes the concentrations of these point defects, and grains elongate in the direction of the tensile stress. The condition for dislocation creep to occur is that the stress in the material must overcome some resistance in the crystal lattice. It can be concluded that the stronger the lattice of the solid solution steel, the greater the resistance to creep will be and dislocation motion will be avoided. Among the most important strengthening principles is precipitation strengthening, which is caused by the presence of fine precipitates in the structure, mainly carbides of alloying elements. These precipitates then form barriers against the movement of dislocations. Another possible hardening is solid solution hardening, which is mainly caused by Mo and W. The substitution of these elements in the underlying metal lattice causes deformation of the lattice, thereby forming a barrier to the movement of dislocations. Even the type of lattice itself influences the movement against dislocations. [25; 26]

2.3.1 Heat resistance

The heat resistance of a steel is its ability to withstand, at high temperatures, long-term stresses without unacceptable plastic deformation or fracture. Other requirements may be resistance to oxidation, corrosion, hot fatigue fracture or, for example, good mechanical properties at lower temperatures. All materials must have this property, which are used for work at temperatures higher than the homologous temperature characteristic for the intersection of two strength properties at elevated temperatures. This is the minimum yield strength R_e and creep strength $R_{mT/T/10}$, see figure 16, temperature is defined as $\mathbf{T_G = 0.4\ T_T}$. Alternatively, it can be defined the refractoriness as the stress at temperatures above 500 °C. [23; 25; 26]

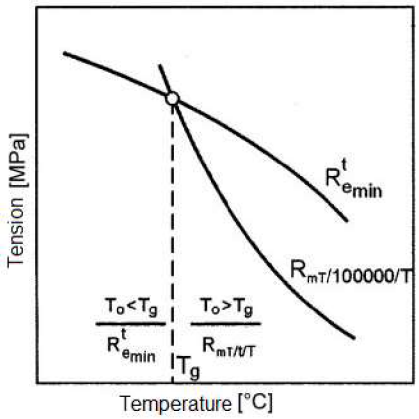

Fig. 16 Point of Homologenous temperature [25]

Two basic values determine optimal material for construction. The yield strength at higher temperatures and the creep strength. In terms of reliability, the strength calculations in strength calculations, the lower value is preferred. Figure 16 shows the intersection of the $\mathbf{R_e}$ and $\mathbf{R_{mT}}$ values for carbon steel used for the manufacture of steam boiler evaporators. At operating temperatures below about 420 °C, the preferred calculation $\mathbf{R_e}$ value, while for higher temperatures the $\mathbf{R_{mT}}$ value will be preferred. [23; 25]

Many factors must be considered when selecting the optimal alloying elements. Each element has different properties, and it is always necessary to consider not only the property under consideration, but also other properties and to create a certain compromise in order not to deteriorate other material properties. Some of the main ones include carbon, which has a positive effect on refractoriness but a negative effect on other technological properties such as formability and weldability. Nitrogen improves refractoriness up to 0,08 %, but higher amounts may be undesirable. Molybdenum and tungsten strengthen the solid solution and thus prevent dislocation creep. Chromium and its carbides also have a significant positive effect on refractoriness, but and other properties, such as corrosion resistance. For example, aluminum should be in refractory steels as little as possible. [23; 25]

Heat resistance can be assessed by various tests that predict the working time of certain components in service. The most common tests include the static tensile test at elevated temperature, the relaxation test, creep and creep strength test and thermal fatigue test. Static tensile test. The elevated temperature test is tested on a conventional tearing machine where the specimen can be heated. These values obtained are different from the creep test because this test is carried out under high stresses and up to a minimum of 50 times the actual strain. Relaxation takes place at room or elevated temperature and consists of a reduction in stress over time. The rate of relaxation R_t is then the difference in stress corresponding to the initial loading force and the force after a period t. Next test is the creep test, which is divided into low - temperature creep tests, high temperature and diffusion. Latest frequent test on hot-rolled steels is the thermal fatigue test, which consists of multiple cyclic or periodic temperature changes. [23; 25]

2.3.2 Types of heat resistant steels

Carbon steels are characterized by a fine-grained structure with a low carbon content. Maximum The temperature of use is limited by the value of the creep limit. Carbon steels are mainly used for the manufacture of tubes, plates, or castings for various power equipment such as evaporators or water heaters. These steels are rolled from quenched, semi-quenched and unquenched steels, However, when cold-forming unsettled steels, the plastic properties decrease due to deformation ageing, and the most common choice is to tempering. [23] [27]

Low-alloy steels are one of the most widespread and widely used group of hot-rolled steels. These steels are divided into yield strength steels and creep strength steels. They must have high creep plasticity but also resist oxidation or have good weldability using basic welding methods. Their carbon content shall be such that no carbon is formed cementite but only fine carbides. These carbides are usually composed of Mo, Cr or V, which are the most common alloying elements in these steels. The steels are of course alloyed with other elements which can alter the technological or mechanical properties in various ways, see figure 17. The use of these steels is limited by operating temperatures up to 580 °C. [23; 26; 27]

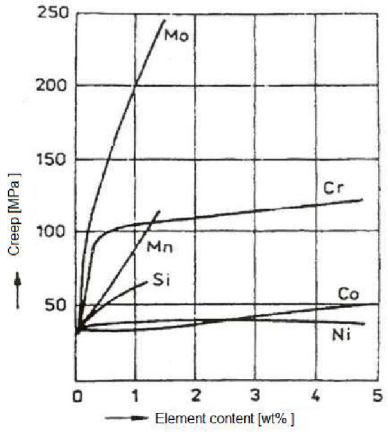

Fig. 17 Influence of elements on creep [27]

Chromium steels most often have a ferritic or martensitic structure and must not only have good heat resistance, but, due to their use at higher temperatures, must be refractory. Chromium steels have a Cr content of 9 to 12 %. The steel is suitable for use up to 620 °C and is most used to make preheated tubes for steam boilers or, for example for the manufacture of steam and gas turbine rotors and blades. Chromium steels are also alloyed with elements such as Mo, V, Nb, W, Ni or Co. [23; 26; 27; 28]

Austenitic steels are classified as steels with very high heat resistance and have a high yield strength up to 650 °C. This is mainly due to the FCC lattice, which has a denser arrangement and movement dislocation is thus considerably reduced. These steels are easy to form lattice defects, which also prevent the movement of dislocations. Another advantage is that austenite has a temperature recrystallisation temperature in the range 800-900 °C, unlike ferrite. To form an austenitic structure, it is necessary to add austenite-forming elements such as Ni or Mn to the steel. Austenitic refractory steels are therefore divided into chromium nickel austenitic steels and manganese chromium austenitic steels. In chromium nickel steels, elements such as W or Mo are added to increase the refractoriness, sometimes can also be Nb, Ti, V and N. The Cr content here is in the range of 12-20 %, which will also guarantee a good corrosion resistance of the material. It is advisable to heat treat the steels with a stabilizing or dissolving annealing to reduce the content of the undesirable Laves phase. Manganese-chromium steels, use cheaper Mn instead of Ni. [26; 27; 28]

Austenitic hard enable steels are used in even more demanding conditions than chrome nickel steels. Temperature applications are up to 750 °C and they also have a very good creep strength and generally good plastic properties. The material acquires these excellent properties when dissolution annealing at 1150 °C for 1 h followed by cooling in air. The heating is then repeated, but at 750 °C for 20 h. This heat treatment produces a saturated solid gamma solution with a small amount of undissolved TiC carbides in the structure. The main additives here are Ti, Al, B and Mo, which increase the required creep strength. [23; 25]

The most used carbon low-alloy steels are most often alloyed with Cr and Mo. The choice of membrane wall material depends mainly on the operating temperature and pressure. Chemical composition and mechanical properties see Table 3.

EN P235GH – W. Nr. 1.0345 – is heat-resistant steel. The letters in the designation have the following meaning. P – weldable, G – soft annealed, H - hardened. Suitable for continuous heat loads up to 450 °C. [29]

EN P265GH – W. Nr. 1.0425 – belongs to the same group as the previous material. Operating temperatures up to 450. Compared to the previous material it has lower tensile strength. It has good weldability. [30]

EN X10CrWMoVNb9-2 – W. Nr. 1.4901 - – is a low-alloy stainless steel suitable for temperatures up to 650 °C. Standard annealed and tempered. Corrosion-resistant, with guaranteed yield strength, and good weldability. [31]

EN 16Mo3 -W. Nr. 1.5415 - is a low alloy steel with increased heat resistance, resistance to high temperature corrosion and creep. Operating temperatures of this steel range up to 500 °C. It is very easy to weld. The mechanical properties can be increased by approximately 15-20 % by standardization annealing. [32]

EN 13CrMo4-5 – W. Nr. 1.7335 is a low-alloy stainless steel suitable for temperatures up to 530 °C. Corrosion-resistant, with guaranteed creep limit, good weldability. [33]

EN 7CrMoVTiB10-10 -W. Nr. 1.7378 – is a low-alloy stainless steel suitable for working temperatures up to 600 °C. Standard annealed and tempered. Corrosion-resistant, with guaranteed yield strength, good weldability. [34]

Table 3 Chemical composition and mechanical properties of steels. [31; 32; 33; 34]

	1.0345	1.0425	1.4901	1.5415	1.7335	1.7378
wt % C ≤	0,16	0,2	0,13	0,2	0,18	0,1
wt % Si ≤	0,35	0,4	0,5	0,35	0,35	0,45
wt % Mn ≤	0,6-1,2	0,8-1,4	0,3-0,6	0,9	0,4-1	0,3-0,7
wt % P_{max}	0,025	0,025	0,02	0,025	0,025	0,02
wt % S_{max}	0,015	0,01	0,01	0,020	0,01	0,01
wt % Cr ≤	0,3	0,3	8,5-9,5	0,3	1,15	2,2-2,6
wt % Cu ≤	0,3	0,3	0,3-0,6	0,3	0,3	-
wt % Ni ≤	0,3	0,3	0,4	0,3	0,01	-
wt % Mo ≤	0,08	0,08	0, -0,6	0,35	0,6	0,9-1,1
Re [MPa]	235	264	355	280	290	350
Rm [MPa]	360-500	410-530	620-850	450-600	450-600	565-840
A_5 [%]	23	22	19	22	21	17
$R_{p0,2}$ [MPa]	108	133	440	150	175	450

2.4 Nickel and nickel alloys

Nickel is one of the most abundant elements on Earth. It is a silver-gray metal that is stable in air, resistant to alkalis, and has very good ductility. In nature it is found most often in compounds with oxides or sulfides. The production of pure nickel is very expensive, as it is difficult to isolate from other elements. The most common methods of producing pure nickel are electrolysis or carbon reduction. Nickel has a negative effect on the human body. It can cause allergies, redness and swelling. The atomic number of nickel is 28. The atomic weight is 58,71. The crystal structure is FCC is shown in the figure 18. Compared to other metals, nickel has a high density of 8907 kg/m^3. In comparison, titanium has 4508 kg/m^3 and aluminum has 2698 kg/m^3. This makes nickel an ideal material for use in the aerospace industry. Nickel has stable mechanical properties at both high and low temperatures. The recrystallisation temperature is around 600 °C. Nickel has a low ultimate strength of 220 MPa. It exhibits rapid and large hardening during forming. The chemical, physical and mechanical properties are significantly improved in compounds with other elements. Primarily nickel is used in the form of alloys in the chemical, aerospace, energy, and space industries. In addition, nickel is used to coat metals to increase their corrosion resistance. Secondarily, nickel is used to increase ductility, notch toughness or to convert the structure of steels to austenitic. Table 4 below describes the basic properties of nickel. [35; 36; 37]

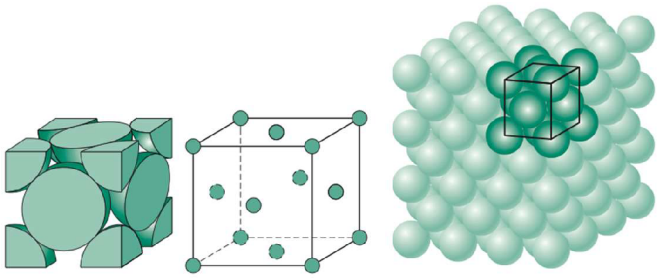

Fig. 18 Nickel atomic structure – FCC [36]

Table 4 Physical properties of nickel [36]

Properties	Mark	Value	Unit
Atomic weight	A_T	58,69	-
Melting point	T_T	1453	$°C$
Density	ρ	8908	$Kg \cdot m^{-3}$
Heat conductivity	λ	91	$W \cdot m^{-1} \cdot K^{-1}$
Thermal expansion coefficient	$\alpha_{(20°C)}$	13,3	$10^{-6} \cdot K^{-1}$
Electrical resistance	$R_{(20°C)}$	6,844	$\mu\Omega \cdot cm$
Vickers hardness	HV	638	-
Brinell hardness	HBW	700	-
Shear modulus	G	76	GPa
Tensile modulus	E	216,2	GPa
Structure	-	FCC	-
Grid constant	a	0,35168	mm

Nickel is used as an element itself in surface treatments or to modify the properties of steels. Otherwise, nickel is mainly used in the form of alloys with other elements. It can also give good and greater solubility of alloying elements than that of iron. The high solubility of alloying elements results in better material values and thus increases the availability of nickel alloys. There are elements which must be reduced to the minimum permissible by metallurgy as they significantly degrade the material properties. [35; 36; 37]

Elements that degrade the properties of nickel alloys include carbon. This forms graphite at the grain boundaries of nickel alloys when the permissible concentration is exceeded and thus reduces the mechanical properties at higher temperatures. The carbon content is reduced by metallurgy to below 0,02 wt.%. Sulfur is another element that significantly degrades material properties. At temperatures around 645 $°C$, a concentration of 0,002 wt.% results in a significant reduction in mechanical properties. Overall, the sulfur concentration in the structure is kept below 0,005 wt.%. At room temperatures, sulfur causes a reduction in ductility. Nickel alloys are most often processed in a protective atmosphere to eliminate the presence of oxygen, which forms oxides, especially binding manganese, which then does not form sulfides with sulfur and would cause a deterioration in mechanical properties. [35; 36; 37]

Manganese is added to nickel alloy to increase oxidation resistance and reduces the negative effects of sulfur at higher temperatures, as manganese forms manganese sulfide with sulfur. Another element that has positive effects on nickel alloy is zircon, which is deposited at grain boundaries in a columnar or lamellar form. Zircon is added to nickel alloys to increase mechanical properties over a wide range of temperatures. Silicon is used in metallurgy to bind residual oxygen that is present in the melt. In addition, silicon is used to increase resistance to high temperature corrosion. The usual concentration of silicon is below 0,3 wt%. As nickel becomes expensive through refining, iron is added to nickel alloys. The iron has the effect of reducing the price of the alloys. It also reduces the solubility of carbon like cobalt. [35; 36]

The addition of 2-3 wt% copper results in a significant increase in corrosion resistance in acids such as hydrochloric, sulfuric, or phosphoric acid. The most important alloying element in nickel alloys is chromium. It causes high corrosion and acid resistance. In alloys, chromium reaches a concentration of up to 50 wt. %. Chromium forms a passivation layer on the surface of the alloy. Furthermore, tungsten is added to the alloys as it increases the strength at high temperatures. It also increases corrosion resistance. The disadvantage is the high cost of tungsten due to its low concentration and complex production. Often tungsten is replaced by molybdenum, which has the same effect. Cobalt is an element that is added to the melt in the metallurgical process because of its high affinity for sulfur, with which it forms compounds that are more resistant than sulfur and nickel compounds. Furthermore, cobalt is used because it increases the solubility of carbon in the melt and thus prevents carburizing at higher temperatures. Magnesium or beryllium is used to further reduce the sulfur content. Table 5 below shows the breakdown of the different alloys into groups according to chemical composition. [35; 36; 37]

Table 5 Nickel and nickel alloy types [35]

Group	Nickel alloy types
41	*Pure nickel*
42	*Nickel-copper (Ni-Cu) with Ni ≥ 45 %, Cu ≥ 10 %*
43	*Nickel-chrome (Ni-Cr-Fe-Mo) with Ni ≥ 40 %*
44	*Nickel-molybdenum (Ni-Mo) with Ni ≥ 45 %, Mo ≤ 32 %*
45	*Nickel-iron. chrome (Ni-Fe-Cr) with Ni ≥ 31 %*
46;	*Nickel-chrome-cobalt (Ni-Cr-Co) with Ni ≥ 45 %, Co ≥ 10 %*
47	*Nickel-iron-chrome-copper (Ni-Fe-Cr-Cu) s Ni ≥ 45 %*
48	*Nickel-iron-cobalt-chrome-molybdenum-copper (Ni-Fe-Co-Cr-Mo-Cu) with 31 % ≤ Ni ≤ 45 % and Fe ≥ 20 %*

2.4.1 Nickel superalloys

If nickel superalloys are considered in terms of the number of alloying elements, which contain more than ten, they are among the most complex materials to produce. Superalloys contain large amounts of chromium, cobalt, aluminum, and titanium. In addition, small amounts of zircon and carbon are added. The major alloying elements such as chromium and aluminum significantly affect the phase diagram and solidification of the superalloy, as shown in figure 19 and 20. Chromium and aluminum form a stable oxide layer. In general, nickel superalloys have high resistance to oxidation, corrosion, and strength loss at high temperatures. They are very resistant to creep and have good fatigue properties. [35; 38; 39]

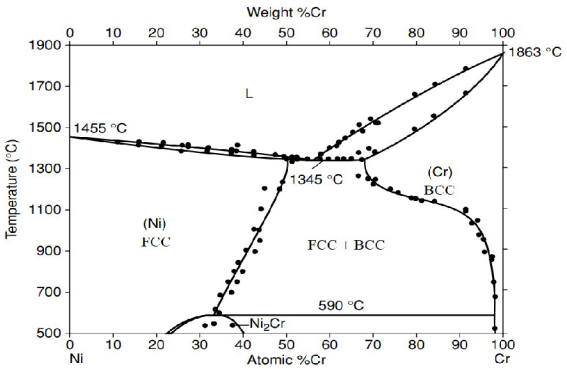

Fig. 19 Ni-CR binary phase diagram [38]

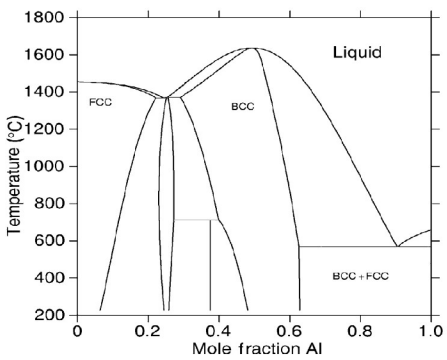

Fig. 20 Ni-Al binary phase diagram [38]

The basic matrix of nickel alloys is austenite or gamma phase denoted γ. This phase has an FCC lattice, and the matrix can be strengthened by substitution. Substitutional foaming describes the replacement of the atoms of the base lattice with atoms of another element. The strengthening is ensured by enough alloying elements up to a temperature of 810 °C. This phase contains many alloying elements such as chromium, cobalt, molybdenum. Another type of nickel superalloy matrix may be the gamma prime phase, referred to as γ'. The main alloying elements include aluminum and titanium. The last type is the gamma secondary phase, where a high content of alloying elements such as niobium and tantalum are found. Both phases have the same function, but the gamma secondary phase is preferred. Both phases have low interfacial energy. This ensures stability at high temperatures. The precipitates are dissolved at 1000 °C. Figure 21 shows the different phases. [38; 39]

Nickel superalloys are most often produced in a certain ratio of the different gamma phases. In this way the necessary physical properties are achieved. The gamma prime phase alone has the highest yield strength values, this value decreases with increasing gamma double prime phase content. At lower temperatures a combination with 10-20 % is suitable. If the content with 20 % is exceeded, the yield strength at low temperatures decreases. At a concentration of 40 %, the curve is without a drop in strength for increasing temperatures and then rises. This is due to the strengthening effect which increases with increasing temperature. The solubility of 80-100 % gamma prime waist is highest at temperatures around 900 °C. All concentrations are summarized in figure 22. [38; 39]

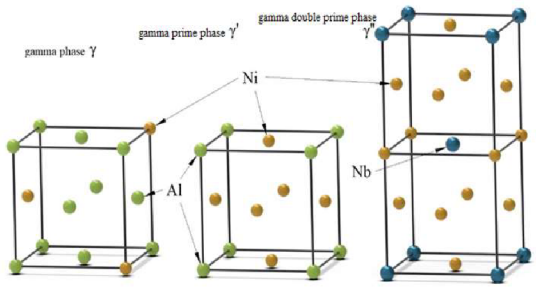

Fig. 21 Gamma phases [35]

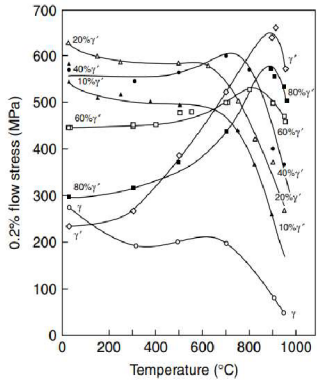

Fig. 22 Dependence 0,2 flow stress on temperature [35]

Precipitation hardening is mainly influenced by the size and shape of the hardening phases. These are mainly influenced by chromium and heat treatment parameters. With increasing time at high temperatures, grain coarsening occurs. Other phases appear in the structure, those mentioned above. These are the η or δ phases, which are formed at high titanium, tantalum, or niobium content. These have a negative effect on the hardening. Another phase that appears with high iron, chromium and molybdenum content is σ. Laves phases can form which result in a reduction in ductility of nickel alloys. Since nickel superalloys are alloyed with many alloying elements, as mentioned in previous chapters, carbides are formed. The most common carbides formed are MC, $M_{23}C_6$, or M_6C. Some of the carbides formed are stable and some are unstable. Carbides have a beneficial effect on blocking grain movement at high temperatures, depending on the position of the exclusion. If the carbides are excluded at the grain boundaries, this is a positive effect, but plasticity is reduced. The last transformation converts the carbides to the stable M_6C type. The addition of alloying elements is the last way to achieve strengthening in nickel alloys. Alloying elements such as boron and zirconium are added. The atoms of the elements occur at grain boundaries and replace vacancies. [36; 38; 40]

Boron and zirconium increase creep resistance and fracture toughness. They also change the type of fracture, which was intergranular before the addition of alloys and is transcrystalline after the addition. Nickel superalloys are hardened able. Heat treatment is therefore used. This consists of two parts. The first part is the dissolution annealing, which takes place at high temperatures around 1150-1315 °C. This is followed by rapid cooling, which results in the elimination of the supersaturated solid solution. The decomposition of the supersaturated solid solution is the second part of the heat treatment. Since this is a desirable process, the process is called artificial aging. It takes place at elevated temperatures in the range of 420 to 870 °C. The solid solution breaks down into the gamma prime phase. The whole curing process is carried out up to 7 times. Since there is a lot of internal stress after curing, another type of heat treatment is recrystallization annealing, which is done to restore plasticity after cold forming, where the original undeformed structure is restored. Recrystallisation annealing is carried out at temperatures between 700 and 1200 °C. Alternatively, stress reduction annealing is carried out directly for precipitation hardening in the temperature range 420 - 870 °C. [38; 40]

2.4.2 Weldability of nickel superalloys

When welding nickel alloys, strict requirements for material purity must be observed. Since nickel is very susceptible to forming compounds with other elements, it must be stored in areas away from other materials. Another requirement is the cleanliness of the welding surfaces. Mechanical cleaning is carried out in protective elements. The surface of the nickel alloy is cleaned with suitable agents such as acetone. Carbon, sulfur, phosphorus, oxygen, and nitrogen have a negative effect on the welding process. They are unsuitable because of the formation of low-melting eutectics. They also cause porosity in the weld joint. Elimination of these elements is possible by bonding to other elements that have a higher affinity at high temperatures or by completely reducing their content in the material. The carbon content is kept below 0,2 %, the sulfur and phosphorus content below 0,015 % and the oxygen and nitrogen content below 0,005 %. [17; 41; 42; 43]

A dissolution anneal is performed before welding to prevent hot cracks in coarse-grained structures. Adjusting welding parameters minimizes heat input. Interpass temperature for nickel alloys should not exceed 150°C. High aluminum and titanium content (≤ 5%) promotes crack formation, necessitating high-power methods like laser and electron beam. Argon and helium, or their combination (> 99,996 % purity), are commonly used as shielding gases in electric arc welding. Nickel alloys with higher iron and chromium content should be shielded with an inert gas. Titanium, aluminum, and niobium increase the susceptibility of the melt bath. [41] [42]

This reduces the corrosion resistance of the weld joint. The biggest problem in nickel alloy welding is the formation of hot cracks that occur on cooling or on repeated heating. There are three types of hot cracks. The first type is crystallization cracks, which are formed in the weld joint. The second type is casting cracks, which occur at the interface between the base material and the weld pool. The last type is polygonization cracks, which occur in the heat affected zone. Cracks are most often formed in the direction of welding. Cracks are caused by low-melting eutectics, which are caused by sulfur, phosphorus, silicon. In the figure 23 and 24 shows a hot crack. [41; 42; 44]

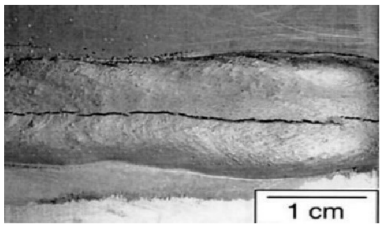

Fig. 23 Solidification crack [41]

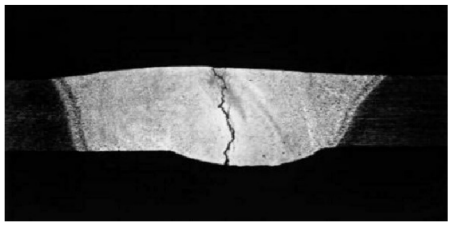
Fig. 24 Cut of solidification crack [41]

3 DESIGN AND EXECUTION OF THE EXPERIMENT

The practical part of the thesis describes the individual tests of the materials. The procedure of preparation of individual samples for the experiments, the process of experiment and finally the evaluation of individual tests are described. The first step is the evaluation of the chemical composition tests to determine the suitability of the samples that have been supplied. The samples are monitored for major element content. Next, the samples were examined under a digital microscope to observe the macrostructure, defects and then the specific areas were selected for scanning electron microscope observation of the microstructure. As the last part of practical part, microhardness, strength, and yield strength of the surfacing material are examined. Different types of samples are compared. Samples are of two types as a sample with different content of iron in welded overlay. The samples were welded with different parameters, which are reflected in the individual properties of the material being welded. The individual tests are chosen in a certain continuity, where the results of the previous measurements are used to evaluate the following measurements.

3.1 Base material – 16Mo3

Molybdenum heat-resistant structural steel 16Mo3, also known as W.Nr.1.5415 or ČSN 15 020, is a type of steel that is highly resistant to high temperatures, creep, and high-temperature corrosion. The steel 16Mo3 has ferritic-perlitic structure. This material can be easily machined and is ductile both at hot and cold temperatures. One of the main advantages of this material is its excellent weldability using standard welding techniques such as TIG, MIG/MAG. With a higher concentration of chromium and molybdenum, this steel possesses properties that are highly suitable for use in industries such as heating, power, oil, gas, or chemicals. The chemical composition of 16Mo3 steel is shown in table 6 below. Mechanical properties and chemical composition are described in attachment 1. [32] [45]

Table 6 Chemical content of steel 16Mo3 [46]

[%wt]	C	Si	Mn	P	S	Cr	Mo	Ni	N	Cu
16Mo3	0,12-0,20	0,35	0,40-0,90	0,025	0,01	0,03	0,25-0,35	0,30	0,01	0,30

At present, the primary application of this material is in the manufacturing of industrial equipment such as boilers, steam lines, heat exchangers, and pressure vessels. Table 7 presents the mechanical properties of 16Mo3 steel at a temperature of 20°C.

Table 7 Mechanical properties of steel 16Mo3 [45]

Tensile modul of elasticity	212 GPa
Yield strength	380 MPa
Tensile strength	440 MPa
Hardness	150 HB
Ductility	30 %
Impact work ISO-V	31 J
Application temperatures	-20 – 530 °C

Based on the information provided, 16Mo3 steel is commonly utilized for applications that involve high temperatures. When subjected to these temperatures, the material enters a state called "creep," which is characterized by slow deformation caused by prolonged exposure to elevated temperatures. Heat resistance, a property of steel, is defined by this creep behavior. Table 8 displays the creep strength limits for 16Mo3 steel at various temperatures and loading times. [32; 45]

Table 8 Creep strength for different temperatures and loading time [45]

Temperature [ºC]	Creep strength for 10^4 hour [MPa]	Creep strength for 10^5 hour [MPa]	Creep strength for 10^6 hour [MPa]
450	298	239	217
470	247	178	159
500	171	101	84
510	147	91	69
530	102	53	45

3.2 Protective material Inconel 625

Inconel 625 has high strength without prior heat treatment. Equilibrium temperatures range from -200 to 980 °C. The chemical composition of the nickel superalloy guarantees high corrosion resistance in a wide range of corrosive environments. It is mainly resistant to pitting, crevice corrosion. This material finds a wide range of applications in the chemical, energy, aerospace, and space industries. For the problem addressed in this work, Inconel 625 is suitable for welding the protective layer of membrane walls, evaporators, and preheaters. As mentioned earlier, the welded layer on the membrane wall does not need further heat treatment. As the degree of dilution of the coating material with iron increases, it is corrosion resistance decreases. For the problem of welding the layer on the membrane wall, a material in the form of a wire called Inconel Filler Metal 625, which is designed for TIG/MIG welding processes, is used. More information is described in attachment 2. [47; 48]

The chemical composition of the Inconel 625 is shown in table 9, where the largest amounts are represented by the elements Ni and Cr. Alloying Cr and Al yields superalloys the required anticorrosive and antioxidant properties. These then form a protective layer in an oxygen environment, e.g., Cr_2O_3 and Al_2O_3. The elements Ti and Al are the basis for formation of γ' curing phase. Small amounts of other elements may also be present in superalloys. Beneficial elements that contribute to grain boundary strengthening include C, Zr and B. On the other hand, harmful elements include, for example, O, H, N, He, as residual gases, as well as Pb, Sb, Cu, Ag, as impurities. [47; 48]

Table 9 The compositions (in wt %) of Inconel 625 [47]

Ni_{min}	Cr	Co	Mo	W	Nb	Al	Ti	Ta	Fe	Hf	C	B	Zr
58	21,5	-	9,0	-	3,6	0,2	0,2	-	2,5	-	0,05	-	-

Inconel 625 belongs to the D-2 group. This refers to materials that are hardenable by an ageing process that maintains high hardness and strength. When low hardness of the material, such as drilling and tapping operations, the material is machined in the unaged. The material with the lowest hardness and ease of machinability is in chemical and heat treatments such as dissolution annealing followed by quenching or air cooling. This process is necessary in the roughing process in the aged state. Table 10 lists the basic mechanical properties Inconel 625. [47; 48]

Table 10 Mechanical properties of Inconel 625 [47]

Tensile strength	965 MPa
Yield strength	490 MPa
Tensile modulus of elasticity 20 °C	207 GPa
Ductility at 20 °C	50%
Creep strength	360 MPa

3.3 Welding of Inconel 625 protective layer

The primary factor considered when selecting the appropriate welding method was the level of iron present on the surface of the coating layer. Using a conventional MIG pulsed current method with an EWM source, manual welding achieved 5,45% Fe, robotic welding achieved 4,3 %. The CMT method resulted in lower levels of iron, with 1,9 % achieved for manual welding and 1,35 % for automated welding. Monitoring the amount of iron is crucial for ensuring the corrosion resistance of the coating. Due to the lower mixing achieved with the MIG method, it was chosen, specifically the CMT source Fronius TPS 500i. The CMT torch used in this method has a wire oscillation frequency of up to 90 Hz. The additive material used is from ALUNOX, designated AX-625, and its chemical composition is given in table 11. With a wire diameter of 1,2 mm, a sufficient weight of metal can be welded. Other specification has been shown in attachment 3.

Table 11 Chemical composition of welded material from company Alunox [49]

Element	Ni	C	Cr	Mo	Mn	Si	Nb+Ta	Fe
%wt	63,8	0,02	22	9,0	0,2	0,2	3,3	1,5

To optimize the welding process for this material, a gas mixture consisting of argon, helium, hydrogen, and carbon dioxide is recommended. The gas from Linde, called Cronigon Ni10, has a chemical composition that is listed in table 12, and the small amount of carbon dioxide can enhance the arc's stability. Helium is included in the mixture to increase heat transfer to the weld area and facilitate wetting. Adding hydrogen can enhance the wettability and fluidity of the weld metal, but it is important to note that it can also have a non-negligible impact on the ductility of the final product.

Table 12 Chemical composition of shielding gas

Element	Ar	He	H	CO_2
%	67,945	30,0	2,0	0,055

The welding of the Inconel 625 protective material layer took place at the workplace of Šmeral s.r.o. The workplace was equipped with a handling device for welding the coating on the membrane wall in the length of six meters. The assembly also included a cooling device that pumped water through the membrane wall for cooling, thus ensuring minimal dilution and a small heat affected area. The handling equipment is shown in figure 25. In addition, the entire system was fitted with a Fronius TPS 500i power supply, which is shown in figure 26. This device operates with software that uses synergies that optimize many parameters that can reduce dilution and the size of the thermally affected area.

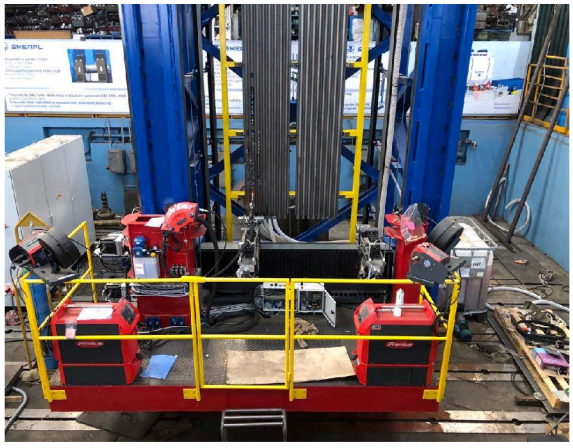

Fig. 25 Handling equipment

Fig. 26 Fronius TPS 5OOi [50]

For the welding of the samples, synergistic curve with the designation 3921, which is designed for Inconel 625, was used. In addition, arc length correction and pulse dynamics correction are considered. The arc length correction ranges from -10 to +10. When changing from the original 0 to positive values, time of returning of the wire is reduced. Speed of movement is the same and the distance of the wire end from base material is reduced. Because the time is reduced, frequency of metal transfer is increased. The shorter distance reduces voltage and heat input. Conversely, when the return time is set to negative values, the return time is increased and the arc length is increased, resulting in increased voltage and energy loss. The metal droplet to be melted is larger and the frequency is smaller. The pulse dynamics correction (PDC) is adjustable from -10 to +10. It simulates inductance in the circuit. And controls the magnitude of the short circuit current. The current is increased for negative values and decreased for positive values. The consequence of reducing the current is a less stable arc, but less spatter and mixing. Increasing the short circuit current results in higher mixing, better arc stability and increases the contact angle between the lead and the base material.

The wire feed rate is mathematically synergistically related to current and voltage. In the CMT method, the speed is not constant as in conventional methods. The process is digitally controlled, and the device regulates itself at any time in case of non-compliant parameters. Pulse dynamics correction and arc length correction also affect the wire feed rate. To protect the know-how of the technology developed by BUT, some parameters will not be described precisely. Table 13 describes the allowed welding parameters.

Table 13 Welding parameters

I [A]	U [V]	v_s [mm·min^{-1}]	v_v [m/min]	divergence [mm]
180	17	267	6,4	10-20

Part of the work was to develop a welding procedure specification (WPS), which summarizes all the information about the welding process. There is information about the additive material, shielding gas, welding parameters and the final welding process. The WPS is shown in attachment 3.

3.4 Analysis of chemical composition

Optical emission spectrometry (OES) is a widely used method for chemical analysis of a wide range of metallic materials. This technology is mostly used in the metallurgy and metalworking industries. Here, a rapid and high-quality determination of the chemical composition of the sample is required. For example, in foundries where molten steel samples are analyzed. As the previous description suggests, no complex sample preparation is required. It is necessary to have a clean and flat surface but can do without the necessary grinding and polishing. The principle of this technology is based on the use of the UV-VIS electromagnetic spectrum, or from 130 nanometers to 800 nanometers. OES can analyze a wide range of elements from hydrogen to uranium in solid metal examples covering a wide concentration range, giving very high accuracy, high precision, and low detection limits. [51; 52; 53]

The principle is based on the use of an electric discharge that is generated in an excitation generator. The high voltage discharge ionises the atmosphere between the tungsten electrode and the sample, this causes the atmosphere to become conductive. The atmosphere is made up of an inert gas, most commonly argon. The gap between the sample and the electrode is in units of millimeters and during the measurement a low impedance and stable current is generated. In a short moment of time a discharge is generated which heats the material, then the material vaporizes and ionizes. Two forms of electrical discharge can be generated. Either an arc-like on/off event or a spark-like series of multi-discharge. Arc excitation consists of a continuous

current flow for several seconds. In spark excitation this current flow is interrupted with a specific frequency from 100-1000 Hz. After the electric arc and light radiation are generated, the optical device captures the light, which is split through a diffraction crystal (grating) into individual wavelengths corresponding to the element contained in the sample under examination. The detector then measures the intensity and the specific wavelength. In the last step, the computer obtains and records the intensities and evaluates them according to predefined calibrations. The scheme of OES is shown in the figure 27. [53; 54]

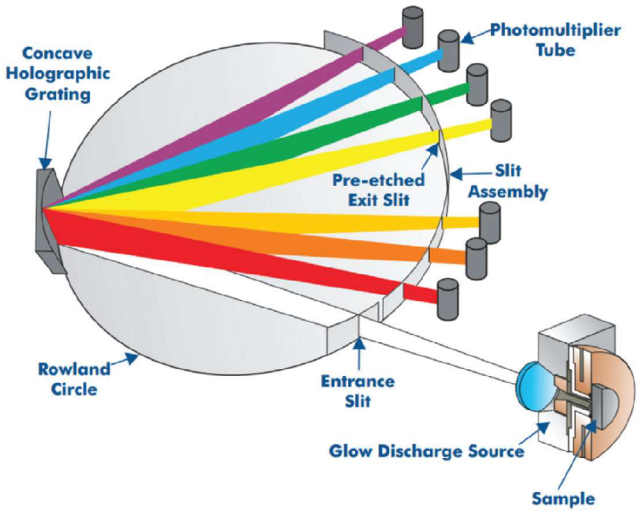

Fig. 27 Scheme of OES [53]

Every element emits a series of spectral lines corresponding to the different electron transitions between the different energy levels or shells. Each transition produces a specific optical emission line with a fixed wavelength or energy of radiation. For a typical metallic sample containing iron, manganese, chromium, nickel, vanadium etc., each element emits many wavelengths, leading to a line-rich spectrum. For example, iron emits just over 8000 different wavelengths so choosing the optimum emission line for a given element in a sample is important. The characteristic light emitted by the atoms in the sample is transferred to the optical system where it is split into its spectral wavelengths by the high-tech grading, the grading contains up to 3600 grooves per millimeter. Next the individual spectral line peak signals are collected by detectors and processed to generate a spectrum showing the light intensity peaks versus their wavelengths. This means that OES provides qualitative information about the sample measured, however, OES is also a quantitative technique. The peak wavelength identifies the element, and its peak area or intensity gives an indication of its quantity in the sample. The analyzer then uses this information to calculate the sample's elemental composition based on a calibration with certified reference material. The whole process, from pressing a start button or a trigger to getting the analysis results, can be as quick as 3 seconds or it can take up to 30 seconds for a full accurate quantitative analysis, it all depends on the analyzer used, the range of elements measured and the concentrations of those elements. Compared to other analytical techniques, OES has many advantages: it's fast and relatively easy to use, it measures a wide range of elements and concentrations in many different types of materials, including important elements such as carbon, sulfur, phosphorous, boron and nitrogen. It's extremely accurate when measuring low levels of trace and tramp elements, and it's low-cost compared to other techniques. For trace analysis of metals OES is the preferred method, OES is also currently the only method which can analyze carbon and nitrogen on site, out of the laboratory. [51; 53; 54]

To evaluate the chemical composition of the Inconel 625 coating layers, two types of samples were welded and prepared. As an approximation, the chemical composition was determined using a Thermo Scientific Niton XL3t XRF Analyzer portable spectrometer (Fig. 28), on site after welding. It was found that the first type of samples contained a dilution of the coating layer of about 1% iron and the second type of samples contained about 5 % iron. Since the analysis using a portable spectrometer is not very accurate, the chemical composition is analyzed on an ARL iSpark Series Optical Emission Spectrometer (Fig. 29), which achieves higher accuracy results. A more detailed technical specification is described in attachment 4. This method was used because the samples being investigated are heterogeneous, as the base material 16Mo3 is completely different from the Inconel 625 design.

Fig. 28 Niton™ XL3t XRF Analyzer [55]

Fig. 29 ARL iSpark™ Series Optical Emission Spectrometer [52]

A total of 8 samples were prepared for measurement, 4 pieces of each iron content in the surface layer with a length of 40±2 mm, the length was chosen because of the working space of the instrument. Sample preparation was carried out on a HERZOG HS 200 grinder (Fig. 30.) with a HERZOG A24 F8V grinding wheel (Fig. 31). The material was dressed at a thickness of 0,2 mm to create a sealing surface and to remove oxides from the surface that would distort the results. A total of 3 measurements were taken on each sample, for a total of 12 measurements for each sample type, as it shown in the figure 32.

Fig. 30 HERZOG HS 200 [56]

Fig. 31 HERZOG A24 F8V

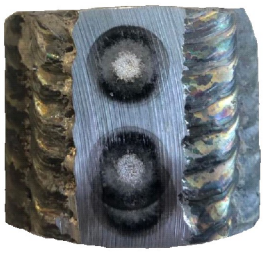

Fig. 32 Sample after analysis

The entire instrument must be calibrated before the actual measurement of the samples. OES spectrometers are very sensitive devices and without maintenance and recalibration their accuracy may decrease. OES spectrometers use relative value measurements, so it is important that the amount and concentration of the substance is correct. Certified materials or reference samples are used for this purpose. Reference samples are chosen according to the basis of the material. In this case, a reference sample with a Ni-Cr base was chosen. To fine tune the calculation, this procedure should be performed just before running one or more samples of a given alloy type. Once the correct sample type has been obtained, the optimum level of accuracy of the baseline calibration should be checked with the CRM before starting. The user must ensure that he has a large quantity of recently prepared and easily measured materials ready, as would be common when using control samples for recalibration. For all its advantages, type standardization should not be used as a global correction technique for the analysis of materials with significantly different chemical compositions.

3.4.1 Evaluation of the results

Two types of samples were evaluated. For both types, the same elements were evaluated and selected according to their influence on the properties of the coating layer. Inconel 625 has a matrix consisting of nickel and chromium. The molybdenum, niobium and titanium content were also monitored. Iron is evaluated as the most important element in terms of corrosion resistance in the structure. The individual elemental contents of the structure are described in the attachment 5. The average values of the elemental contents have been plotted on a chart 1. The contents of the major elements nickel and chromium are very similar in both samples. The same is also true for molybdenum, titanium, and niobium. The biggest difference in elemental content is in the case of iron. In the samples I, the average value is 2,76 wt% and in contrast the average value for the samples II is 4,79 wt%.

Chart 1 Elemental composition of Inconel 625

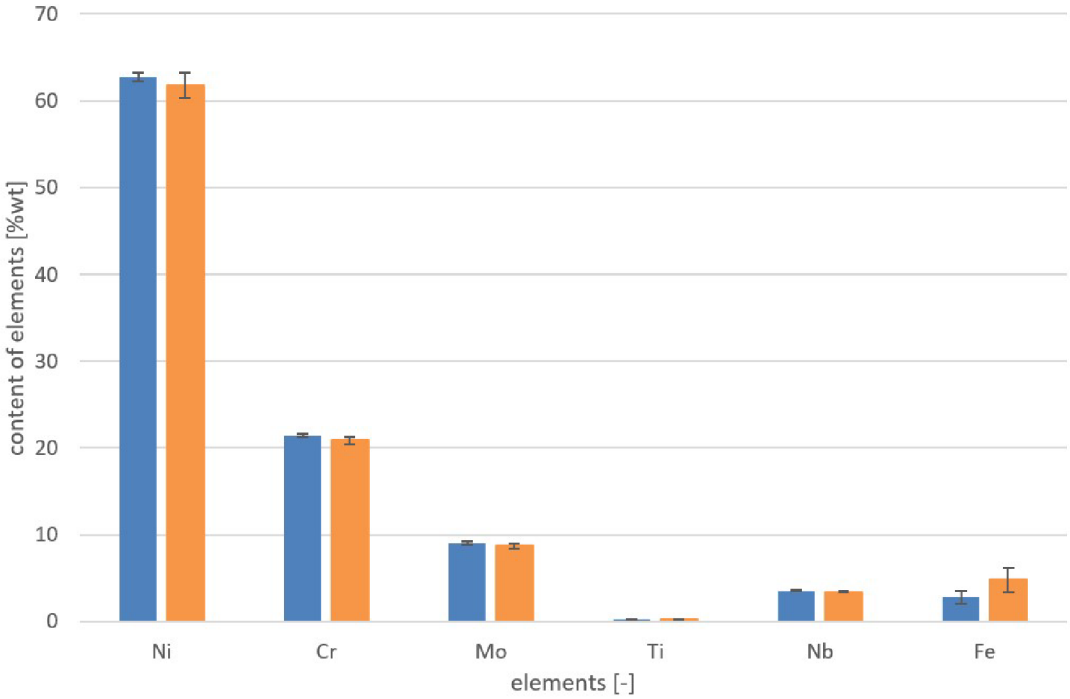

Next, the average values ($\bar{x}$) of the individual concentrations were calculated. The standard deviation (σ) values, which describes how the individual measured values differ from the mean value. Relative standard deviation ($\frac{\sigma}{\bar{x}}$), which describes the degree to which the values deviate from the mean value. All values are described in Table 14.

Equation 2 average value:

$$\bar{x} = \frac{1}{n} \cdot \sum_{i=1}^{n} x_i \tag{3.1}$$

where: $\bar{x}$ – average value of chemical composition [-]
x_i – value of individual measurements [-]
n - – number of measurements [-]

Equation 3 standard deviation:

$$\sigma = \sqrt{\frac{1}{(n-1)} \cdot \sum_{i=1}^{n} (x_i - \bar{x})^2} \tag{3.2}$$

where: σ – standard deviation [-]

Equation 4 relative standard deviation:

$$\frac{\sigma}{\bar{x}} = \frac{\sigma \cdot 100}{\bar{x}} \tag{3.3}$$

where: $\frac{\sigma}{\bar{x}}$ – relative standard deviation [-]

Table 14 Values of AV, SD, RSD

[%wt]	Ni	Cr	Mo	Ti	Nb	Fe
$\bar{x}$	67,78287	21,40996	9,013903	0,183962	3,519779	2,764138
σ	0,520874	0,186678	0,156939	0,003878	0,075448	0,702649
$\frac{\sigma}{\bar{x}}$	0,829643	0,871919	1,741082	2,107909	2,143554	25,4202
[%wt]	Ni	Cr	Mo	Ti	Nb	Fe
$\bar{x}$	61,75852	20,85678	8,683198	0,184282	3,142059	4,792178
σ	1,463556	0,450628	0,265835	0,022861	0,053173	1,318084
$\frac{\sigma}{\bar{x}}$	2,369804	2,160583	3,061492	12,40553	1,558381	28,75695

From the results obtained from the measurement of the chemical composition of Inconel 625 drill bit, it can be found that the sample with 1%wt of steel in welded layer is better for practical use. It achieves a lower dilution of iron in the structure with an average value of 2,76 wt%. In contrast, the samples with 5 wt% of iron in the structure have an average iron content of 4,79 wt%, which results in lower corrosion resistance and a lower lifetime of the coating layer on the membrane wall.

3.5 Analysis of macrostructure of base material and welded layer

All samples used in the experiments shall be specially prepared for the evaluation of, macrostructure, microstructure, and microhardness. All samples were cut on a LECO MSX205 saw, which is shown in figure 33. The cutting wheel used was a Struers type 30A25 wheel, which is shown in figure 34. During the cutting of the specimens, great emphasis was placed on cutting force and cooling the material to avoid thermal effect on the material and thus deterioration of the material structure, demineralized water was used as the coolant.

Fig. 33 LECO MSX205 [57]

Fig. 34 Struers 30A25 [58]

The specimens used for the determination of macrostructure, microstructure and microhardness shall have a specially prepared surface which shall be ground, polished and finally etched to show the structure. The specimens, which were cut on a ripping saw, were then lightly beveled at the edges after cutting on a Struers LaboPol-60 grinding machine, which is shown in figure 35. After the sharp edges of the samples were ground down, the samples were cleaned in isopropanol and then handled in laboratory gloves until the end of the process. The samples thus prepared were then split in half, where the first half of the samples were pressed into bakelite pellets and the second half into iron pellets. The different metallographic pellets were chosen because of their use on the optical and electron microscope. Another reason is for use in etching, where samples pressed in bakelite pellets were used to etch the Inconel 625 structure. Samples pressed in iron pellets were used to etch the 16Mo3 structure. The samples were molded at a pressure of 2600 kPa and a temperature of 180 °C in a Struers Citopress-30 machine, which is shown in figure 36. After crimping, the edges of the metallographic samples were ground again.

Fig. 35 Struers LaboPol-60 [58]

Fig. 36 Struers CitoPress-30 [58]

The samples were ground and polished on a LECO PX500 machine, which is shown in figure 37. Standard parameters were set on the machine depending on the type of grinding and polishing wheel. The CAMEO Platinum 1 Blue wheel (comparable to 120 to 180 grit) was selected as the first wheel. CAMEO Platinum 2 Green (comparable to 220 to 280 grit) was selected as the second grinding wheel. The third abdominal wheel used was CAMEO Platinum 3 Yellow (comparable to 400 grit). The last abrasive wheel used was CAMEO Platinum 4 Red (comparable to 600 grit). All the abrasive wheels used are shown in figure 38. The advantage of using LECO machines and CAMEO abrasive wheels is the standardized parameters, which resulted in high quality scratch-free cuts. All samples were ground with individual pressure for 3 minutes.

Fig. 37 LECO PX500 [59]

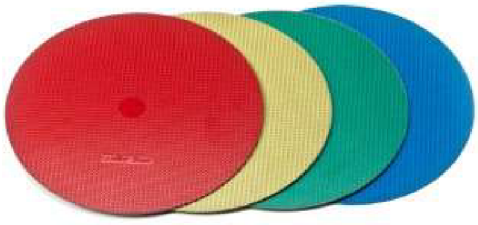

Fig. 38 Grinding discs CAMEO Platinum [60]

After grinding the samples, polishing follows. Polishing is performed in the same way as grinding on the LECO PX500. Only the discs are changed, in this case a Brown Technotron polishing disc, which is shown in figure 39, was used together with LECO PREMIUM GRADE with diamond abrasive 3 to 1 μm. The samples were polished with individual pressure twice for 2,5 minutes. After grinding, all samples were cleaned in the laboratory ultrasonic cleaner POLSONIC SONIC-2 shown in figure 40.

Fig. 39 Brown Technotron [60]

Fig. 40 POLSONIC SONIC-2 [61]

The last part of sample preparation was chemical etching. Since the samples are heterogeneous in that they contain Inconel 625 alloy and 16Mo3 base material, it was very difficult to find an etchant that would etch both materials sufficiently without damaging each other. As mentioned at the beginning of this chapter, the samples that were pressed into the Bakelite pellets were used to etch the Inconel 625 structure were etched with Marble (4g $CuSO_4$, 20 ml HCl, 20 ml H_2O) and the samples pressed into the iron pellets to etch the 16Mo3 steel structure were etched with 2%Nital. (a solution of HNO_3 in C_2H_6O). All samples were etched between 10 and 20 seconds. The method of etching the surface of the samples was by rubbing.

3.5.1 Results of macrostructure

For the resulting macrostructure, specimens containing a circular section of Inconel 625 coating material on a base material of 16Mo3 membrane wall were selected. The structures of both the base material and the coating layer on both types of specimens. The main parts that are monitored on the samples are the size of the thermally affected region, the structure, defects in the thermally affected region, and defects in the transition between the base material and the coating layer will be monitored. Defects in the coating layer are monitored, which may include cracks, bubbles, imperfections.

Samples for macrostructure evaluation were photographed on a Keyence VHX-5000 digital microscope. It has been shown in figure 41. The microscope is equipped with a desktop computer for displaying the images and for manipulating the microscope. The Keyence VHX-500 in our case includes the Universal Zoom Lens VH-Z20UR/Z20UT. It can also measure the distances of individual points on a straight line, on a circle, this measurement is used when measuring the size of a thermally affected area. The microscope has an HDR software program to improve the image quality.

The stitching images program was used to create panoramic images. In addition, the microscope has a 3D surface structure measurement capability, where stitching of many images with a shallow depth of field is used, where the software stitches the individual images together to create a 3D map of the surface structure.

The sample I for evaluation of 16Mo3 macrostructure was taken from the top of the semicircle, which forms the functional part of the incineration boiler wall. The sample was photographed in panorama mode to provide an overall view of the sample and to highlight the locations of individual defects. As can be seen in the figure 42, there are cracks in the transition layer. The image shows a thermally affected area.

Fig. 41 Keyence VHX-5000 [62]

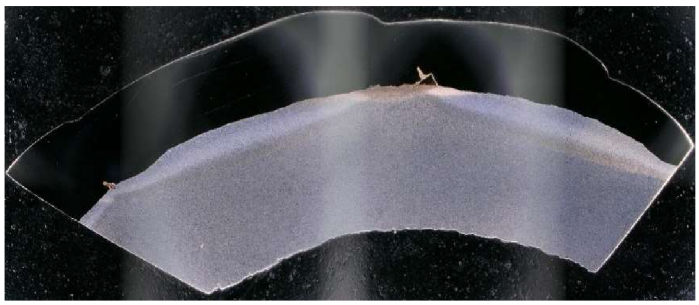

Fig. 42 Panorama of welded specimen

The size of the heat affected area is shown in figure 43. The specifin shape may be due to the specific welding parameters. The average size of the heat affected area is calculated by arithmetic averaging, where the resulting value is 1,376 mm.

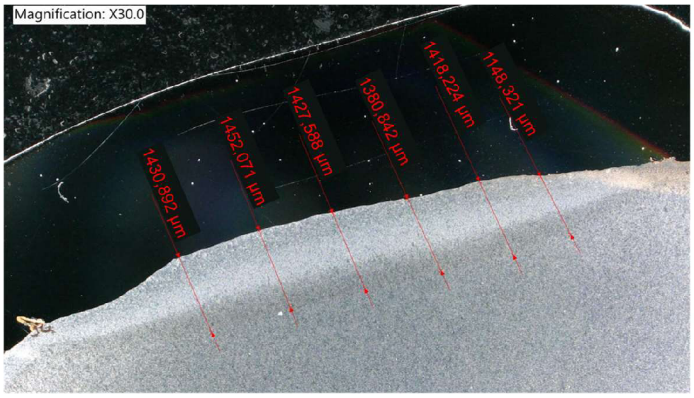

Fig. 43 Measure of HAZ I

The cracks are shown in Figures 44 and 45. The images were taken at 100x magnification. The yellow areas around the cracks are visible, which are formed during the preparation of the samples during etching. Sharp edges are visible near the cracks, which may indicate future crack propagation and thus reduce the service life of the membrane wall coating.

Fig. 44 Detail of crack I

Fig. 45 Detail of craft II

The sample I for the evaluation of the Inconel 625 filler material was created in the same location as for the evaluation of the 16Mo3 base material. Again, a panoramic image of the entire specimen was taken to locate the defects and the size of the heat affected area, which is shown in figure 46. In this image, the light streaks from the illumination are not as noticeable, as a different illumination level was chosen for the specimen. There are characteristic dark spots on the coating layer that are caused by the reflection of the lens from the coating layer.

Fig. 46 Panorama of Inconel 625 layer

A single crack was formed in the transition between the base material and the Inconel 625 coating, which is shown in figure 47. The vicinity of the crack is characteristic because of the metallographic preparation of the samples. The image was taken under 100x magnification.

Fig. 47 Detail of crack in specimen I

According to the images above, since the individual pairs of samples were taken from the same location, the errors are duplicated, or the errors that are in the images of the transition of the 16Mo3 base material and the Inconel 625 coating layer are the same ones that are in the images with the etched Inconel 625 coating layer structure. The discontinuities could have been caused by rapid cooling of the individual layers, this could have led to rapid shrinkage and crack formation.

The sample II for evaluation of 16Mo3 was taken from the top of the semicircle, which forms the functional part of the membrane wall, was photographed in panorama mode to get a general view of the sample and to highlight critical areas, the panorama is shown in the figure 48. In the image, it can be seen the lighter stripes that are created by gradually moving the lens over the sample area and the light that shines on the workspace will create the lighter areas in the image. In the bottom left corner of the sample there are visible scratches that were created when the sample was sanded, these scratches do not affect the evaluation. The heat affected area can be clearly seen, which has a specific shape that is created by the welding process.

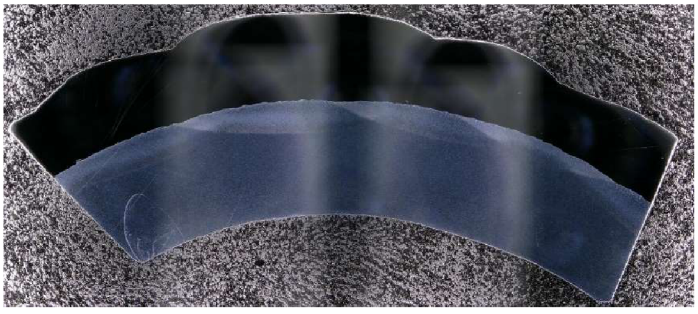

Fig. 48 Panorama of sample with 16Mo3 structure

The sample was further examined in more detail under 50x magnification. No defects were found in the structure of the base material 16Mo3. The size of the thermally affected region was evaluated in figure 49. The average value of the thermally affected region was calculated as the average of the measured values, which has a size of 1,369 mm.

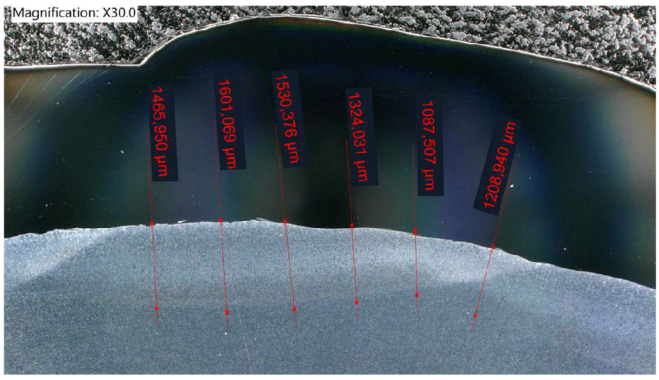

Fig. 49 Measure of HAZ

For the evaluation of macrostructure of Inconel 625 samples were taken from the same location as for the evaluation of the base material. A panoramic image was created, which is shown in the figure 50. The dark streaks in the structure of Inconel 625 are created by photography, where there reflects the lens from the glossy structure of the layer.

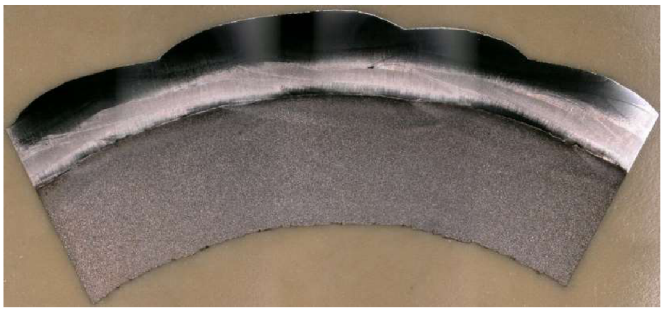

Fig. 50 Panorama of sample with Inconel 625 structure

It can already be seen from the panoramic photo that there are layers of overburden between the layers. This defect is shown in more detail in the figure 51, where a zoom of 100x is selected. The dendritic structure of the coating layer can be clearly seen here, which is stretched due to the gradient cooling in the direction of the layer thickness, and the transition boundary between the layers can also be seen here, since the Inconel 625 layer was double layered.

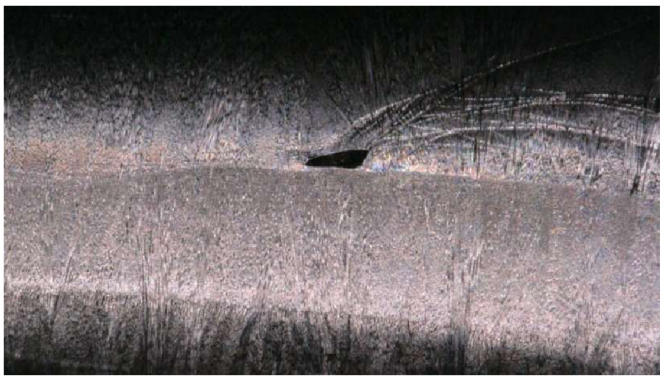

Fig. 51 Detail of crack between the layers 100x

The detail of the crack has been shown in the figure 52. The figure was created with a magnification of 200x. It is possible to give a good indication of the crack edges from which the crack could propagate further and thus reduce the service life of the overburden wall. In this case, the dendritic structure of the material is even more noticeable and the continuity between the layers can be clearly seen, as well as the fact that the upper coating layer differs in its elongation, which is due to the different heat dissipation from the welding site.

Fig. 52 Detail of crack between layers

The last defect revealed in the macrostructure images is a bubble. This defect is located in the welding overlay. The bubble was caused by rapid cooling of the welding overlay after welding and it is shown in the figure 53. The figure was taken at 200x magnification. The source of the bubbles in this case is most likely residual moisture. During welding, the material is heated to a high temperature, which causes the gas inside the material to heat up and expand. As a result, a bubble is formed, which can manifest itself in different shapes and sizes. Bubbles in the form of defects in the material are undesirable because they weaken the strength and integrity of the material. They can reduce the resistance of the material to mechanical stress and can also act as stress concentration points, increasing the risk of cracks and material failure. The presence of bubbles can result in reduced component life and reliability.

Fig. 53 Detail of the bubble in overlay

3.6 Analysis of microstructure of base material and welded layer

A scanning electron microscope (SEM) is a complex, sophisticated device that consists of three basic parts: an electron source, electron optics, and a part for detecting the products of electron collisions with a given sample, as shown in the figure 54. With the SEM microscope, it is possible to observe and characterize organic and non-organic materials, as well as to observe not only the surface topography, but also to analyze the crystal structure, chemical composition, and electronic properties of the sample down to a depth of 1μm. The resolution of current SEM microscopes is about 1 nm and magnification up to $1 \cdot 10^6$. The first SEM microscope was designed in 1937 by scientist Manfred von Ardenne. The principle on which this microscope works is more complex than its early predecessor, the TEM microscope. The TEM microscope shines a beam of electrons through a given specimen, where individual atoms of the specimen can be observed, but a small sample thickness is required. In contrast, the SEM microscope scans a given surface in lines and the system converts the recorded signal into an image of the sample properties. The probe with which the surface is scanned forms a beam of high-speed primary electrons that is ideally focused on the surface by the imaging system. The detectors are positioned above the sample. [63; 64; 65]

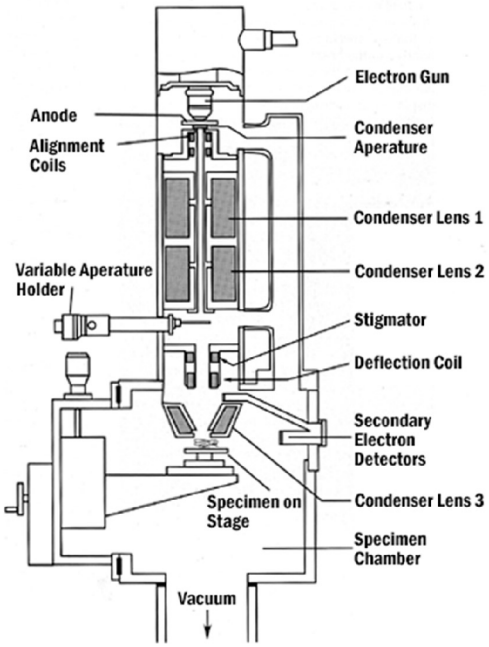

Fig. 54 Scheme of SEM microscope [64]

Electron emission occurs at the cathode, which is supplied with a high negative voltage of 0,1 to 30 kW. The resulting electrons are accelerated by an electromagnetic field to the anode. Tungsten tips or filaments are most often used as the cathode. A high vacuum must be maintained throughout the process to prevent oxidation of the electrodes. The resulting electrons are focused on the sample surface by an optical system. Electromagnetic coils and lenses are used. The most important part is the condenser lens, which creates a parallel parsec of electrons behind the anode. BSEA stigmator is used to eliminate lens errors and apertures are used to capture scattered electrons. As mentioned above, a high vacuum is required for good quality electron microscope images. The fewer particles there are in space, the fewer the number of scattered electrons. Turbo vacuum pumps are used to create vacuum. Detectors are used to capture the reflected secondary electrons. In a detector, the electrons emit photons that have a characteristic wavelength according to the element, then the photons are converted into an electrical signal. The detectors are placed over the sample. [64; 65]

Electron sample interaction used electrons that are focused on the surface of the sample and interact with it to produce different signals. Depending on the choice of signal detection, the SEM microscope can observe the surface, the chemical composition, or the crystal structure, for example. The correct signal detection is determined by the choice of detector. When an electron hits the surface of a component, the electron penetrates below the surface of the component and is scattered to form a signal. The volume of this sample where scattering occurs is called the interaction volume and is shown in figure 55. This volume increases with increasing accelerating voltage and changes with increasing atomic number. [64; 65]

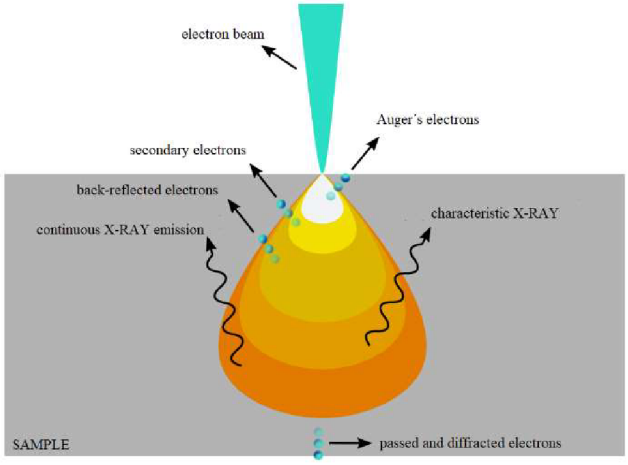

Fig. 55 Scheme of interaction volume [65]

Secondary electrons are produced by collisions of the electron beam with the atoms of the sample. The original electrons from the beam lose energy and transfer it to the sample atom. The electrons are excited, and the sample is ionized. These excited electrons are called secondary electrons. These electrons have low energy and can escape from a small depth in the sample. They are used to show surface roughness and texture. The Everhart-Thornley detector is used to detect secondary electrons. Backscattered electrons (BSE) are produced by elastic collisions. These electrons provide additional information on chemical composition and crystallographic structure compared to secondary electrons. Detectors used to detect these electrons are like those used to detect secondary electrons but have shielding to eliminate the presence of secondary electrons. Auger electrons are created when an electron is moved from higher energy levels to lower energy levels to reduce the total energy, the excess kinetic energy is transferred to another electron, which is then able to leave the atom, and this is called an Auger electron. These electrons describe the chemical composition of the sample. Characteristic X-RAY is characteristic of each chemical element. Thanks to X-RAY it is possible to determine the chemical composition of a sample. The principle is like the Auger electron, but the energy released is emitted in the form of a photon. As additional electrons can detect passed electrons in very thin samples. [64; 65]

3.6.1 Results of microstructure

The same samples were selected for microstructure evaluation as for macrostructure evaluation. The samples were chosen because we already know from the macrostructure evaluation what to look for and where to focus the electron microscope. Samples were selected from the top of the semicircle, where the microstructure of the Inconel 625 coating layer as well as the 16Mo3 base material will be observed. Areas of interest will include the individual structures found on the samples, as well as defects that reduce the life of the membrane walls.

An Apreo 2 scanning electron microscope was used to evaluate the microstructure and is shown in figure 56. The Apreo 2 has an accelerating voltage of up to 15 kV at low vacuum, thus achieving a resolution of up to 1,8 nm. At high vacuum it has an accelerating voltage of up to 30 kV, where a resolution of up to 0,7 nm is achieved. Apreo 2 includes a handling stage that allows tilting about all three axes, thus achieving the ability to view the sample from all angles, up to a tilt of 60º. ETD, DBS, low vacuum SE, EDS detectors were fitted as detectors. The vacuum system reaches values up to $6{,}3 \cdot 10^{-6}$ mbar.

Fig. 56 Apreo 2 SEM [63]

In the previous chapter, which dealt with the macrostructure evaluation, it was found that the structure of each material, whether it was the base material 16Mo3 or the Inconel 625 coating layer, did not differ from each other. For verification, the individual samples were examined on an Apreo 2 electron microscope, and it was confirmed that there was no structural difference between the samples. The following section will focus on the evaluation of the microstructure of both types of samples. Furthermore, the microstructure evaluation will focus on the evaluation of defects. More information is described in attachment 6.

According to the macrostructure evaluation, it was found that the individual structures of the Inconel 625 plating layers do not differ from each other. To confirm this claim, the samples were observed under an Apreo 2 scanning electron microscope (SEM) where this view was confirmed. Thus, in the following section, the structure that was better prepared for SEM observation will be evaluated. Furthermore, defects in the form of cracks were evaluated.

First, the structure at the transition between the materials was monitored. In figure 57, the 16Mo3 base material can be seen over etched on the right side. This was created during preparation of the samples. A more contrasting structure of Inconel 625 can be seen on the boundary, which is less etched further away from the boundary, this may be due as sample preparation. The continuing structure continues to be more pronounced and there is clearly visible increasing dendritic structure.

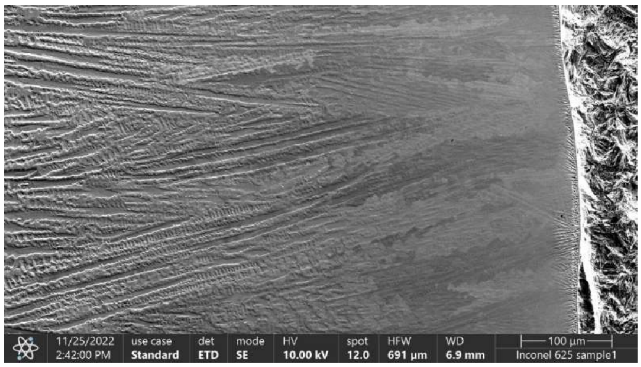

Fig. 57 Boundary between 16Mo3 and Inconel 625

The continuing dendritic structure can be clearly seen in figure 58. There can be clearly seen the growth of the dendritic grains, which have a characteristic tree-like structure that is distinctive in its shape, where main branch from which grow smaller perpendicular branches. The elongation of the structure is due to the heat dissipation from the point of welding and the re-heating when the second layer is welded.

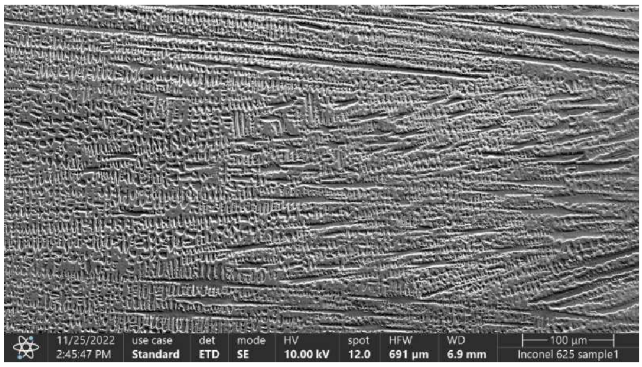

Fig. 58 Dendritic structure of Inconel 625

The transition between the layers of Inconel 625 coating layers clearly shows the change in dimensions of the individual structures. This transition is shown in figure 59. The difference in the shape of the structure is due to the welding process of the protective layer. During the welding process, the material is melted and welded onto the underlying weld. The thermal effect on the bottom layer results in recrystallisation of the bottom layer and slower cooling. Thus, the bottom layer is not as stretched as the top layer, which is on the left in the figure. The upper layer is stretched because of the rapid heat dissipation from the weld site and the individual grains are stretched in the direction of the heat dissipation gradient.

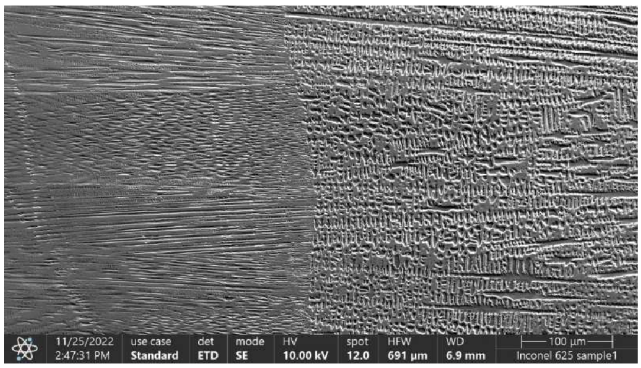

Fig. 59 Boundary between each layer of Inconel 625

The top coating layer has more elongated grains for fast heat dissipation. The structure of the top layer is shown in figure 60. The dendritic structure is less elongated directly at the boundary between the layers and there is more elongation of the individual grains as the distance from the boundary increases. The scratches that were made during sample preparation are visible in the figure below.

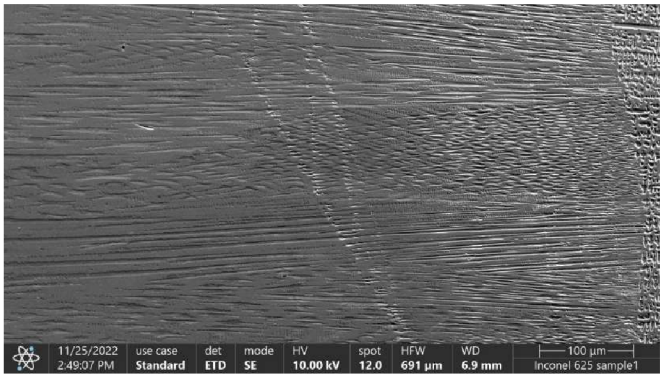

Fig. 60 Second layer of Inconel 625

The evaluation of the structure of the base material 16Mo3 was carried out in the same way as for the coating layer. The material was examined under an Apreo 2 electron microscope. The individual structures of the samples differed from each other only in the size of the thermally affected region, but structurally they are identical. The complete structure was observed from the boundary with the Inconel 625 filler layer to the base material 16Mo3, which was not thermally affected.

Figure 61 shows the structure located at the boundary with the Inconel 625 overlay. The figure shows the mixed structure. The mixed structure is formed during rapid cooling after welding. The rapid heat dissipation from the welding site causes a structural change in the material where there is a non-homogeneous heat dissipation from the structure, hence the formation of the mixed structure. The mixed structure consists of martensite, bainite, residual austenite, ferrite, and pearlite. The structure is very heterogeneous and hard.

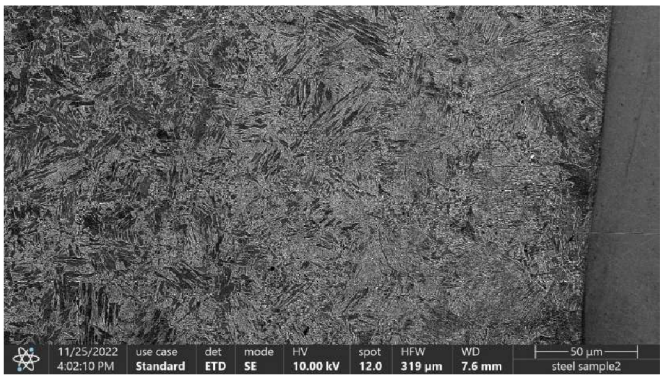

Fig. 61 Boundary between base material 16Mo3 and welded layer Inconel 625

Martensite forms when austenite cools rapidly below the martensite finish temperature. On cooling, austenite does not have enough time to transform to other phases, such as ferrite or pearlite, and transformation to martensite occurs. Martensite has a needle or rod microstructure. The needles or rods are formed by atomic planes and have a specific shape. This microstructure gives martensite its hardness and strength but limits its ductility and toughness. Martensite is known for its high hardness and strength. It also has low toughness and is brittle, which means it tends to fracture instead of deforming under stress.

Bainite forms when austenite cools moderately rapidly below the martensite start temperature It is the result of a diffusion transformation in which carbon atoms and other alloying elements diffuse. This transformation is slower than the transformation of austenite to martensite. Bainite has a fibrous microstructure, which consists of needle or plate crystals. These crystals are composed of ferrite (α-iron) and cementite (carbides). The fibrous structure of bainite contributes to its strength and ductility properties. Bainite provides a balanced combination of strength and ductility. It has higher strength than ferrite but is less brittle than martensite. Bainite also has a higher ductility than martensite, which means that it can exhibit a certain amount of deformation before fracture. There are two main types of bainite - upper bainite and lower bainite. Upper bainite forms at higher temperatures and has a finer fibrous structure. Lower bainite forms at lower temperatures and has a coarser fibrous structure. The two types of bainite have different microstructural properties and mechanical properties.

Residual austenite is formed when austenite, the iron phase, cools rapidly at high temperatures, below the martensite finish temperature. As a result, some of the austenite does not have enough time to fully transform and remains present in the microstructure as a residual phase. Residual austenite is a metastable phase, which means that it tends to transform into other phases such as martensite or bainite with time. This transformation can be caused by heat treatment, cyclic stresses, or temperature rise. This structure has a typical austenite structure that is stable at higher temperatures. It is a face centered cube structure in which the atomic planes are arranged in a regular pattern. Residual austenite can be converted to martensite or bainite by further heat treatment or cyclic stressing. This transformation can lead to a change in the mechanical properties of the material, such as an increase in hardness and strength. Residual austenite can be stabilized by a process called austenite stabilization. Stabilization involves the addition of alloying elements, such as nickel, to the steel. These alloying elements can help reduce the transformation of residual austenite and stabilize it at lower temperatures. The detail of microstructure of mixed structure has been shown in figure 62.

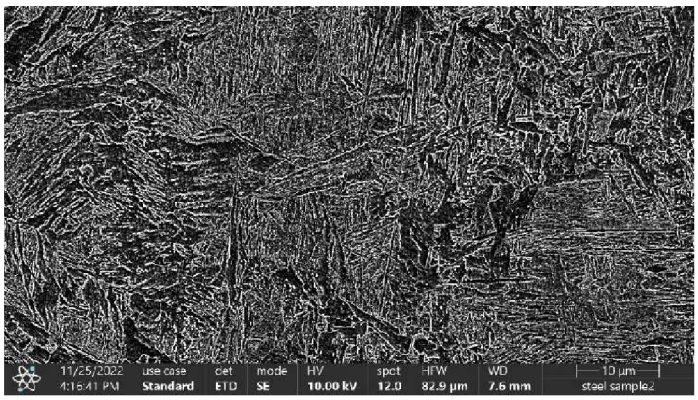

Fig. 62 Detail of mixed structure

The mixed structure is also found further away from the boundary between the materials. At this point, the heat dissipation from the site is slower, thus changing the structural composition of the mixed structure. In figure 63, the darker areas can be seen which are grains of perlite and the lighter areas which are grains of ferrite. Further, the structure contains martensite, bainite and residual austenite. Details of each part of the heat affected zone and the base material are shown in the attachment 7.

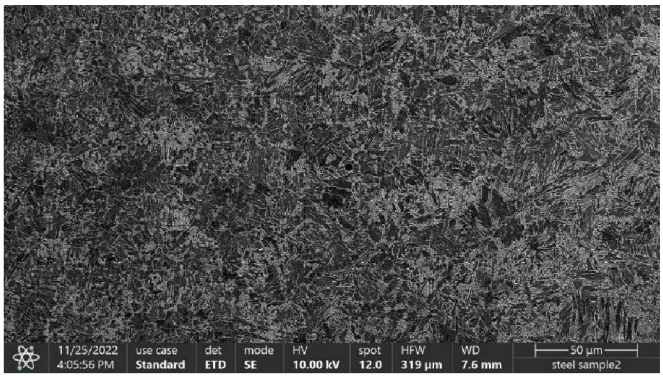

Fig. 63 HAZ of base material 16Mo3

Figure 64 again shows a mixed structure. The difference can be seen in the shape of the structure. It is not as needle-shaped as in the previous case, but the ratio of phases in the mixed structure is different due to the slower cooling. A greater amount of pearlite and ferrite can be seen, on the other hand, with lesser amounts of bainite and martensite.

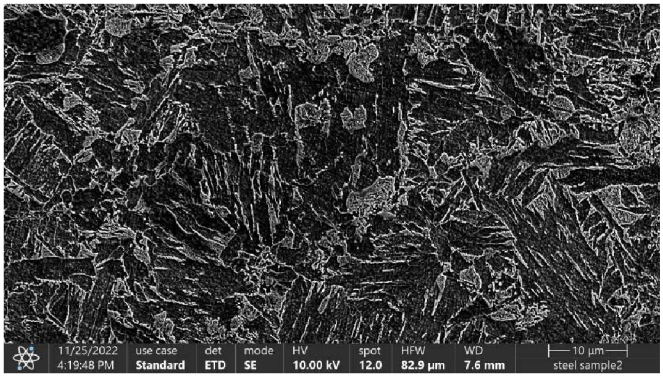

Fig. 64 Detail of HAZ structure

The mixed structure with increasing distance gradually forms into the structure of the base material 16Mo3. The transition region is shown in figure 65. Here the gradual formation of the ferritic-pearlitic structure can be seen. The structure is composed of ferrite and pearlite, then a residual mixed structure containing martensite and bainite with residual austenite. On the right side of the figure, it has been shown the normalization structure. On the left side of the figure, the gradual disintegration of pearlite into ferrite and cementite is visible.

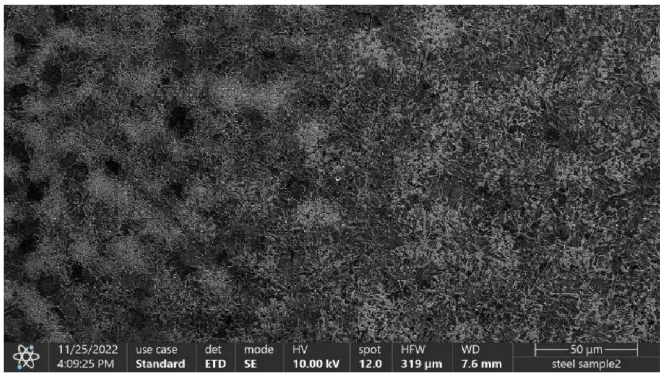

Fig. 65 Normalization and gradual disintegration of pearlite in base material of 16Mo3

The material cools more slowly as the distance from the boundary of the coating increases. Figure 66 and shows a detail of the normalization structure and disintegration of perlite. Compared to the previous structures, there is a slow enough cooling to allow normalization and disintegration of the perlite to take place. Thus, the structure is mainly composed of perlite and ferrite.

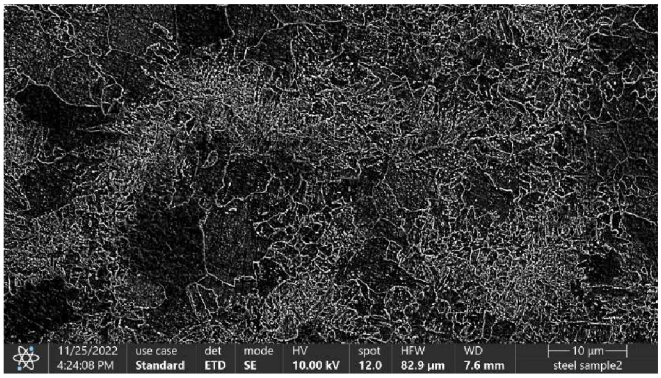

Fig. 66 Detail of normalization structure

The basic structure of the 16Mo3 material is a ferritic-perlitic structure, which is shown in figure 67. This structure is characterized by its lighter areas that are ferrite grains and darker areas that are perlite grains. In the figure the grains are forming from a flake-like shape into the original grains. The size also differs, with the grains in the heat-affected area being larger because of the slow heat dissipation from the material causing the grains to grow. Black lines are visible in the photographs, which are caused by the preparation of the samples during grinding.

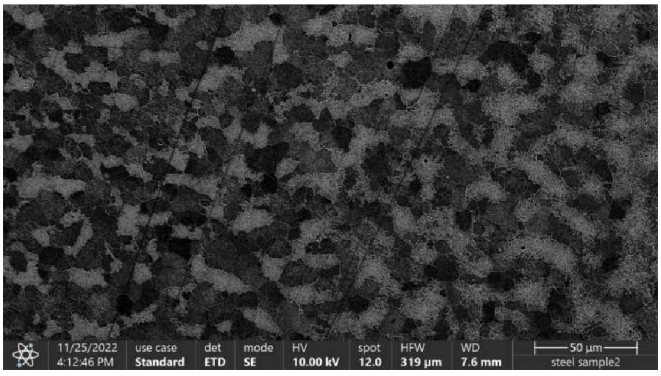

Fig. 67 Structure of base material 16Mo3

The last figure 68 is a detail of the ferritic-pearlitic structure. This structure is basic in this material and is not affected by heat. Ferrite is a phase that consists of a cubic crystal structure and contains a small amount of carbon. Ferrite is soft and ductile, which means that it deforms easily and is resistant to fracture. In 16Mo3 steel, ferrite is present as a matrix that surrounds the pearlitic regions. Perlite is a composite microstructure that consists of layers of ferrite and cementite. Cementite is an iron carbide that is hard and brittle. The layers of ferrite and cementite alternate and form a characteristic lamellar pattern. Perlite is relatively hard and strong, but also has a good ductility. In the microstructure of 16Mo3 steel, perlite is present as dispersed particles surrounded by ferrite. The ferrite-perlite structure is a combination of these two phases and provides a balanced combination of strength, hardness, and ductility. The ferritic matrix provides ductility and fracture resistance, while strength and hardness are provided by the perlite regions.

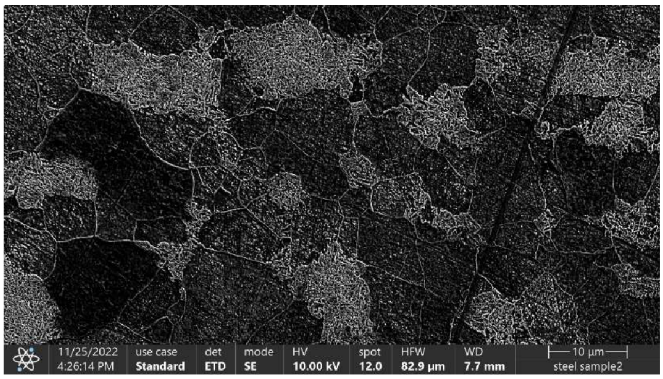

Fig. 68 Detail of ferite-perlite structure

The first defects that was investigated was the crack recorded in the macrostructure image. This defect was recorded on a sample I The crack is located at the boundary between the base material and the coating layer. The crack is shown in figure 69. A detail of the crack is shown in figure 70.

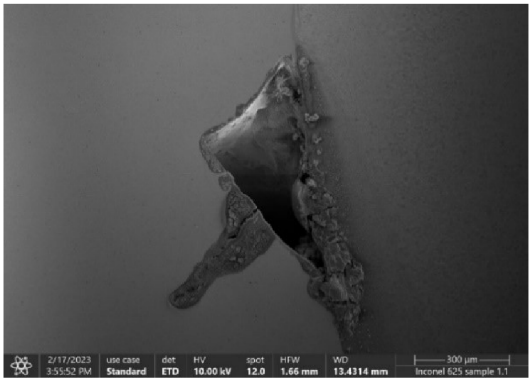

Fig. 69 Crack between materials

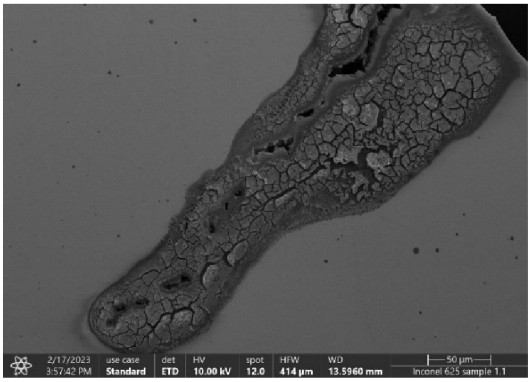

Fig. 70 Detail of crack in specimen I

Detailed view of the fracture boundary is shown in the figure 71. Here you can clearly see the cracks and the boundaries from where thins can potentially spread. The next defect that was investigated is a bubble in the welding overlay. In figure 72 is shown the detail of the bubble. It can be seen that there are boundaries and potential crack propagation points from the bubble boundary. This can reduce the life of the membrane wall. If bubbles are found in the material during welding, measures must be taken to minimise their occurrence. This may include, for example, better control of the welding process, additional pre-treatment of the material or the use of appropriate welding techniques and protective atmospheres.

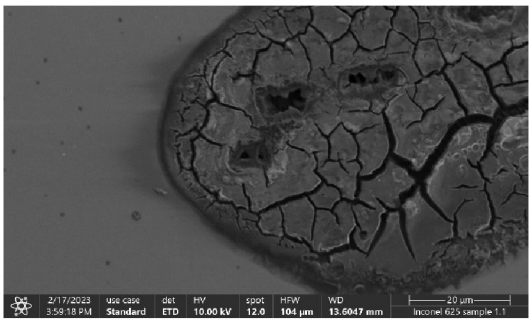

Fig. 71 Detail of the boundary of crack

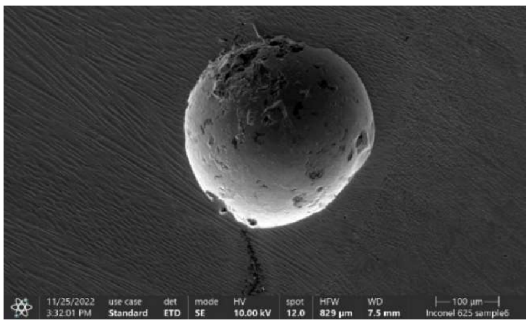

Fig. 72 Detail of bubble

The last defects that were investigated was located between each layer of the Inconel 625 coating in the sample II. The crack formed between the layers is shown in figure 73 and a detail of the crack is shown in figure 74. The crack is located at the boundary between the two layers of Inconel 625. The boundaries of the crack show the boundaries of the individual dendritic structures that were formed during cooling. The dendritic structure that has undergone reheating can be clearly seen on the right side and the elongated grains formed by rapid heat dissipation on the left side. The crack has sharp corners through which the crack could expand.

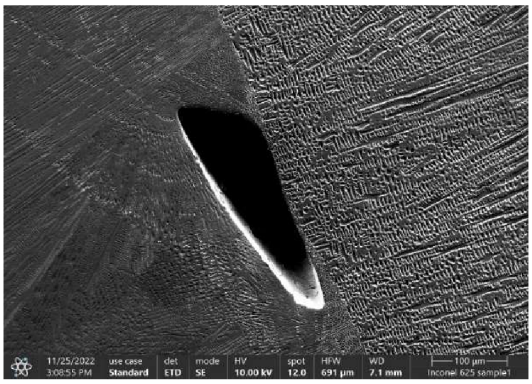

Fig. 73 Crack between each layer of Inconel 625

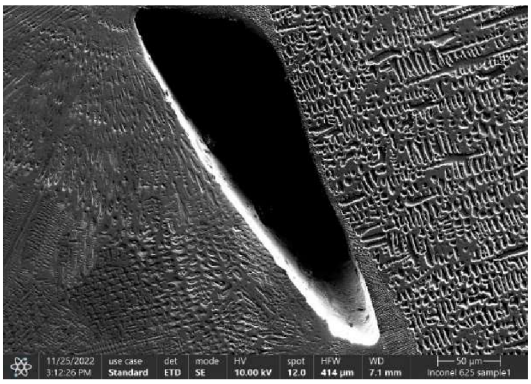

Fig. 74 Detail of crack

3.7 Analysis of microhardness test

In general, the hardness of a material is characterized as the resistance of the surface to local damage due to the action of a foreign body. The individual hardness tests are characterized by the shape and size of the intruding body, the magnitude of the loading force and the method of evaluation. The Vickers test is one of the most accurate hardness tests. The test is described in EN ISO 6507-1. The exact description of the test is described in the table 15. [66; 67; 68]

Table 15 Description of the evaluation of the test [68]

630 HV 30/20	
630	Vickers hardness value
HV	Hardness mark
30	Approximate value of the equivalent test load used in kgf (30 kgf=294,2 N)
20	Test load time 20 s (in the case of steel it is described if it does not lie in the range of 10 to 15 s)

The test is most often performed at a temperature of 10 to 35 ºC. In this method, an indenter in the shape of a regular quadrilateral needle with a square base and an apex angle of 136º is used. The resulting values are the lengths of the individual diagonals of the indentation in the material. The standard EN ISO 6507-1 is only characterized for diagonal lengths in the range 0,02 to 1,4 mm. The method of measuring microhardness described below is used for smaller indentations. Table 16 describes typical test conditions. After the applied load is relieved, the lengths of the diagonals of the body impression are evaluated. The mean diagonal length is then evaluated using the equation 3.4. To correctly evaluate the individual diagonals, the diagonals must occupy 25 to 75 % of the microscope field of view. The resulting material hardness are then determined using the attached tables. Figure 75 shows the scheme of the Vickers test [66]

Table 16 Test conditions for Vickers hardness test [66]

Hardness test		Low load hardness test	
Hardness mark	Nominal value of the test load F $[N]$	Hardness mark	Nominal value of the test load F $[N]$
HV 5	49,03	HV 0,2	1,961
HV 10	98,07	HV 0,5	4,903
HV 50	490,3	HV 1	9,807
HV 100	980,7	HV 3	29,42

Equation 5 Average length:

$$L_a = \frac{L_1 + L_2}{2} \tag{3.4}$$

where: L_a – average length [mm]
L_1 – length of the first diagonal [mm]
L_2 – length of the second diagonal [mm]

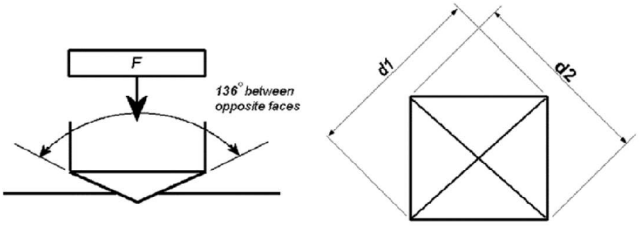

Fig. 75 Scheme of Vickers test [68]

The material must be polished, smooth, flat, and free from any oil or grease. The preparation itself must not thermally or plastically affect the surface of the material, which would cause distortion of the resulting hardness value. The test material shall have a thickness of at least 1,5 times the mean diagonal length of the impression. There shall be no deformation on the reverse side after the test. For testing materials such as lead or tin, a spacing of 6 times the average length of the diagonal of the impression is required. The center of the impression must be at least 2,5 times the average diagonal length of the impression from the edge of specimen. [68]

The Vickers micro-hardness test differs from the Vickers macro-hardness test in the magnitude of the applied load and in the higher accuracy of the evaluation, since the indentations in micro-hardness are orders of magnitude smaller than in macro-hardness. In the Vickers microhardness test, the hardness of the individual structural components of the material can be measured. Since orders of magnitude lower loading values are used, proper specimen preparation is required, like the microscope for microstructure monitoring. The individual parameters of the microhardness test are described in the table 17. [68]

Table 17 Parameters of Vickers micro-hardness test [68]

Micro-hardness test	
Hardness mark	Nominal value of the test load F $[N]$
HV 0,001	0,009807
HV 0,005	0,04903
HV 0,01	0,09807
HV 0,05	0,4903
HV 0,1	0,9807

3.7.1 Results of microhardness test

The sample preparation procedure for microhardness evaluation is identical to the sample preparation discussed in Section 3.2, except for the use of acids to etch the structure of the individual materials. The samples chosen for the macrostructure and microstructure assessment were the same samples from the tops of the semi-circular membrane walls. The individual measurement parameters are described in the table 18.

Table 18 parameters of microhardness test

Method	Load weight	Distance	Load time
Vickerse	100 g	180 µm	10 s

Vickers hardness values were obtained using the AMH55 from LECO. This is an automated device for measuring both hardness at low loads as well as microhardness. It is most used for the analysis of powder surface metals, evaluating hardness in weldments, determining the thickness of surface layers, e.g. For the determination of the surface finish after cementation, nitriding, hardening, boriding or for the determination of the decarburization of a component. This equipment operates in fully automatic mode, where pixel calibration, correction shading, alignment, focusing on the surface to be measured and then measuring the hardness. More information about LECO AMH55 is described in attachment 8.

The first sample that was evaluated on LECO AMH55 was sample I. The evaluation of microhardness will be carried out depending on the information obtained from previous measurements of chemical composition and evaluation of macrostructure and microstructure. The sample contains an average iron dilution of 2,76 wt% in the coating layer. The microhardness map that was produced on the sample I is shown in figure 76.

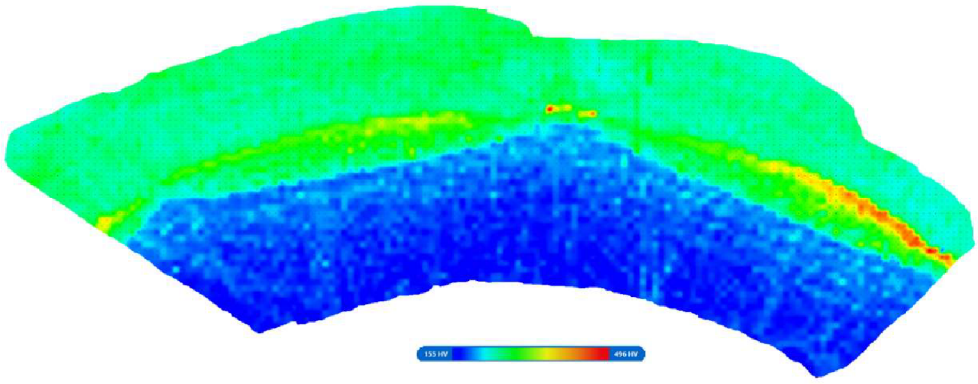

Fig. 76 Microhardness map of specimen with 2,76 wt%

A maximum hardness of 496 HV was found in the alluvial layer. This value was found in the first layer of the weld material, specifically at the boundary between the layers of the weld material. The increased value of microhardness is due to the internal stress in the material caused due to the heat introduction into the material and the subsequent drainage, which in result caused the internal stress that was measured as microhardness According to the microhardness map, compared to the previous sample, there are noticeably fewer areas with such high hardness. This is due to the different welding parameters. The average size of the microhardness in the welded layer is 198,4 HV.

In the Base Material, a minimum hardness of 155 HV was measured, which, as in the previous case, corresponds to the interval according to the material sheet of 16Mo3. The size of the thermally welded area does not differ much from sample to sample, but it is noticeable that the sample I contain a smaller area of material with a higher microhardness value. The highest microhardness value in the base material reaches 254 HV, which is due to the welding process that created a mixed structure at the boundary between the layers of materials, which, as in the previous case, is formed by martensite and bainite, which increases the overall hardness of the mixed structure.

The second sample that was evaluated on the LECO AMH55 instrument was a sample II. The evaluation of microhardness was carried out depending on the information obtained from the chapters on the chemical composition of the Inconel 625 coating and the analysis of the macrostructure and microstructure. The first sample II was tested. This sample achieves an average iron dilution in the structure of 4,79 wt%. The microhardness map of the sample is shown in figure 77.

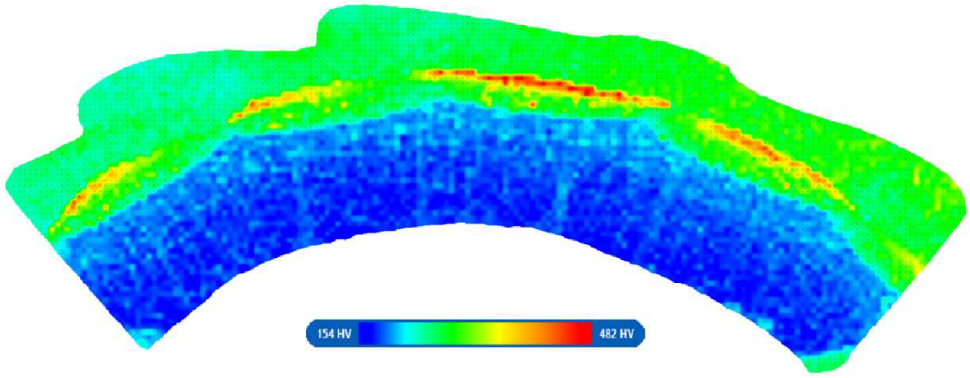

Fig. 77 Microhardness map of specimen with 4,79 wt%

A maximum microhardness of 482 HV was achieved in the coating layer. This hardness is achieved in the first layer of the Inconel 625 coating, specifically at the boundary between the first and second layers of the coating. In figure 71 the increased microhardness is located where the MIG-CMT arc was passed. Although this method guarantees a small thermally affected area, it cannot be dispensed with. The increased micro-hardness is caused by the stress in the material that is created by the heat just delivered, which creates mechanical stress in the material. The average hardness in the coating layer is 346 HV. This value is influenced by the higher iron content in the coating layer of the material and the heat supplied to the transition layer between the different layers of the material. The individual structures of the coating layer were observed under SEM microscope, but structurally these harder regions do not differ from the others.

In the base material, the minimum hardness measured was 154 HV. This hardness corresponds to the Vickers hardness interval according to the material data sheet. The hardness gradient increases towards the boundary between the materials, where the highest value is 226 HV. The magnitude of the maximum microhardness was due to the thermal welding of the base material during the welding of the first layer of Inconel 625. In this region there is a mixed structure that contains hard phases such as martensite and bainite, which form the main component of this part and increase the hardness in this region.

3.8 Analysis of tensile test

The principle of this test is to break the test specimen using uniaxial tension, primarily at an ambient temperature of 10 °C to 35 °C, to obtain the basic stress and strain characteristics of the test specimen such as: ultimate strength, yield strength, ductility, and contraction of the specimen material. Using specific evaluation procedures, the modulus can also be determined tensile elasticity or proportionality limit. In rare cases, the test may be performed at reduced or elevated temperatures. Due to structural or chemical inhomogeneity, the influence the results of this test, therefore care must be taken to ensure the correct location and method of sampling of the sample. The sample should be chosen so that it adequately characterizes the material as a whole and to include the properties of the areas that are most important from a structural or technological point of viewpoint of view. It is also necessary to ensure that the sampling does not affect the subsequent the properties to be tested. To comply with these requirements, it is often necessary to use a larger number of samples. For most tests, the shapes, dimensions, and processing of the specimen are prescribed by the standard. In most cases, the specimens are circular, square, or rectangular cross-section. At the ends of the specimens there are called heads, which are often larger in cross-section than because they are used to clamp the jaws of the testing machine. This difference ensures that the fracture of the test specimen occurs in the measured part of the bar, designated $\mathbf{L_0}$. Examples of cross-sections and shapes of test specimens are available in figure 78 below, showing the type of specimen which has been used in test. Dimensions of specimen before the test (cross-section and measured length marked $\mathbf{L_0}$ and $\mathbf{S_0}$) and after the test (cross-section and measured length marked $\mathbf{L_U}$ and $\mathbf{S_U}$). [67; 69]

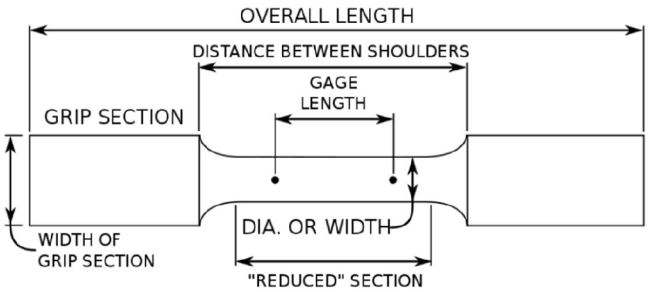

Fig. 78 Type of tensile tests specimen [69]

Using the initial measured length $\mathbf{L_0}$, the test samples can be divided into proportional or non-proportional test bar. For a proportional test bar, $\mathbf{L_0}$ refers to the original cross-section of the test bar $\mathbf{S_0}$ and can be calculated using the equation 3.5. The coefficient of proportionality shall preferably take the value of 5,65. This is the case when observing the condition where $\mathbf{L_0}$ is at least 20 mm. The calculated $\mathbf{L_0}$ should then be rounded to the nearest to the nearest multiple of 5 mm. If this condition is violated, then $\mathbf{L_0}$ will be less than 20 mm, a proportionality factor of 11,3 or a non-proportional test bar must be used. [67; 69]

Equation 6 Initial measured length:

$$L_0 = k \cdot \sqrt{S_0} \tag{3.5}$$

where: L_0 – initial measured length [mm]
k – coefficient of proportionality [-]
S_0 – initial cross-seciton of the bar to be tested [mm]

In the case of non-proportional test bars, the length L_0 is not related to S_0 and these bars are manufactured preferably in lengths **L** = 50, 80, 100 or 200 mm and widths of 12,5, 20, 25 or 40 mm. For specimens made of strip, sheet, or flat products in thicknesses from 0,1 to 3 mm, the following are preferred. For wires, rods, or profiles up to 4 mm thick or diameter, L_0 is selected as 100 or 200 mm. The whole product is usually tested, so the test bar has an unmachined surface. In the case of strips, sheets, or flat products over 3 mm thick and wires, rods, profiles with a thickness or diameter of more than 4 mm, widths of 20, 25 and 40 mm and lengths of L_0 80 and 200 mm are used. [67; 69]

3.8.1 Tensile test procedure

Figure 79 shows a diagram with a significant yield strength. This diagram is typical of annealed, unrelieved steel. Figure 80 shows a diagram with an insignificant yield strength, which is typical for annealed quenched and tempered steel. Both diagrams are divided into four phases. [67]

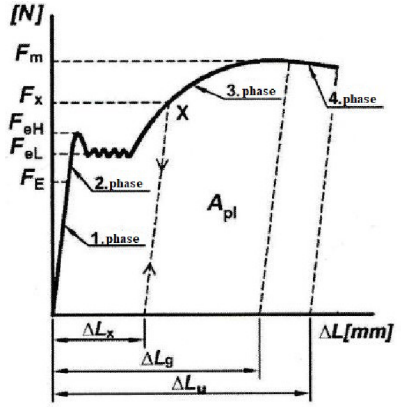

Fig. 79 Diagram with significant yield strength [69]

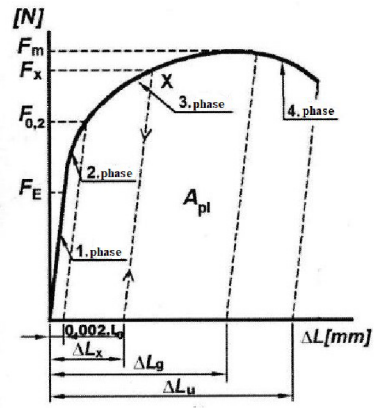

Fig. 80 Diagram with insignificant yield strength [69]

In the first phase is a region of elastic deformation where the tested bar elongates in direct proportion to the increasing applied force. This deformation, which is elastic only, is shown in the diagram as a straight line. This means that when the applied force is removed, the test bar shortens to its original length. value. The first phase ends at the so-called limit of proportionality, which is denoted by R_e. In most cases, practical measurements in the laboratory do not determine because of the difficulty of finding the point where elastic deformation becomes plastic. [67; 69]

The second phase is located between the proportionality limit and the so-called yield stress, marked depending on the type of diagram, as R_e or $R_{p0.2}$. The deformation in this phase is only plastic and occurs there is a difference between a diagram with a significant yield stress and one with an insignificant yield stress. The elongation of the tested bar no longer grows linearly with increasing loading force. As can be seen in figure 73, when the so-called yield strength, denoted as R_e, is reached (in figure 73, the force at the yield strength F_E), the elongation continues without further increase in the loading force and thus a lag occurs. If this delay is in a larger section, the force on the upper yield strength can also be discerned in figure 73 F_{eH} and the force at the lower yield point F_{eL}. In figure 74, the case where the nonlinear deformation transitions smoothly from the second phase can be seen to the third phase, which is the so-called inelastic yield stress. In this type of diagram, the second phase is terminated by a contracted yield stress, denoted as $R_{p0.2}$ (in figure 74 denoted by the contracted yield stress $F_{p0.2}$). This strain is commonly given as 0,2 % of L_0 and is therefore equal to 0,002-L_0. [67; 69]

In the third phase, homogeneous (uniform) plastic deformation occurs. The area of this of deformation begins above the yield stress and ends at the strength limit, denoted as **R_m** (denoted in figure 73 as the force at the interface **F_m**). This phase is characterized by uniform permanent deformation of the test bar over the entire length measured up to the point where the loading stress reaches the ultimate strength (**R_m**) and a constriction, called a neck, is formed. Thereafter, there is no longer a uniform deformation (end of the third phase), but only the area where the constriction occurs is deformed. [67; 69]

Phase four starts at the intermediate strength **R_m** and ends with the breaking of the tested bar. In this last area, the test bar is no longer extended along the entire measured length, but only in the neck area up to the breaking point. After breaking the two parts can be brought together again and the maximum size of the permanent elongation of the test bar **ΔL_u** according to the equation 3.6. [67; 69]

Equation 7 Total elongation of the tested bar

$$\Delta L_u = L_u - L_o \tag{3.6}$$

where: ΔL_u – total elongation of the tested bar [mm]
L_u – final measured length after breaking [mm]
L_0 – initial measured length [mm]

3.8.2 Basic evaluated parameters

If the yield strength is exceeded, only plastic deformation of the bar. The bar under test is further elongated without increasing the load force. As mentioned above, in the second phase, it is possible to distinguish materials with a significant yield strength yield strength (**R_e**) and with a non-significant yield strength (**$R_{p0.2}$**). The yield strength can be expressed by the ratio of the loading of the yield stress to the original cross-section of the tested bar. Equations has been described below. [67; 69]

Equation 8 Tensile yield strength:

$$R_e = \frac{F_e}{S_0} \tag{3.7}$$

where: R_e – significant yield strength [MPa]
F_e – load force [N]
S_0 – initial cross-section [mm^2]

Equation 9 Tensile yield strength:

$$R_{p0.2} = \frac{F_{p0.2}}{S_0} \tag{3.8}$$

where: $R_{p0.2}$ – insignificant yield strength [MPa]
$F_{p0.2}$ – load force [N]

Tensile strength **Rm** is a contractual value which can be expressed by equation (3.9). It is the proportion of the maximum measured loading force during the test and the initial cross-section of the bar to be tested. [67; 69]

Equation 10 Tensile strength:

$$R_m = \frac{F_m}{S_0} \tag{3.9}$$

where: R_m – tensile strength [MPa]
F_m – maximum load force [N]

Ductility **A** refers to the relative elongation of the bar under test, expressed as a percentage of the original measured length. The relative elongation can be calculated according to equation (3.10). [67; 69]

Equation 11 Ductility:

$$A = \frac{L_u - L_0}{L_0} \cdot 100 \tag{3.10}$$

where: A – ductility [%]

Contraction **Z** indicates the percentage ratio of the difference between the original and final cross-sectional area (after breaking) to the original cross-section of the bar under test. This ratio is shown in equation (3.11). [67; 69]

Equation 12 Contraction:

$$Z = \frac{S_0 - S_u}{S_0} \cdot 100 \tag{3.11}$$

where: Z – contraction [%]
S_u – final cross section [mm^2]
S_0 – initial cross section [mm^2]

3.8.3 Results of tensile test

In tensile testing, the yield strength and ultimate strength of 16Mo3 base material samples and Inconel 625 coated 16Mo3 base material samples were evaluated. Three specimens are with Inconel 625 overlay with iron dilution of 2,76 wt% as determined by chemical analysis and 16Mo3 base material. The other three samples are 16Mo3 base material only. The samples were prepared on a plasma cutter. Since the values to be determined are yield strength, ultimate strength and maximum loading force and ductility is not required, the specimens are notched to better indicate the crack at a specific location on the specimens.

ZD40 hydraulic testing machine was used as the testing equipment. The test rig is multifunctional as it can perform tensile, compression and bending tests up to 400 kN. It is equipped with an EDC 60 control unit. The machine parameters are further described in attachment 9.

The first material tested was the base material 16Mo3. Three samples were tested. The values found were yield strength, tensile strength, and maximum load force. The values obtained were entered in Table 19.

Table 19 Parameters of 16Mo3 steel

Parameter	Unit	2.1	2.2	2.3	average value
Tensile strength R_m	[MPa]	526	524	526	525
Tensile yield strength $R_{p0,2}$	[MPa]	405	397	414	405
Maximum load force F_m	[N]	47316	45886,4	44964,8	46055,7

The average values that have been calculated from the values found in the work are compared with the values from the material sheet in attachment. 1.The yield strength and the ultimate strength are within the range given in the bill of materials. The progress of the individual measurements is included in the chart 2. The vertical axis shows the stress calculated from the maximum loading force divided by the original area of specimen.

Chart 2 Tensile test graph of samples of 16Mo3

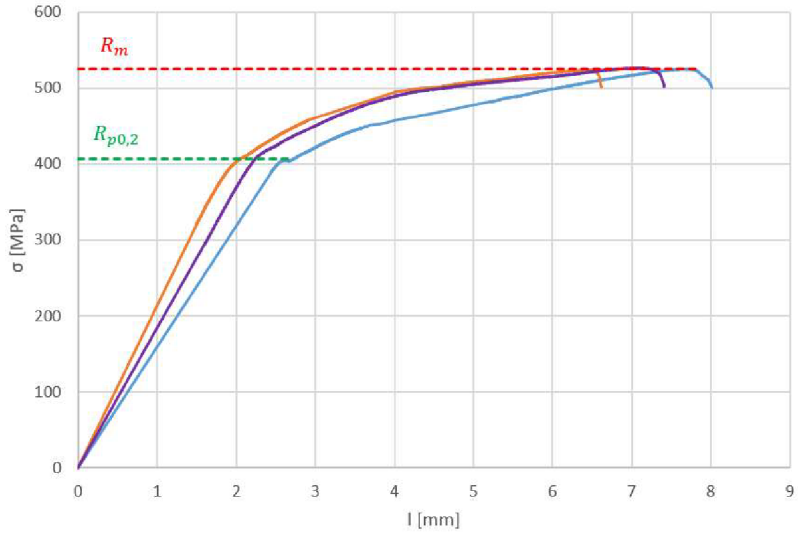

In the second case, samples with a coating of Inconel 625 were tested. Three samples were tested as in the previous case. The obtained values of yield strength, tensile strength and maximum load force were recorded in Table 20.

Table 20 Parameters of specimens with welded layer

Parameter	Unit	1.1	1.2	1.3	average value
Tensile strength R_m	[MPa]	684	622	655	654
Tensile yield strength $R_{p0,2}$	[MPa]	532	461	498	497
Maximum load force F_m	[N]	50842,8	67875,2	82320,8	67012,9

In this case, a plot of the individual voltage dependence on elongation was again created and entered the chart 3. The average values of yield strength and ultimate strength were also plotted. As in the previous case, the stress is recorded on the vertical axis and is calculated as the maximum loading force divided by the half surface area of the specimen. Each chart of tensile test is shown in the attachment 10.

Chart 3 Tensile test graph of samples with welded layer

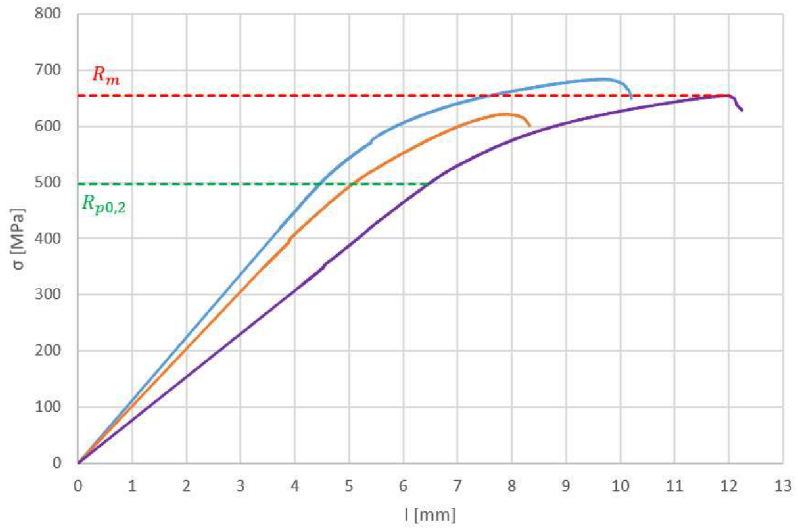

4 CONCLUSION

The focus of the research part of the thesis was the analysis of designs created using welding parameters in the form of synergies recommended by the supplier of welding resources. The results obtained from the analysis of the chemical composition served to verify the correctness of the use of each welding parameter. The average value of the dilution of the weld layer with iron reached values of 2,76 % and 4,79% for the individual samples. For practical use, the lower the iron content in the structure, the higher the lifetime of the coating layer.

The analysis of the macrostructure served to determine whether the parameters used produce a surfacing of sufficient quality and to determine the amount, size of defects and to identify areas for the evaluation of the material microstructure. The macrostructural defects were in the form of pores that were formed during the welding process. A reduction in the number of defects could be guaranteed by changing some welding parameters. The resulting size of the thermally affected area did not differ much from each other, reaching an average value of 1,38 % and 1,37 % for the samples.

The microstructure was mainly evaluated to see how the material behaves during the two-layer welding process. An important piece of information was the shape of the dendritic structure when thermally affected during the welding process. The mixed structure was observed in the base material and the transition to the base material, which was without thermal influence, where the ferritic-perlitic structure was found. The defects were also monitored to determine in what form they are found and whether they influence reducing the life of the coating. The information obtained from the analysis of the chemical composition and microstructure of the material was used in the microhardness test.

Microhardness maps were produced, and it was found that the specimen with higher iron content in the structure and therefore using different parameters achieved higher internal stresses, which was found to be higher at the boundary between the layers of Inconel 625. The highest value of microhardness of sample I was in the coated layer 496 HV, and in the base material 254 HV. The average value was 198,4 HV and minimum value in base material was 155 HV. In the sample II was the highest value of microhardness in coated layer 482 HV and in base material 226 HV. The average value was 346 HV and average value was 226. The differences are small, but the residual stress is different due to welding process parameters.

Tensile testing was chosen as the last test. Here the task was to determine the magnitude of the yield strength and ultimate strength of the base material and the combination of the base material and the superstrate. Tensile diagrams were produced, from which it was immediately apparent that the specimens with a coating layer achieved higher values. For the base material 16Mo3, the yield strength and ultimate strength averaged 405 MPa and 525 MPa respectively. For the Inconel 625 coated samples, the yield strength and ultimate strength values were 497 MPa and 654 MPa respectively.

5 BIBLIOGRAFIE

1. *Spalovny odpadu – odpad jako palivo* [online]. 2014 [cit. 2022-07-17]. Dostupné z: https://energetika.tzb-info.cz/nakladani-s-odpady/11897-spalovny-odpadu-odpad-jako-palivo
2. *Radermacher Walter: Environmental statistics and accounts in Europe* [online]. 2014 [cit. 2022-07-16]. Dostupné z: http://epp.eurostat.ec.europa.eu/cache/ITY_OFFPUB/KS-32-10-283/EN/KS-32-10-283-EN.PDF
3. *DEPARTMENT OF THE ARMY: Central Boiler Plants* [online]. Headquarters, 354 s. [cit. 2023-05-14]. Dostupné z: https://www.wbdg.org/FFC/ARMYCOE/COETM/tm_5_650.pdf
4. DLOUHÝ, T. *Stavba kotlů: Přednáška č.12*. Praha, 2019. Dostupné také z: http://energetika.cvut.cz/wp-content/uploads/StK-p12.pdf
5. NOVÁK, P. ÚSTAV KOVOVÝCH MATERIÁLŮ A KORZNÍHO INŽENÝRSTVÍ VŠCHT PRAHA. *Druhy koroze kovů* [online]. 2005 [cit. 2022-07-17]. Dostupné z: http://www.kmt.tul.cz/edu/podklady_kmt_magistri/KPU/koroze%20druhy%20vscht.PDF
6. KASTNER, W., M. ERWE, N. HENZEL a B. STELLWAG. SIEMENS. *Erosion corrosion in power plant piping systems* [online]. Erlangen, Federal Republic of Germany:, 1990 [cit. 2022-07-17]. Dostupné z: https://inis.iaea.org/collection/NCLCollectionStore/_Public/22/038/22038332.pdf
7. *Optimiza: High temeprature corrosion* [online]. 2020 [cit. 2022-07-17]. Dostupné z: https://optimiza.es/en/high-temperature-corrosion/
8. *What is a pitting resistance equivalent number (PREN)?* [online]. 2021 [cit. 2022-07-19]. Dostupné z: https://www.unifiedalloys.com/blog/pitting-resistance-pren/
9. SlANIA, J., R. KRAWCZYK a S. WÓJCIK. *Examination And Detecting Discontinuities In The Austenite Inconel 625 Layer Used On The Sheet Pile Walls Of The Boiler's Evaporator To Utilize Waste Thermally.* [online]. Archives of Metallurgy and Materials, 2015 [cit. 2022-07-19]. doi: 10.1515/amm-2015-0294.
10. DUTRA, J., N. BONACORSO, R. SILVA, R. CARVALHO a F. SILVA. *Development of a flexible robotic welding system for weld overlay cladding of thermoelectrical plants' boiler tube walls.* Mechatronics, 2014. Dostupné z: doi:10.1016/j.mechatronics.2014.03.002
11. SONGYA, T., A. SAIFAN, G. PENGQIAN, I. DAWY a B. SALEH. *Development of an Automatic Welding System for the Boiler Tube Walls Weld Overlay: Metals* [online]. China [cit. 2022-07-19]. Dostupné z: https://www.mdpi.com/2075- 4701/10/9/1241/htm
12. KUBÍČEK, J. *Žárové nástřiky: Přednáška* [online]. In: . Brno [cit. 2022-07-20]. Dostupné z: https://docplayer.cz/104232869-Zarove-nastriky-jaroslav-kubicek-vut-fsi-brno- 2018.html
13. *Plynové dynamické stříkání: Technologie dynamického stříkání studeným plynem* [online]. In: . Rusko [cit. 2022-07-20].
14. JECH, D., P. KOMAROV, M. REMEŠOVÁ a I. ROČŇÁKOVÁ. *Technologie žárových nástřiků: Studený kinetický nástřik: EngineeringSK* [online]. In: . Brno: CEITEC, VUT [cit. 2022-07-20].
15. WEMAN, Klas. *Welding processes handbook*. 2nd ed. Oxford: Woodhead Publishing, 2012. Woodhead Publishing in materials. ISBN 978-0-85709-510-7.
16. AMBROŽ, O., B. KANDUS a J. KUBÍČEK. *Technologie svařování a zařízení: učební texty pro kurzy svářečských inženýrů a technologů*. 1. vyd. Ostrava: ZEROSS, 2001. Svařování. ISBN 80-85771-81-0.
17. KOVAŘÍK, R. a F. ČERNÝ. *Technologie svařování*. 2. vyd. Plzeň: Západočeská univerzita, 2000, 185 s. ISBN 80-7082-697-5.

18. FRONIUS ČESKÁ REPUBLIKA S.R.O. *COLD METAL TRANSFER: Technologie.* [online]. In: . 2. 16s. [cit. 2022-07-20]. Dostupné z: https://www.fronius.com/cs-cz/czechrepublic/perfect-welding/polozky-ke-stazeni
19. MEDUNA, M. a FRONIUS ČESKÁ REPUBLIKA S.R.O. *Inovace svářecích zařízení pro metodu MIG/MAG.* [online]. In: . Jihlava [cit. 2022-07-20]. Dostupné z: https://www.fronius.com/cs-cz/czech-republic/perfect-welding
20. *Technický týdeník: Nový standard ve svařovací technice: Proces CMT (Cold Metal Transfer)* [online]. In: . [cit. 2022-07-20].
21. *CMT -cold metal transfer: Studený svařovací proces pro nejvyšší kvalitu* [online]. Praha [cit. 2022-07-16]. Dostupné z: https://www.fronius.com/cs-cz/czech-republic/perfect-welding/svet-svarovani/fronius-welding-processes/cmt
22. *CMT upgrade for TPS/i robotics power source: Fronius: Perfect Welding* [online]. In: . [cit. 2022-07-20]. Dostupné z: https://www.fronius.com/cs-cz/czech-republic/perfectwelding/informacni-centrum/tisk/cmt-upgrade-060317
23. FREMUNT, Přemysl a Tomáš PODRÁBSKÝ. *Konstrukční oceli*. Brno: Akademické nakladatelství CERM, 1996. ISBN isbn80-858-6795-8.
24. *Konstrukční oceli pro práci za zvýšených teplot: Materiály a technologie* [online]. [cit. 2023-05-13]. Dostupné z: https://www.scritub.com/limba/ceha-slovaca/Konstrukn-ocelipro- prci-za-zv74444.php
25. PANTĚLEJEV, Libor. *Přednášky: Mezní stavy materiálů.* Brno, 2007. Http://ime.fme.vutbr.cz/index.php/cs/studium/podklady-pro-vyuku-zimni-semestr.
26. PURMENSKÝ, Jaroslav, Václav FOLDYNA a Karel MATOCHA. *PERSPEKTIVNÍ ŽÁRUPEVNÉ OCELI A JEJICH VLASTNOSTI A PRAKTICKÉ VYUŽITÍ* [online]. In: . [cit. 2023-05-13]. Dostupné z: https://adoc.pub/perspektivni-arupevne-oceli-ajejich- vlastnosti-a-prakticke-.html
27. BENDICK, W. a I. VON HAGEN. *Creep Resistant Feritic Steels For Power Plants* [online]. In: . [cit. 2023-05-13]. Dostupné z: http://www.cbmm.com.br/portug/sources/techlib/science_techno/table_content/sub_4/im a ges/pdfs/040.pdf.
28. VODÁREK, Vlastimil. *Fyzikální metalurgie modifikovaných (9-12)%Cr ocelí*. Ostrava: Vysoká škola báňská - Technická univerzita Ostrava, 2003. ISBN isbn80-248-0329-1.
29. *P235GH: nelegovaná teplu odolná ocel pro tlakové nádoby a bezešvé trubky*. 2014. Dostupné také z: https://pdms-help.webnode.cz/news/p235gh-tepelne-odolna-ocel-pro-tlakove-nadoby/
30. PENINSULAR STEEL TUBES. *P91_T91* [online]. Spain, 2014 [cit. 2022-07-19]. Dostupné z: http://www.peninsulardevastagos.es/wp-content/uploads/P91-T91.pdf
31. SALZGITTER FLACHSTAHL. *3CRMo4-5: Heat resistant pressure vessel steels* [online]. In: . Salzgitter, Německo, 2019 [cit. 2022-07-19].
32. *16Mo3 Chrome Moly Steel: AZoM.com* [online]. Masteel UK, 2010 [cit. 2023-04-03]. Dostupné z: https://www.azom.com/article.aspx?ArticleID=5244
33. *Nová ocel z Ostravy se uplatní zejména v energetice: TechMagazín* [online]. Praha: TECH MEDIA PUBLISHING s r.o., 2015 [cit. 2023-04-03]. Dostupné z: http://www.techmagazin.cz/2138
34. *Material No.: 1.5415: M.Woite Sonderwerkstoffe Edelstähle* [online]. 2012 [cit. 2023-04-03]. Dostupné z: http://www.woite-edelstahl.com/15415en.html#

35. PILOUS, V. a V. KUDĚLKA. *Nikl a slitiny niklu - superslitiny niklu* [online]. In: . Brno: TESYDO, s.r.o, 2017, 62 s. [cit. 2022-07-19]. ISBN ISBN 978-80-87102-16-9.
36. MACHEK, Václav a Jaromír SODOMKA. *Nauka o materiálu:Kovy a kovové materiály: 1. část*. Praha ČVUT, 2001. ISBN ISBN 80-01-02424-5.
37. MACHEK, Václav a Jaromír SODOMKA. *Nauka o materiálu: Kovy a kovové materiály 1. část.* Praha ČVUT, 2001. ISBN 80-01-02424-5.
38. REED, Roger C. UNIVERSITY OF CAMBRIDGE. *The Superalloys Fundamentals and Applications*. 2. University of Birmingham, 2008, 392 s. ISBN 9780521070119. Dostupné také z: https://www.cambridge.org/cz/academic/subjects/engineering/materials-science/superalloys-fundamentals-and-applications?format=PB&isbn=9780521070119
39. LOSERTOVÁ, M. *Progresivní materiály: učební text* [online]. In: . Vysoká škola báňská: Technická univerzita Ostrava [cit. 2022-07-19].
40. PTÁČEK, Luděk. *Nauka o materiálu II.* 2. opr. a rozš. vyd. Brno: Akademické nakladatelství CERM, 2002. ISBN 80-7204-248-3.
41. SONDEL, M. a ČESKÝ SVÁŘEČSKÝ ÚSTAV S.R.O. *Svařování niklu a jeho slitin* [online]. In: . Ostrava, 2017 [cit. 2022-07-19].
42. HÖFER, M. a BÖHLER SCHWEIßTECHNIK AUSTRIA. *Svařování niklu a slitin na bázi niklu* [online]. In: . [cit. 2022-07-19]. Dostupné z: https://www.kskct.cz/images/katalog/dokumentyostatni/dokumentace/Ni%20slitiny%20BW%20%C4%8Desky.pdf
43. KUNCIPÁL, Josef. *Teorie svařování: celostátní vysokoškolská učebnice pro strojní fakulty vysokých škol technických*. 1. vyd. Praha: Státní nakladatelství technické literatury, 1986. ISBN MK 1622.
44. FOLDYNA, V., K. HENNHOFER a I. HLAVATÝ. *Materiály a jejich svařitelnost: učební texty pro kurzy svářečských inženýrů a technologů*. 2. Ostrava: Zeross, 2001. ISBN 80-85771-85-3.
45. *16Mo3 Heat-resistant pressure-vessel steel: Salzgitter Flachstahl 16Mo3 Seite 1*. Www.salzgitter-flachstahl.de. 2022.
46. *16Mo3 material datasheet* [online]. XICHENG SCIENCE & TECHNOLOGY BUILDING HIGH-TECH DEVELOPMENT ZONE, ZHENGZHOU, CHINA, 2016 [cit. 2023-04-03]. Dostupné z: http://www.bebonchina.com/v3/bebon-show/news/16mo3-material-specification-16mo3-material-datasheet_894.html
47. *SPECIAL METALS CORPORATION. INCONEL®: Alloy 686: Datasheet* [online]. In: . USA: SMC-024, 2000, s. 15 [cit. 2022-07-19].
48. OLA, O.T. a F.E. DOERN. *A study of cold metal transfer clads in nickel-base INCONEL 718 superalloy: Materials & Design*. 2014, 57 s. ISSN 0261-3069. Dostupné také z: https://doi.org/10.1016/j.matdes.2013.12.060
49. *AX-625 AX-2.4831* [online]. AX-625 AX-2.4831 [cit. 2023-05-14]. Dostupné z: https://www.kskct.cz › katalog › dokumentace
50. *Tps-500i: Fronius* [online]. Praha, 2023 [cit. 2023-04-03]. Dostupné z: https://www.fronius.com/cs-cz/czech-republic/perfect-welding/vyrobky/ru%C4%8Dn%C3%AD-sva%C5%99ov%C3%A1n%C3%AD/migmag/tpsi/tpsi/tps-500i
51. SOMMER, Lumír, Viktor KANICKÝ, Vítězslav OTRUBA a Jiří TOMAN. *Optická emisní spektrometrie v indukčně vázaném plazmatu a vysokoteplotních plamenech*. 1. vyd. Praha: Academia, 1992, 151 s. ISBN 80-200-0215-4.

52. *ARL iSpark™ Series Optical Emission Spectrometer: Thermo Scientific™* [online]. 2023 [cit. 2023-03-09]. Dostupné z: https://www.thermofisher.com/order/catalog/product/IQLAAHGABDFAOOMBCM
53. KOMÁREK, Josef. *Atomová absorpční spektrometrie*. 1. vyd. Brno: Masarykova univerzita, 2000, 85 s. ISBN 80-210-2500-X.
54. HILL, Steve J. *Inductively coupled plasma spectrometry and its applications*. 2. ed. Oxford: Blackwell, 2007, xviii, 427 s. : il., tab. ISBN 978-1-4051-3594-8.
55. *Niton™ XL3t XRF Analyzer: Thermo Scientific™* [online]. 2023 [cit. 2023-03-09]. Dostupné z: https://www.thermofisher.com/order/catalog/product/10131166
56. *HS 200: Manual grinding machine* [online]. 2023 [cit. 2023-03-11]. Dostupné z: https://www.herzog-maschinenfabrik.de/en/products/grinding/hs-200-manual-grinding-machine/
57. *LECO Sectioning Products: LECO MSX205 Series Benchtop Sectioning Machines* [online]. 2022 [cit. 2022-11-13]. Dostupné z: https://eu.leco.com/metallography-sectioning
58. *Struers - LaboSystems* [online]. 2022 [cit. 2022-11-13]. Dostupné z: https://www.struers.com/en/Products/Grinding-and-Polishing/Grinding-and-polishing-equipment/LaboSystem
59. *LECO - PX400 / PX500 Series Advanced Grinder / Polisher* [online]. 2022 [cit. 2022-11-13]. Dostupné z: https://eu.leco.com/product/px400-px500-grinder-polisher-series
60. *LECO Supplies for Inorganic Analysis* [online]. 2022 [cit. 2022-11-13]. Dostupné z: https://cz.leco.com/products/consumables
61. *Ultrasonic cleaner Sonic-2* [online]. 2022 [cit. 2022-11-13]. Dostupné z: https://www.polsonic.com/ultrasonic-cleaner-sonic-2.html
62. *Keyence VHX-500: Digital microscope* [online]. 2020 [cit. 2023-05-14]. Dostupné z: https://www.equipx.net › KeyenceVHX500
63. *Scanning Electron Microscopes Apreo 2 SEM* [online]. 2023 [cit. 2023-05-14]. Dostupné z: https://www.thermofisher.com/cz/en/home/electron-microscopy/products/scanning-electron-microscopes/apreo-sem.html
64. REIMER, L. *Scanning Electron Microscopy*. Berlin: Berlin Heidelberg, Springer Series in Optical Sciences, 1998. ISBN 978-3-642-08372-3. Dostupné z: doi:10.1007/978-3-540-38967-5
65. ZWORYKIN, V.K. *The Scanning Electron Microscope.: Scientific American.* 1942. ISSN 0036-8733. Dostupné z: doi:10.1038/scientificamerican0942-111
66. *Zkoušky tvrdosti: Oddělení povrchového inženýrství* [online]. [cit. 2022-11-29]. Dostupné z: https://www.opi.zcu.cz/Zkousky_tvrdosti.pdf
67. MACHEK, Václav. *Kovové materiály 2: Vlastnosti a zkoušení kovových materiálů*. Praha, ČVUT, 2014. ISBN 978-80-01-05527-4.
68. *ČSN EN ISO 6507-1 (420374) A Kovové materiály-Zkouška tvrdosti podle Vickerse.: Část 1, Zkušební metoda.* Praha: Úřad pro technickou normalizaci, metrologii a státní zkušebnictví, 2018.
69. *ČSN EN ISO 6892-1 (420310) A Kovové materiály-Zkoušení tahem. Část 1, Zkušební metoda za pokojové teploty.* Praha: Úřad pro technickou normalizaci, metrologii a státní zkušebnictví, 2017.
70. *ARL iSpark Series - Thermo Fisher Scientific* [online]. 2013 [cit. 2023-05-14]. Dostupné z: https://tools.thermofisher.com › sfs › brochures

71. *AMH55 Hardness Testing System* [online]. 2023 [cit. 2023-05-14]. Dostupné z: https://www.leco.com/product/amh55-hardness-testing-systems

LIST OF SYMBOLS AND ABBREVIATIONS

Symbols

Mark	Legend	Unit
A_5	Ductility	%
A_T	Atomic weight	-
a	Grid constant	mm
E	Tensile modulus	GPa
F	Force	N
F_e	Load force	N
F_m	Maximum force	N
G	Shear modulus	GPa
k	Coefficient of proportionality	-
L_0	Initial measured length	mm
L_1	Length of the first diagonal	mm
L_2	Length of the second diagonal	mm
L_a	Average length	mm
L_u	Final measured length	mm
n	Number of measurements	-
R	Electrical resistance	Ω
Re	Significant yield strength	MPa
Rm	Tensile strength	MPa
$Rp_{0,2}$	Insignificant yield strength	MPa
S_0	Initial cross section of the bar to be tested	mm^2
S_u	Final cross section	mm^2
T	Temperature	$°C$
T_T	Melting point	$°C$
$\bar{x}$	Average value of chemical composition	-
x_i	Value of individual measurements	-
Z	Contraction	%
γ	Material phase gamma	-
δ	Material phase sigma	-
η	Material phase eta	-
σ	Standard deviation	-

LIST OF ATTACHMENTS

Attachement 1 1/1

Chemical composition of steel 16Mo3

SALZGITTER FLACHSTAHL
A Member of the Salzgitter Group

16Mo3

Heat-resistant pressure-vessel steels

Material no.	1.5415
according to	DIN EN 10028-2
Tensile strength class	B

General

These steel grades are characterised by a good weldability. They are used above all for manufacturing boilers, pressure vessels and pipes transporting hot liquids.

The user of these steel grades must make sure that his calculation, design and processing methods are appropriate for the material. The grades of this series offer good cold and hot-forming properties.

Chemical composition[1)2)]

(in percent by weight)

	min. in %	max. in %
C	0.12	0.20
Si		0.35
Mn	0.40	0.90
P		0.025
S		0.010
N		0.012
Cu		0.30[3)]
Cr		0.30
Ni		0.30
Mo	0.25	0.35

1) Heat analysis

2) The Al-content of the melting is to determine and to indicate in the certification.

3) A lower Cu-content and a maximum tin content may be agreed in the order, e. g. with respect to formability.

Mechanical properties[4)]

Nom. thick. e in mm	Yield strength R_{eH} in MPa
≤ 16	≥ 275
> 16	≥ 270

Tensile stength R_m in MPa
440 - 590

Total elongation A in %
≥ 22

Temperature in °C	Notch impact energy[5)] in J
+ 20	≥ 31
0	–[6)]
- 20	–[6)]

Test temperature in °C	Yield point at elev. temp. $R_{p0,2}$ in MPa ≤ 16 mm	> 16 mm
50	≥ 273	≥ 268
100	≥ 264	≥ 259
150	≥ 250	≥ 245
200	≥ 233	≥ 228
250	≥ 213	≥ 209
300	≥ 194	≥ 190
350	≥ 175	≥ 172
400	≥ 159	≥ 156
450	≥ 147	≥ 145
500	≥ 141	≥ 139

4) Transverse samples, normalised

5) Average values of 3 samples; one individual value may fall short of the required minimum value by not more than 30 %. The sample width shall equal the product thickness if the latter is between 6 and 10 mm. The tests are performed by using samples similar to Charpy-V samples. The values specified in the table above are to be reduced proportionally to the sample width.

6) A value can be agreed on in the request and order.

Welding

The steel grades of this series may be welded by means of the usual welding techniques.

Condition of delivery, scope of testing and certificate

The provisions of DIN EN 10028-2, chapters 8.2 and 9 shall apply for delivery and inspection. The steel grade 16Mo3 is delivered in the as-rolled condition; the test is carried out on simulating heat treated samples (normalised).

Test certificates according to DIN EN 10204 can be supplied as follows: EDP, remote data transmission, fax, e-mail, paper.

SALZGITTER FLACHSTAHL
A Member of the Salzgitter Group

Salzgitter Flachstahl GmbH / Eisenhüttenstraße 99 / 38239 Salzgitter
PHONE +49 (0) 53 41 21 28 90 / FAX +49 (0) 53 41 21 85 36 / MAIL flachstahl@salzgitter-ag.de
www.salzgitter-flachstahl.de

Attachement 2 1/1

Chemical compostion of AX 625

ALUNOX
welding alloys group

AX-625
AX-2.4831

EN ISO 18274	S Ni 6625 (NiCr22Mo9Nb)
Werkstoff-Nummer	2.4831
AWS A5.14	ERNiCrMo-3

Anwendungsgebiet
Schweißstab/Drahtelektrode aus Nickel-Chrom-Molybdän-Legierung zum WIG - bzw. MAG-Schweißen von artgleichen und artähnlichen Nickellegierungen, kaltzähen Nickelstählen und artverschiedenen Verbindungen für Betriebstemperaturen bis 1000°C; kaltzäh bis -196°C.

Besondere Hinweise
Sauberkeit des Werkstückes im Schweißnahtbereich ist Voraussetzung für eine rissfreie Verbindung.
Bei dünnen Blechen und bei Wurzelschweißungen ist Unternahtschutz erforderlich. Bei V- und X- Nähten sollte der Öffnungswinkel mindestens 70° betragen. MIG – Drahtelektrode bevorzugt im Impulslichtbogen verschweißen.
Wegen Versprödungsgefahr zwischen 600 und 850°C ist dieser Temperaturbereich zu vermeiden.

Zusammensetzung des Schweißstab/Drahtelektrode (Richtwerte in %)

Ni	C	Cr	Mo	Mn	Si	Nb+Ta	Fe
Bal.	0,02	22	9,0	0,2	0,2	3,3	1,5

Wichtige Grundwerkstoffe
Nickel-Chrom-Molybdän-Legierungen, z.b. NiCr 22 Mo 9 Nb (2.4856), NiCr21Mo (2.4858), NiCr22Mo6Cu (2.4618), NiCr22Mo7Cu (2.4617), X1NiCrMoCuN25-20-7 und ihre Verbindungen mit un-, niedrig- und hochlegierten Stahl/Stahlguß sowie für korrosionsbeständige Plattierungen. Kaltzähe Nickelstähle, z.B. X8Ni9 (1.5662) und Schwarz-Weiß-Verbindungen für Betriebstemperaturen über 300°C.

Inconel 625, NiCrofer 4221hMo, Hastelloy G, Hastelloy G3, Incoloy 800, UNS N06625, UNS N08825, UNS N08926, UNS N08904

Werkstoffeigenschaften

Schutzgas Wärmebehandlung Prüftemperatur	Argon unbehandelt 20°C	Mechanische Gütewerte des Schweißgutes nach EN ISO 15792-1
0,2%-Dehngrenze $R_{p0,2}$	[MPa]	500
Zugfestigkeit R_m	[MPa]	760
Dehnung A (L_0= 5d_0)%	[%]	35
Kerbschlagarbeit Av	[J]	110

Anwendbare Schutzgase (EN ISO 14175)
WIG: Argon I1, MAG: M12 (Ar+30%He+0,5%CO_2), Ar+28%He+2%H_2+0,05%CO_2

Zulassung
(Aktuellen Umfang bei Bedarf anfordern)

Lieferformen

Spulen	Ø mm	0,8	1,0	1,2	1,6
Stäbe	Ø mm x 1000mm	1,6	2,0	2,4	3,2

Weitere Abmessungen auf Anfrage

Stand 02/2013

Attachement 3 1/1

Welding procedure specification – WPS

VUT FSI BRNO	WPS	Welding Procedure Specification specifikace svařovacího postupu	pWPS No./Č.: WPS-0001 Rev.: 0 Date/Datum: 20.4.2023 Pg./Str.: 1/1

Welding Process/Metoda: 1: 135 2:
Type of Weld/Typ svaru: BW
Backing/Podkladka: N.A.
Other/Ostatní:
Mark/ Označení značkl: 1-2

Supporting/Související WPAR:
Aplikační/Aplikace:

Base metal / Základní materiál:

Material 1:	16Mo3	Group/Sk.:	1	Thickness/Tloušťka:	7	mm	Outside Dia./Vnější ø:	35 mm
and/A Material 2:	N.A.	Group/Sk.:	1	Thickness/Tloušťka:	7	mm	Outside Dia./Vnější ø:	35 mm

Remark/Poznámka: EN 10028-2

Filler Material / Svařovací materiál:
Classification: 1: EN ISO 18274 2:
Klasifikace:
Designation: 1: ALUINOX AX-826 2:
Označení:
Size/Průměr: 1: 1,0 mm 2: mm
Name-Type of Flux/Jméno-typ tavidla: N.A.
Drying of F.M./Sušení svař. mat.: 1: N.A. 2:
Replace/Náhrada: 1: 2:
Remark/Poznámka:

Gas / Plyn:

		%	l/min	%	l/min
Shielding/O. svaru:	1: Cronigon NI10	15	2:		
Backing/O. kořene:	1: N.A.	N.A.	2:		
Trailing/Dodatečná:	1: N.A.	N.A.	2:		

Remark/Poznámka: I3 with ČSN EN ISO 14175

Position / Pozice:
Groove/Do žlabu: 1: PG 2:
ČSN EN ISO 6947

Welding Sequences / Postup svařování:

Joint Design / Tvar spoje:

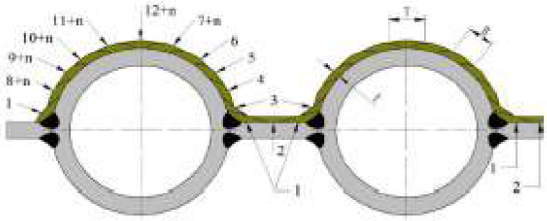

Preheat / Předehřev:

Preheat Temp./Teplota předehřevu:	Interpass:	Post Heating/Dohřev:	Cooling After W./Ochlazení po svař.:	Temp. Control/Kontrola teploty:	Remark/Poznámka:
N.A. °C	max.160 °C	N.A. °C h	still air klidný vzduch		

Post Weld Heat Treatment / Tepelné zpracování po svařování:

Type/Typ:	Temperature/Teplota:	Time/Čas:	Heating Rate/Rychlost ohřevu:	Cooling Rate/Rychlost ochlazování:	Remark/Poznámka:
	°C	min.	°C/h	°C/h	

Technique / Technika svařování:
Tungsten EL/Wolframová elektroda: 1: N.A. mm Type -
Edge Preparation/Příprava žlabu: N.A.
Method of Cleaning/Metoda čištění: mechanical / mechanicky
Method of Back Gouging/Drážkování kořene: N.A.
Remark/Poznámka:

Type of Bead/Tvar housenky: 1: string - rovná 2:
Weaving / Kyvadlo: 1: YES 2:
Pulsing/Pulzace: 1: N.A. 2:
Oscillator/Oscilace: 1: N.A. 3:

Welding Parameters / Svařovací parametry:

Layer(s) / Vrstva	Process / Metoda	Filler Material/Svařovací materiál: ø (mm)	Class/Označení/Klasifikace	Type/Polarity / Typ /Polarita	Amperage/Proud (A)	Voltage/Napětí (V)	Wire speed (m/min) / Rychl. drátu (m/min)	Travel Speed (cm/min) / Rychlost posuvu (cm/min)
1	135	1,0	ALUINOX AX-826	DC/+	180	17	8,4	26,7
2 - n	135	1,0	ALUINOX AX-826	DC/+	180	17	8,4	26,7

Remarks / Poznámky:

Tack welding shall be performed accordance with WPS.
Not Peening during and after welding.

Prepared (Name, Date, Signature):
Připravil (jméno, datum, podpis): Bc. Daniel Chrást 20.4.2023

Approved (Name, Date, Signature):
Schválil (jméno, datum, podpis): Ing. Jaroslav Kubíček, IWE

Attachement 4 1/2

Technical specification of ARL ISpark

thermoscientific

TECHNICAL SPECIFICATIONS

Optical Emission Spectrometer

ARL iSpark Series

The Thermo Scientific™ ARL iSpark™ Series is a high-performance optical emission spectrometer platform based on the famous Thermo Scientific one-meter vacuum PMT optics and innovative technologies. The ARL iSpark Series answers the needs of the different market segments of the metallurgy and brings an optimum solution for everyone. If offers high accuracy, sensitivity, precision, stability and reliability.

PMT optics

- One meter Paschen-Runge mounting vacuum spectrometer
- Special cast iron body, temperature controlled at 36 °C ±0.1 °C
- Primary optics: heated focusing lens made of MgF_2, CaF_2 or fused silica, depending on application
- Ruled gratings: 1080, 1667 or 2160 grooves/mm, appropriately selected for the analytical task
- Primary slit width: 20 µm
- Secondary slit width: 25, 37.5, 50 or 75 µm
- Up to 80 photomultiplier tubes (PMT) detectors
- PMTs: Ø 28 mm, side-on-type, 10-stage, windows: MgF_2, UV glass, borosilicate glass or synthetic silica appropriately selected for the specific wavelength
- Wavelength range depending on grating and diffraction order, selected for optimum resolution and sensitivity
- Diffraction order selective filters in front of PMTs for gratings with 1080 and 1667 grooves/mm

Spark stand

- Stand cover with ergonomic design for easy operation with maximal operator security
- Maximal sample size: 250 mm width x 250 mm depth x 150 mm height, maximal weight 10 kg

ThermoFisher SCIENTIFIC

Attachement 4 2/2

Technical specification of ARL ISpark

- Sample clamp with ergonomic design
- Wear-resistant stainless steel analysis table with quick fastening system; no tools needed for assembly and dismantling
- Design allowing argon savings and reduced maintenance
- Smart Argon Management (SAM) with programmable argon flows and argon saving ECOmode
- Argon flows can be different for each phase of the analytical sequence (flush, pre-burn, integration). Optimized for each application, between 2 to 5 l/min (typically 3 l/min) in analysis and 0.4 /min in stand-by requiring the minimum argon consumption
- Argon pulses after analysis for improved dust evacuation and instrument autonomy
- Electrode: Ø 1.4, 4 mm or pin electrode according to application; 3 mm analytical gap

Control electronics

- Instrument master control board (IMC) controlling all spectrometer functions, data flows and communication with OXSAS analytical software

Spark generator

- intelliSource, current controlled, double current source (i.e. a double CCS) for high shape flexibility and reproducibility
- Vectored spark shape definition, up to 200 A and 2500 µs single spark duration
- Spark short-circuit (DISC) to improve spark repeatability

Acquisition electronics and algorithmics

- Programmable high voltage settings: -300 to -1000 V for each channel
- For each channel:
  - Very low noise time gated differential integrator allowing PMT dark current and electronic offset subtraction
  - TGA (Time Gated Acquisition), a ultrahigh precision (100 ns) TRS from 2 to 6000 µs
  - ADC bit depth: 20 bits
  - SSA (Single Spark Acquisition) and storage
  - FAST (Flexible Acquisition STart/stop) algorithm, for usage of optimal single sparks subsets
- DISIRE (DIffuse Spark Intensity REmoval) algorithm for improved accuracy
- Spark-DAT methods for determination of soluble/ insoluble concentration and for inclusion analysis

Vacuum system

- Rotary pump for wavelength range down to 170 nm with speed control for reduced electrical consumption
- Membrane pump combined with molecular pump for operation down to 119 nm

Dimensions and weight

- Dimensions: 1750 m length x 860 m width x 1200 m height (inches: 68.9 x 33.9 x 47.3)
- Weight: approx. 500 kg net (1100 lbs), 570 kg with pallet (1260 lbs)

Requirements

- Ambient temperature: 16-30°C (62-86°F); maximum rate of change ±5°C/hour
- Relative humidity: 20-80%
- Voltage 230 V (+10% to -15%), single-phase with protective ground (2.5 kVA regulator required if fluctuations exceed +10%)
- Current: 10A, including PC, screen and printer
- Frequency: 50 or 60 Hz
- Grounding: < 1 Ohm
- Argon: > 99.998% maximum 5 ppm oxygen (maximum 2 ppm oxygen for samples with high Si content). Optional argon purifier available and recommended for low carbon analysis. For VUV lines (carbon, nitrogen, oxygen, chlorine, hydrogen), argon purifier recommended

Consumption

- Electrical power: 1 kVA
- Argon: typically 3 l/min. during analysis, 0.4 l/min in stand-by and down to 0 l/min in ECOmode

Compliance to norms

- 2006/95/EC: Low Voltage Directive (LV)
- 2004/108/EC: Electromagnetic compability (EMC)
- 2011/65/EU: Restriction of the use of certain Hazardous Substances in Electrical and Electronic Equipment (RoHS)
- 2012/19/EU: Waste Electrical and Electronic Equipment (WEEE)

Find out more at **thermofisher.com/ispark**

ThermoFisher SCIENTIFIC

Attachement 5 1/2

Chemical composition of welded layer

Run Info																							
Element		Ni%	C	Si	S	P	Mn	Cr	Mo	V	Cu	W	Ti	Co	Al	B	Nb	Ta	Mg	Fe	Sn	Zr
Channel		Matrix	C02_1	Si01_1	S01_1	P01_1	Mn03_1	Cr05_1	Mo04_1	V03_1	Cu08_1	W07_1	Ti03_1	Co01_1	Al07_2	B01_1	Nb07_1	Ta04_1	Mg01_1	Fe07_1	Sn02_2	Zr03_1
Type		MTX	INS	INS	INS	INS	INS	INS	INS	INS	INS	INS	INS	INS	INS	INS	INS	INS	INS	INS	INS	INS
Unit		%	%	%	%	%	%	%	%	%	%	%	%	%	%	%	%	%	%	%	%	%
Run 1	2	60,33067	0,03239	0,08589	0,00335	0,00452	0,05035	20,42642	8,57455	0,01591	0,02194	0,01688	0,17338	0,01852	0,05123	0,00204	3,32614	0,01596	0,01013	6,83676	0,00375	-0,00074
Run 2	2	60,6525	0,03381	0,08829	0,00349	0,00456	0,04746	20,60028	8,66812	0,01602	0,02138	0,0178	0,17654	0,01926	0,04847	0,00206	3,38275	0,01539	0,01035	6,18857	0,00337	-0,00046
Run 3	2	60,18568	0,02959	0,08753	0,00333	0,00438	0,0501	20,515	8,57408	0,01594	0,02193	0,01667	0,1728	0,0189	0,05527	0,00204	3,3213	0,01574	0,01014	6,89661	0,00362	-0,00067
Grade High		0	0	0	0	0	0	0	0	0	0	0	0	0	0	0	0	0	0	0	0	0
Average		60,38962	0,03193	0,08723	0,00339	0,00449	0,0493	20,5139	8,60558	0,01596	0,02175	0,01711	0,17424	0,01889	0,05166	0,00204	3,34339	0,01569	0,01021	6,64065	0,00358	-0,00062
Grade Low		0	0	0	0	0	0	0	0	0	0	0	0	0	0	0	0	0	0	0	0	0
SD		0,238928	0,002149	0,001226	0,000085	0,000095	0,001601	0,086934	0,054161	0,000057	0,000319	0,000603	0,002016	0,000368	0,003421	0,000011	0,034164	0,000288	0,000123	0,392651	0,000193	0,000149
SD%		0,4	6,73	1,41	2,52	2,11	3,25	0,42	0,63	0,36	1,47	3,53	1,16	1,95	6,62	0,52	1,02	1,83	1,2	5,91	5,4	23,99
U(95 %)		0	0,004353	0,004487	0,000444	0,000423	0,003759	0,18808	0,119938	0,001347	0,001336	0,005001	0,005985	0,003099	0,00695	0,000197	0,068869	0,002737	0,000789	0,788298	0,003899	0,001126
Last SCT Value		0	0	0	0	0	0	0	0	0	0	0	0	0	0	0	0	0	0	0	0	0
Nom. SCT Value		0	0	0	0	0	0	0	0	0	0	0	0	0	0	0	0	0	0	0	0	0

Run Info																							
Element		Ni%	C	Si	S	P	Mn	Cr	Mo	V	Cu	W	Ti	Co	Al	B	Nb	Ta	Mg	Fe	Sn	Zr
Channel		Matrix	C02_1	Si01_1	S01_1	P01_1	Mn03_1	Cr05_1	Mo04_1	V03_1	Cu08_1	W07_1	Ti03_1	Co01_1	Al07_2	B01_1	Nb07_1	Ta04_1	Mg01_1	Fe07_1	Sn02_2	Zr03_1
Type		MTX	INS	INS	INS	INS	INS	INS	INS	INS	INS	INS	INS	INS	INS	INS	INS	INS	INS	INS	INS	INS
Unit		%	%	%	%	%	%	%	%	%	%	%	%	%	%	%	%	%	%	%	%	%
Run 1	2	57,86384	0,17899	0,0809	-0,01308	-0,00574	0,0203	30,15763	4,10392	0,00468	0,00447	-0,02635	0,33652	-0,01827	0,01912	0,00446	6,93577	-0,00848	0,01042	0,39297	-0,0015	-0,04058
Run 2	2	61,29415	0,02825	0,08643	0,00351	0,00438	0,04021	29,92084	8,75161	0,0161	0,01905	0,01673	0,1769	0,01949	0,05289	0,00205	3,41124	0,01388	0,01031	5,12892	0,00334	-0,00026
Run 3	2	61,76448	0,0266	0,08519	0,00363	0,00436	0,03675	21,10534	8,90109	0,01614	0,01801	0,01759	0,18113	0,0197	0,05137	0,00207	3,47747	0,01317	0,01043	4,26293	0,00257	-0,00001
Grade High		0	0	0	0	0	0	0	0	0	0	0	0	0	0	0	0	0	0	0	0	0
Average		60,63496	0,06491	0,08418	-0,00066	0,00174	0,03385	23,37448	7,60628	0,01321	0,01499	0,00569	0,21795	0,01006	0,04337	0,00265	4,30627	0,00783	0,0102	3,57665	0,00169	-0,01034
Grade Low		0	0	0	0	0	0	0	0	0	0	0	0	0	0	0	0	0	0	0	0	0
SD		1,857633	0,076061	0,002368	0,008283	0,004993	0,009143	4,524952	2,336885	0,005688	0,00703	0,021391	0,079068	0,018888	0,016208	0,001209	1,753328	0,010886	0,00037	2,153264	0,002169	0,020161
SD%		3,06	117,19	2,81	1258,74	286,39	27,01	19,36	30,72	43,05	46,88	375,86	36,28	187,7	37,37	45,71	40,72	138,94	3,63	60,2	128,28	195,01
U(95 %)		0	0,152124	0,006041	0,016572	0,009995	0,018392	9,050307	4,673859	0,011455	0,014112	0,043073	0,158211	0,037897	0,032437	0,002426	3,506671	0,021935	0,001054	4,306754	0,006378	0,040338
Last SCT Value		0	0	0	0	0	0	0	0	0	0	0	0	0	0	0	0	0	0	0	0	0
Nom. SCT Value		0	0	0	0	0	0	0	0	0	0	0	0	0	0	0	0	0	0	0	0	0

Run Info																							
Element		Ni%	C	Si	S	P	Mn	Cr	Mo	V	Cu	W	Ti	Co	Al	B	Nb	Ta	Mg	Fe	Sn	Zr
Channel		Matrix	C02_1	Si01_1	S01_1	P01_1	Mn03_1	Cr05_1	Mo04_1	V03_1	Cu08_1	W07_1	Ti03_1	Co01_1	Al07_2	B01_1	Nb07_1	Ta04_1	Mg01_1	Fe07_1	Sn02_2	Zr03_1
Type		MTX	INS	INS	INS	INS	INS	INS	INS	INS	INS	INS	INS	INS	INS	INS	INS	INS	INS	INS	INS	INS
Unit		%	%	%	%	%	%	%	%	%	%	%	%	%	%	%	%	%	%	%	%	%
Run 1	2	61,3683	0,02761	0,08618	0,00363	0,00438	0,03883	21,07113	8,7995	0,01632	0,01889	0,01766	0,17908	0,02032	0,06198	0,00208	3,43123	0,01351	0,0103	4,82574	0,00295	0,00038
Run 2	2	62,97691	0,02617	0,08679	0,00357	0,00462	0,03075	21,40265	8,99638	0,0164	0,01561	0,02022	0,18202	0,02054	0,05903	0,00213	3,50002	0,01211	0,0108	2,63178	0,00243	0,00008
Run 3	2	61,43635	0,0275	0,08828	0,00362	0,00452	0,04047	21,03529	8,79017	0,01648	0,01956	0,01912	0,17851	0,02041	0,05967	0,00211	3,42554	0,0141	0,01042	4,80485	0,00258	0,00044
Grade High		0	0	0	0	0	0	0	0	0	0	0	0	0	0	0	0	0	0	0	0	0
Average		61,92719	0,02676	0,08708	0,00361	0,00451	0,03668	21,16969	8,86201	0,0164	0,01802	0,019	0,17987	0,02042	0,06023	0,00211	3,45226	0,01324	0,01051	4,08746	0,00265	0,0003
Grade Low		0	0	0	0	0	0	0	0	0	0	0	0	0	0	0	0	0	0	0	0	0
SD		0,909724	0,001379	0,001077	0,000033	0,000118	0,005205	0,202542	0,116454	0,000084	0,002113	0,001288	0,001881	0,000112	0,001547	0,000023	0,041455	0,001018	0,000258	1,260698	0,00027	0,000155
SD%		1,47	5,15	1,24	0,9	2,62	14,19	0,96	1,31	0,51	11,72	6,78	1,05	0,55	2,57	1,08	1,2	7,69	2,45	30,84	10,19	64,59
U(95 %)		0	0,002844	0,004331	0,000415	0,000445	0,010593	0,411901	0,238654	0,001353	0,004392	0,005473	0,005848	0,003016	0,00337	0,000201	0,083375	0,003362	0,00091	2,52185	0,004247	0,00115
Last SCT Value		0	0	0	0	0	0	0	0	0	0	0	0	0	0	0	0	0	0	0	0	0
Nom. SCT Value		0	0	0	0	0	0	0	0	0	0	0	0	0	0	0	0	0	0	0	0	0

Run Info																							
Element		Ni%	C	Si	S	P	Mn	Cr	Mo	V	Cu	W	Ti	Co	Al	B	Nb	Ta	Mg	Fe	Sn	Zr
Channel		Matrix	C02_1	Si01_1	S01_1	P01_1	Mn03_1	Cr05_1	Mo04_1	V03_1	Cu08_1	W07_1	Ti03_1	Co01_1	Al07_2	B01_1	Nb07_1	Ta04_1	Mg01_1	Fe07_1	Sn02_2	Zr03_1
Type		MTX	INS	INS	INS	INS	INS	INS	INS	INS	INS	INS	INS	INS	INS	INS	INS	INS	INS	INS	INS	INS
Unit		%	%	%	%	%	%	%	%	%	%	%	%	%	%	%	%	%	%	%	%	%
Run 1	2	61,68052	0,02835	0,08737	0,00365	0,00455	0,03965	20,95618	8,81459	0,01616	0,0189	0,01894	0,17868	0,02001	0,05291	0,00211	3,42515	0,014	0,0106	4,62108	0,00275	-0,00016
Run 2	2	62,06836	0,02711	0,08475	0,00358	0,00451	0,03799	21,13841	8,72428	0,01628	0,01836	0,01793	0,1767	0,02005	0,05326	0,00206	3,39207	0,0135	0,01053	4,18559	0,00266	0,00003
Run 3	2	65,72688	0,05261	0,07738	-0,00048	0,00242	0,03399	19,79571	7,93551	0,01094	0,01139	-0,0074	0,25637	0,00586	0,04119	0,00184	3,44719	0,00971	0,00906	2,60152	0,00087	-0,01276
Grade High		0	0	0	0	0	0	0	0	0	0	0	0	0	0	0	0	0	0	0	0	0
Average		63,15858	0,03609	0,08317	0,00225	0,00383	0,03721	20,6301	8,49146	0,01446	0,01622	0,00982	0,20458	0,01531	0,04912	0,002	3,4228	0,0124	0,01006	3,80273	0,00209	-0,0043
Grade Low		0	0	0	0	0	0	0	0	0	0	0	0	0	0	0	0	0	0	0	0	0
SD		2,232645	0,014494	0,00518	0,002362	0,001221	0,002912	0,728327	0,48358	0,003048	0,004187	0,014925	0,044848	0,008179	0,006873	0,000141	0,028102	0,002343	0,000873	1,062824	0,00106	0,007332
SD%		3,53	40,16	6,23	104,99	31,88	7,83	3,53	5,69	21,08	25,82	151,93	21,92	53,43	13,99	7,02	0,82	18,88	8,68	27,95	50,62	170,59
U(95 %)		0	0,028997	0,011017	0,004741	0,002472	0,006146	1,458444	0,967738	0,006242	0,008462	0,030256	0,089821	0,016634	0,013799	0,000343	0,056879	0,005396	0,001901	2,126141	0,004947	0,014706
Last SCT Value		0	0	0	0	0	0	0	0	0	0	0	0	0	0	0	0	0	0	0	0	0
Nom. SCT Value		0	0	0	0	0	0	0	0	0	0	0	0	0	0	0	0	0	0	0	0	0

Run Info																							
Element		Ni%	C	Si	S	P	Mn	Cr	Mo	V	Cu	W	Ti	Co	Al	B	Nb	Ta	Mg	Fe	Sn	Zr
Channel		Matrix	C02_1	Si01_1	S01_1	P01_1	Mn03_1	Cr05_1	Mo04_1	V03_1	Cu08_1	W07_1	Ti03_1	Co01_1	Al07_2	B01_1	Nb07_1	Ta04_1	Mg01_1	Fe07_1	Sn02_2	Zr03_1
Type		MTX	INS	INS	INS	INS	INS	INS	INS	INS	INS	INS	INS	INS	INS	INS	INS	INS	INS	INS	INS	INS
Unit		%	%	%	%	%	%	%	%	%	%	%	%	%	%	%	%	%	%	%	%	%
Run 1	2	63,29475	0,04168	0,08865	0,00381	0,00414	0,03076	21,25673	9,01371	0,01776	0,01727	0,01874	0,18636	0,02149	0,05561	0,00212	3,49375	0,01153	0,01085	2,42753	0,00152	0,00123
Run 2	2	63,54925	0,05422	0,09035	0,0041	0,00405	0,02566	21,57282	9,26722	0,0179	0,01503	0,01815	0,19164	0,02218	0,05417	0,00216	3,62968	0,01061	0,01083	1,45686	0,0011	0,00202
Run 3	2	63,54066	0,06315	0,08326	0,00401	0,00377	0,02823	21,40937	8,9707	0,0179	0,01642	0,01579	0,18608	0,02177	0,05435	0,00208	3,41386	0,01106	0,01086	2,14283	0,0019	0,00195
Grade High		0	0	0	0	0	0	0	0	0	0	0	0	0	0	0	0	0	0	0	0	0
Average		63,46155	0,05302	0,08742	0,00397	0,00399	0,02822	21,41298	9,08388	0,01785	0,01624	0,01756	0,18803	0,02181	0,05471	0,00212	3,51243	0,01107	0,01085	2,00908	0,00151	0,00173
Grade Low		0	0	0	0	0	0	0	0	0	0	0	0	0	0	0	0	0	0	0	0	0
SD		0,14452	0,010786	0,003702	0,000146	0,000191	0,00255	0,158078	0,160231	0,000083	0,00113	0,001562	0,003131	0,000344	0,000784	0,000041	0,109116	0,000463	0,000017	0,498967	0,000401	0,000436
SD%		0,23	20,34	4,23	3,67	4,8	9,04	0,74	1,76	0,46	6,96	8,9	1,67	1,58	1,43	1,94	3,11	4,19	0,15	24,84	26,61	25,13
U(95 %)		0	0,021582	0,008303	0,000503	0,000544	0,005465	0,325102	0,324744	0,001353	0,002564	0,005767	0,007745	0,003082	0,002014	0,000212	0,218412	0,002832	0,000752	0,99857	0,004842	0,001386
Last SCT Value		0	0	0	0	0	0	0	0	0	0	0	0	0	0	0	0	0	0	0	0	0
Nom. SCT Value		0	0	0	0	0	0	0	0	0	0	0	0	0	0	0	0	0	0	0	0	0

Run Info																							
Element		Ni%	C	Si	S	P	Mn	Cr	Mo	V	Cu	W	Ti	Co	Al	B	Nb	Ta	Mg	Fe	Sn	Zr
Channel		Matrix	C02_1	Si01_1	S01_1	P01_1	Mn03_1	Cr05_1	Mo04_1	V03_1	Cu08_1	W07_1	Ti03_1	Co01_1	Al07_2	B01_1	Nb07_1	Ta04_1	Mg01_1	Fe07_1	Sn02_2	Zr03_1
Type		MTX	INS	INS	INS	INS	INS	INS	INS	INS	INS	INS	INS	INS	INS	INS	INS	INS	INS	INS	INS	INS
Unit		%	%	%	%	%	%	%	%	%	%	%	%	%	%	%	%	%	%	%	%	%
Run 1	2	62,11362	0,0925	0,08868	0,00486	0,00455	0,03566	21,36429	9,3186	0,01711	0,02758	0,01976	0,18953	0,02245	0,05075	0,00212	3,64959	0,01129	0,01198	2,98143	0,00161	0,00105
Run 2	2	62,6032	0,05026	0,08463	0,00372	0,0041	0,02932	21,61845	9,10097	0,01692	0,01951	0,01514	0,18453	0,02073	0,04854	0,0021	3,57988	0,01109	0,01014	2,59745	0,00125	0,00105
Run 3	2	62,51753	0,05173	0,08772	0,00396	0,00406	0,0286	21,77908	9,08168	0,01691	0,01675	0,0159	0,18431	0,02098	0,04869	0,00211	3,59697	0,01098	0,01003	2,5195	0,00134	0,00116
Grade High		0	0	0	0	0	0	0	0	0	0	0	0	0	0	0	0	0	0	0	0	0
Average		62,41145	0,06483	0,08701	0,00418	0,00424	0,0312	21,58727	9,16708	0,01698	0,02028	0,01694	0,18613	0,02139	0,04933	0,00211	3,60581	0,01112	0,01072	2,69946	0,0014	0,00109
Grade Low		0	0	0	0	0	0	0	0	0	0	0	0	0	0	0	0	0	0	0	0	0
SD		0,26146	0,023972	0,002112	0,000601	0,000271	0,003885	0,209148	0,131574	0,000112	0,006323	0,002476	0,002953	0,000928	0,001231	0,000013	0,031303	0,000155	0,001094	0,247284	0,000187	0,000061
SD%		0,42	36,98	2,43	14,38	6,41	12,45	0,97	1,44	0,66	31,17	14,62	1,59	4,34	2,5	0,64	0,87	1,4	10,21	9,16	13,4	5,64
U(95 %)		0	0,04795	0,005654	0,001271	0,000664	0,008013	0,425244	0,268383	0,001361	0,012701	0,006935	0,007448	0,003532	0,002737	0,000198	0,063255	0,002694	0,002314	0,496093	0,00485	0,001086
Last SCT Value		0	0	0	0	0	0	0	0	0	0	0	0	0	0	0	0	0	0	0	0	0
Nom. SCT Value		0	0	0	0	0	0	0	0	0	0	0	0	0	0	0	0	0	0	0	0	0

Run Info																							
Element		Ni%	C	Si	S	P	Mn	Cr	Mo	V	Cu	W	Ti	Co	Al	B	Nb	Ta	Mg	Fe	Sn	Zr
Channel		Matrix	C02_1	Si01_1	S01_1	P01_1	Mn03_1	Cr05_1	Mo04_1	V03_1	Cu08_1	W07_1	Ti03_1	Co01_1	Al07_2	B01_1	Nb07_1	Ta04_1	Mg01_1	Fe07_1	Sn02_2	Zr03_1
Type		MTX	INS	INS	INS	INS	INS	INS	INS	INS	INS	INS	INS	INS	INS	INS	INS	INS	INS	INS	INS	INS
Unit		%	%	%	%	%	%	%	%	%	%	%	%	%	%	%	%	%	%	%	%	%
Run 1	2	62,69007	0,02663	0,08728	0,00364	0,00459	0,03382	21,31772	8,89048	0,01667	0,01773	0,01978	0,18017	0,02063	0,05442	0,00212	3,47518	0,01288	0,01075	3,13331	0,00189	0,00024
Run 2	2	62,56494	0,0274	0,08752	0,00366	0,00458	0,03243	21,37565	8,94386	0,01672	0,0165	0,01967	0,18144	0,02062	0,05331	0,00212	3,51403	0,01251	0,01067	3,10992	0,00194	0,00051
Run 3	2	63,28595	0,02646	0,087	0,00377	0,00464	0,02903	21,54005	9,00288	0,01691	0,01534	0,0207	0,18252	0,02129	0,05341	0,00215	3,52182	0,01192	0,01091	2,16068	0,00166	0,0009
Grade High		0	0	0	0	0	0	0	0	0	0	0	0	0	0	0	0	0	0	0	0	0
Average		62,84699	0,02683	0,08727	0,00369	0,0046	0,03176	21,41114	8,94574	0,01677	0,01652	0,02005	0,18138	0,02084	0,05371	0,00213	3,50368	0,01243	0,01078	2,8013	0,00183	0,00055
Grade Low		0	0	0	0	0	0	0	0	0	0	0	0	0	0	0	0	0	0	0	0	0
SD		0,38527	0,000501	0,000261	0,00007	0,000035	0,002464	0,115333	0,056226	0,000126	0,001191	0,000565	0,001176	0,000382	0,000611	0,000019	0,024984	0,000483	0,000124	0,554921	0,000148	0,000328
SD%		0,61	1,87	0,3	1,88	0,76	7,76	0,54	0,63	0,75	7,21	2,82	0,65	1,83	1,14	0,88	0,71	3,89	1,15	19,81	8,1	59,62
U(95 %)		0	0,001219	0,003794	0,000432	0,000382	0,005303	0,242781	0,123995	0,001366	0,002672	0,004947	0,00507	0,003102	0,001749	0,000199	0,050749	0,002845	0,00079	1,110543	0,004611	0,001264
Last SCT Value		0	0	0	0	0	0	0	0	0	0	0	0	0	0	0	0	0	0	0	0	0
Nom. SCT Value		0	0	0	0	0	0	0	0	0	0	0	0	0	0	0	0	0	0	0	0	0

Attachement 5 2/2

Chemical composition of welded layer

	Run Info																					
Element		Ni%	C	Si	S	P	Mn	Cr	Mo	V	Cu	W	Ti	Co	Al	B	Nb	Ta	Mg	Fe	Sn	Zr
Channel		Matrix	C02_1	Si01_1	S01_1	P01_1	Mn03_1	Cr06_1	Mo04_1	V03_1	Cu08_1	W07_1	Ti03_1	Co01_1	Al07_2	B01_1	Nb07_1	Ta04_1	Mg01_1	Fe07_1	Sn02_2	Zr03_1
Type		MTX	INS	INS	INS	INS	INS	INS	INS	INS	INS	INS	INS	INS	INS	INS	INS	INS	INS	INS	INS	INS
Unit		%	%	%	%	%	%	%	%	%	%	%	%	%	%	%	%	%	%	%	%	%
Run 1	2	62,18244	0,02698	0,08623	0,00367	0,00462	0,03538	21,17198	8,80739	0,01673	0,01744	0,0194	0,17912	0,02047	0,05421	0,00211	3,43608	0,01326	0,01063	3,90895	0,00234	0,00056
Run 2	2	62,8489	0,02659	0,08733	0,00368	0,00453	0,03233	21,35984	8,92693	0,01679	0,01666	0,02015	0,18092	0,02068	0,05514	0,00213	3,47174	0,01252	0,01088	2,89997	0,00182	0,0005
Run 3	2	62,20309	0,0304	0,08706	0,00368	0,00469	0,03584	21,1535	8,84242	0,01669	0,01756	0,01973	0,18092	0,02042	0,05965	0,00212	3,46377	0,0133	0,01078	3,83122	0,00259	0,00057
Grade High		0	0	0	0	0	0	0	0	0	0	0	0	0	0	0	0	0	0	0	0	0
Average		62,41148	0,02799	0,08687	0,00368	0,00461	0,03452	21,22844	8,85891	0,01674	0,01722	0,01976	0,18032	0,02052	0,05633	0,00212	3,4572	0,01303	0,01075	3,54671	0,00225	0,00055
Grade Low		0	0	0	0	0	0	0	0	0	0	0	0	0	0	0	0	0	0	0	0	0
SD		0,378961	0,002092	0,000672	0,000005	0,000084	0,001906	0,114172	0,061452	0,000049	0,000489	0,000373	0,00104	0,000134	0,002905	0,000009	0,018714	0,000439	0,000117	0,561446	0,000391	0,000039
SD%		0,61	7,47	0,66	0,13	1,82	5,52	0,54	0,69	0,29	2,84	1,89	0,58	0,66	5,16	0,42	0,54	3,37	1,09	15,83	17,36	7,12
U(95 %)		0	0,004241	0,003927	0,00041	0,000412	0,004286	0,240312	0,133471	0,001346	0,001551	0,004877	0,004941	0,003019	0,005951	0,000197	0,038446	0,002816	0,000786	1,123754	0,004463	0,001084
Last SCT Value		0	0	0	0	0	0	0	0	0	0	0	0	0	0	0	0	0	0	0	0	0
Nom. SCT Value		0	0	0	0	0	0	0	0	0	0	0	0	0	0	0	0	0	0	0	0	0

	Ni	Cr	Mo	Ti	Nb	Fe
	63,29475	21,25673	9,01371	0,18636	3,49375	2,42753
	63,54925	21,57282	9,26722	0,19164	3,62968	1,45686
	63,54066	21,40937	8,9707	0,18608	3,41386	2,14283
	62,11362	21,36429	9,3186	0,18953	3,64059	2,98143
	62,6032	21,61845	9,10097	0,18453	3,57988	2,59745
	62,51753	21,77908	9,08168	0,18431	3,59697	2,5195
	62,69007	21,31772	8,89048	0,18017	3,47518	3,13331
	62,56494	21,37565	8,94386	0,18144	3,51403	3,10992
	63,28595	21,54005	9,00288	0,18252	3,52182	2,16068
	62,18244	21,17198	8,80739	0,17912	3,43608	3,90895
	62,8489	21,35984	8,92693	0,18092	3,47174	2,89997
	62,20309	21,1535	8,84242	0,18092	3,46377	3,83122
[%wt]	Ni	Cr	Mo	Ti	Nb	Fe
av	62,78287	21,40996	9,013903	0,183962	3,519779	2,764138
sd	0,520874	0,186678	0,156939	0,003878	0,075448	0,702649
rsd	0,829643	0,871919	1,741082	2,107909	2,143654	25,4202

	Ni	Cr	Mo	Ti	Nb	Fe
	60,33067	20,42642	8,57455	0,17338	3,32614	6,83676
	60,6525	20,60028	8,66812	0,17654	3,38275	6,18857
	60,18568	20,515	8,57408	0,1728	3,3213	6,89661
	61,29415	20,92084	8,75161	0,1769	3,41124	5,12892
	61,76448	21,10534	8,90109	0,18113	3,47747	4,26293
	61,6174	21,31413	8,66849	0,17727	3,40061	4,52179
	61,3683	21,07113	8,7995	0,17908	3,43123	4,82574
	62,97691	21,40265	8,99638	0,18202	3,50002	2,63178
	61,43635	21,03529	8,79017	0,17851	3,42554	4,80485
	61,58052	20,95618	8,81459	0,17868	3,42915	4,62108
	62,06836	21,13841	8,72428	0,1787	3,39207	4,18559
	65,72688	19,79571	7,93551	0,25637	3,44719	2,60152
[%wt]	Ni	Cr	Mo	Ti	Nb	Fe
av	61,75852	20,85678	8,683198	0,184282	3,412059	4,792178
sd	1,463556	0,450628	0,265835	0,022861	0,053173	1,378084
rsd	2,369804	2,160583	3,061492	12,40553	1,558381	28,75695

Attachement 6 1/4

Technical specification of SEM Apreo 2

thermoscientific

DATASHEET

Apreo 2 SEM

Unmatched versatility powered by ColorSEM Technology

Resolve gray areas with the Thermo Scientific Apreo 2 SEM, a high-performance field emission gun (FEG) SEM with unique, live elemental imaging and an advanced, automated optics system that enables you to focus on your research rather than microscope performance.

The Thermo Scientific™ Apreo SEM has earned a reputation for its versatility and high-quality imaging performance—even on magnetic or other traditionally difficult samples. The new Apreo 2 SEM improves upon the original by expanding its already impressive resolution specifications as well as adding a number of new features designed to make the power of the Apreo SEM's advanced capabilities even more accessible.

Multi-purpose labs see a wide spectrum of users looking to image an equally wide range of sample types. Typically, this would mean that users are required to navigate a range of alignments before acquiring data. The Apreo 2 SEM introduces SmartAlign Technology on a workhorse SEM platform. SmartAlign Technology virtually removes the need for user alignments. With the broad base of alignment automation covered, you can focus on obtaining data, as the system is always aligned and ready to image. Even with alignments covered via automation, fine tuning of the beam is typically required to obtain the best image. Enter FLASH technology. FLASH automates the fine-tuning process. With a few mouse movements, the Apreo 2 SEM will execute any necessary corrections to lens centering, the stigmators, and final focus of the image. Combining SmartAlign and FLASH Technologies means that even users new to electron microscopy can access the high-end performance of the Apreo 2 SEM.

Key benefits

All-round nanometer or sub-nanometer resolution performance on materials ranging from nanoparticles, powders, catalysts, and nanodevices to bulk magnetic samples, even at long (10 mm) working distances

Extreme flexibility for handling a wide range of sample types, including insulators, sensitive materials, or magnetic samples, and for collecting the data that matters most to your application

Less time spent on maintenance with an optics system that aligns itself (SmartAlign Technology)

Elemental information at your fingertips with ColorSEM Technology; live quantitative elemental mapping for unprecedented time to result and ease of use

Advanced automation including FLASH Technology for automatic image fine tuning, undo, user guidance, maps tiling, and stitching

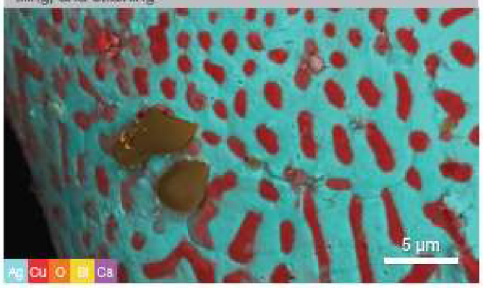

Microstructure of copper-silver alloy revealed with ColorSEM technology. Silicate contamination is immediately recognized when inspecting samples with live compositional imaging via ColorSEM.

ThermoFisher SCIENTIFIC

The Apreo 2 SEM's feature set also expands to analytical capability by integrating Thermo Scientific ColorSEM Technology into the main microscope UI. ColorSEM Technology integrates compositional mapping with the traditional imaging capabilities of the SEM. Once ColorSEM Technology is enabled, the result is an instant, colorized image showing the high-fidelity microstructural details overlain with compositional information in the same image. ColorSEM Technology improves the time to data for basic EDS information and makes moving to key areas of interest a quick trip rather than a long journey. The live color information is complimented by the addition of other conventional EDS functionality (point, line scan, area mapping, and reporting) directly integrated into the main UI. The result is an easy-to-use system that allows you to focus on discovery rather than manipulating multiple software packages.

The Apreo SEM's unique Trinity in-column detection system is present, but now with improved performance. The Apreo 2 SEM remains the platform of choice for research on nanoparticles, catalysts, powders, and nanodevices, thanks to its innovative final lens design that does not compromise on magnetic sample imaging performance. The electrostatic final lens (both Apreo 2 C and Apreo 2 S systems) enables simultaneous in-column detection at high resolution, while the Apreo 2 S SEM combines the electrostatic final lens with magnetic immersion into a compound lens. The compound final lens further boosts resolution performance, providing a resolution of 0.9 nm at 1 kV without additional beam deceleration, while offering unique options for signal filtering.

The Apreo 2 SEM ensures a short time to data with its T1 in-lens backscatter detector, which is positioned close to the sample to collect the maximum amount of signal. Unlike other backscatter detectors, this fast detector makes materials contrast available at all times, even when navigating, while tilted, or at short working distances. On sensitive samples, the detector provides clear backscatter images at currents as low as a few pA. The compound final lens on the Apreo 2 S SEM extends the possibilities of the T1 BSE detector even further, with energy filtering that enables more precise materials contrast as well as charge-free imaging of insulating samples.

Every Apreo 2 SEM comes standard with the widest range of features to address insulating samples, including high-vacuum techniques such as SmartScan mode, drift compensated frame integration (DCFI), and charge filtering. The Apreo 2 S SEM introduces PivotBeam mode, an integrated routine for inducing selected area channeling pattern (SACP) for orienting materials based on crystallography. PivotBeam mode is fully automated and available with a single click.

For the most challenging applications, the Apreo 2 SEM charge mitigation routines can include optional low vacuum (up to 500 Pa) to mitigate charge on any sample while providing excellent resolution and large analytical currents with field-proven through-the-lens differential pumping and dedicated LoVac detectors. The Apreo 2 S SEM with the low Vacuum (lowVac) option now comes standard with an automated routine to insert and remove the pressure limiting aperture (PLA). This allows you to focus on choosing the right conditions for imaging rather than stopping to manually adjust the system for lowVac imaging performance.

Additionally, the Apreo 2 SEM comes standard with a flexible chamber that accommodates up to three EDS/WDS ports for fast and sensitive X-ray measurements. It also features a coplanar EDS/EBSD/TKD arrangement and compatibility with (cryo) CL, Raman, EBIC, and other techniques.

All these capabilities are complemented by easy sample handling and the familiar xT user interface, saving time for novice and expert users alike. A customizable UI provides many options for user guidance, automation, and remote operation. With unique technologies like SmartAlign, FLASH, and ColorSEM Technology added to an already advanced microscope, the Apreo 2 SEM adds additional flexibility to any lab while providing advanced imaging capability for all users.

Electron optics

- High-resolution field emission SEM column with:
  - High-stability Schottky field emission gun to provide stable high-resolution analytical currents
  - Compound final lens: a combined electrostatic, field-free magnetic and immersion magnetic objective lens*
  - 60° objective lens geometry: allows tilting larger samples
  - Automated heated apertures to ensure cleanliness and touch-free aperture changes
- SmartAlign Technology: user-alignment-free technology
- Through-the-lens differential pumping for low vacuum* reduces beam skirting for the most accurate analysis and highest resolution
- Beam deceleration with stage bias from -4,000 V to +600 V
- Continuous beam current control and optimized aperture angle
- Double stage scanning deflection
- Easy gun installation and maintenance: auto bake-out, auto start, no mechanical alignments
- PivotBeam Mode for selected area electron channeling, also known as "rocking beam" mode (Apreo 2 S model only)
- Guaranteed minimum source lifetime: 24 months

Electron beam resolution

Model	Apreo 2 C	Apreo 2 S
Final lens	Electrostatic	Compound
High vacuum		
30 kV (STEM)	0.7 nm	0.7 nm
15 kV (BD)	0.9 nm	0.5 nm
15 kV (6.4 nA, WD 10 mm)		1.9 nm
1 kV	1.2 nm	0.9 nm
1 kV (BD)	1.0 nm	0.8 nm
1 kV (BD, WD 10 mm)		1.0 nm
500 V (BD)	1.2 nm	0.8 nm
200 V (BD)		1.2 nm
Low vacuum*		
3 kV (30 Pa)	1.8 nm	1.8 nm
15 kV (30 Pa)	1.2 nm	1.2 nm

BD: beam deceleration mode. WD: working distance. Resolutions are at optimum working distance unless specified otherwise. By default, upon final installation, the resolution is proven in the systems acceptance test at 1 kV and 30 kV in high vacuum and with immersion switched on if applicable.

Electron beam parameter space
- Beam current range: 1 pA to 50 nA (400 nA configuration also available)
- Accelerating voltage range: 200 V – 30 kV
- Landing energy range: 20 eV – 30 keV
- Max. horizontal field width: 3 mm at 10 mm WD (corresponds to 29x minimum magnification)

Chamber
- Inner width: 340 mm
- Analytical working distance: 10 mm
- Ports: 12
- EDS take-off angle: 35°
- Three simultaneous EDS detectors possible, two at 180°
- Coplanar EDS/EBSD orthogonal to the tilt axis of the stage

Detectors
The Apreo 2 SEM detects up to four signals simultaneously from any combination of the available detectors or detector segments*:

- Trinity Detection System (in-lens and in-column)
  - T1 segmented lower in-lens detector
  - T2 upper in-lens detector
  - T3 in-column detector*
- ETD—Everhart-Thornley SE detector
- DBS—Retractable segmented under-the-lens BSED*
- Low-vacuum SE detector*
- DBS-GAD—Lens-mounted gaseous analytical BSED*
- STEM 3+—Retractable segmented detector (BF, DF, HADF, HAADF)*
- IR-CCD
- Thermo Scientific Nav-Cam+™ Camera (chamber-mounted)

ColorSEM Technology*
ColorSEM Technology provides real-time quantitative compositional information by coloring the SEM image. ColorSEM Technology is based on energy dispersive X-ray spectroscopy (EDS) with reliable Noran quantification. Conventional EDS functions (point & ID, linescan, region, element maps) are included and can directly be applied to the SEM image.

- EDS detector size: 10, 30, or 60 mm^2
- Light element sensitivity down to beryllium
- 127 eV or 129 eV spectral resolution
- Optional motorized slide available
- Advanced mode with Pathfinder*

Vacuum system
- Complete oil-free vacuum system
- 1 × 240 l/s TMP
- 1 × PVP-scroll
- 2 × IGP
- Chamber vacuum (high vacuum) <6.3 × 10^{-6} mbar (after 12 hours pumping)
- Evacuation time: ≤3.5 minute
- Optional low-vacuum mode
- 10–500 Pa chamber pressure
- Automatic Pressure Limiting Aperture (PLA) Loader

Sample holders
- Standard multi-purpose holder uniquely mounts directly onto the stage, hosts up to 18 standard stubs (Ø12 mm), three pre-tilted stubs, cross-section samples, and two pre-tilted row-bar holders* (38° and 90°). Tools are not required to mount a sample.
- Each optional row-bar accommodates 6 S/TEM grids
- Wafer and custom holders*

Stage and sample	
Type	Eucentric goniometer stage, 5 axes motorized
XY	110×110 mm
Repeatability	<3.0 µm (@ 0° tilt)
Motorized Z	65 mm
Rotation	n × 360°
Tilt	-15° / +90°
Max. sample height	Clearance 85 mm to eucentric point
Max. sample weight	• 500 g in any stage position • Up to 5 kg at 0° tilt (some restrictions apply)
Max. sample size	122 mm diameter with full X, Y, rotation (larger samples possible with limited stage travel or rotation)

System control
- 64-bit GUI with Windows 10, keyboard, optical mouse
- 24-inch LCD display, WUXGA 1920×1200 (second monitor optional)
- Customizable graphical user interface, with up to 4 simultaneously active views
- FLASH automated image tuning for focus, lens align, and stigmator
- Image registration
- Navigation montage
- Image analysis software
- Undo / Redo functionality
- User guidance for basic operations / applications
- Optional joystick
- Optional manual user interface (knob board)

thermoscientific

Image processor
- Dwell time range from 25 ns to 25 ms/pixel
- Up to 6144×4096 pixels
- File type: TIFF (8-, 16-, 24-bit), JPEG or BMP
- Single-frame or 4-view image display
- SmartScan Mode (256-frame average or integration, line integration and averaging, interlaced scanning)
- DCFI (drift compensated frame integration) Mode
- Digital image improvement and noise reduction filter

Accessories (optional)
- Sample / chamber cleaning: CryoCleaner, Integrated Plasma Cleaner
- Analysis: EDS, EBSD, WDS, CL, Raman
- Thermo Scientific QuickLoader™ Load Lock for fast sample transfer
- Navigation: correlative navigation, Thermo Scientific Maps™ Software tiling and stitching
- Gas injection: up to 2 units (other accessories may limit number of GIS available) for beam-induced deposition of:
  - Platinum
  - Tungsten
  - Carbon
- Manipulators
- Cryo-stage
- Electrical probing / multi-probing stations
- Electrostatic beam blanker

Software options
- Maps Software for automatic large area acquisition using tiling and stitching; correlative work
- Thermo Scientific AutoScript™ 4 Software—Python-based application programming interface
- TopoMaps for image colorization, image analysis, and 3D surface reconstruction
- Advanced image analysis software
- Remote control software

Documentation
- Online user guidance
- Operating instructions handbook
- Online help
- Prepared for RAPID (remote diagnostic support)
- Free access to online resources for owners

Warranty and Training
- 1 year warranty
- Choice of service maintenance contracts
- Choice of operation / application training contracts

Installation requirements
(Refer to preinstall guide for detailed data)
- Power:
  - Voltage 100–240 V AC (-6%, +10%)
  - Frequency 50 or 60 Hz (±1%)
  - Consumption: <3.0 kVA for basic microscope
- Earth resistance <0.1 Ω
- Environment:
  - Temperature (20 ± 3)°C
  - Relative humidity below 80%
  - Stray AC magnetic fields <40 nT asynchronous, <100 nT synchronous for line times, 20 ms (50 Hz mains) or 17 ms (60 Hz mains)
- Minimum door size: 0.9 m wide × 1.9 m high
- Weight: column console 980 kg
- Dry nitrogen recommended for venting
- Compressed air 4–6 bar, clean, dry and oil-free
- System chiller
- Acoustics: site survey required, as acoustic spectrum relevant
- Floor vibrations: site survey required, as floor spectrum relevant
- Optional active vibration isolation table

Consumables (partial list)
- Replacement Schottky electron source module

* Optional

Find out more at **thermofisher.com/apreo**

ThermoFisher SCIENTIFIC

Attachement 7 1/3

Figures of structures of 16Mo3 and welded layer of Inconel 625

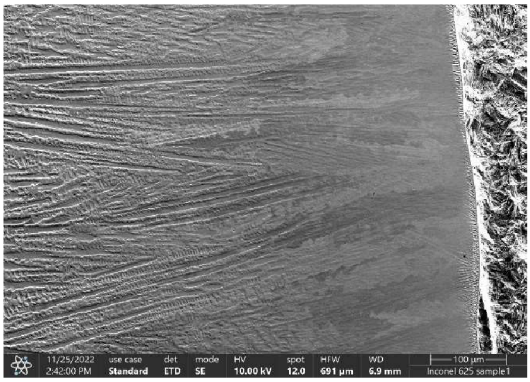

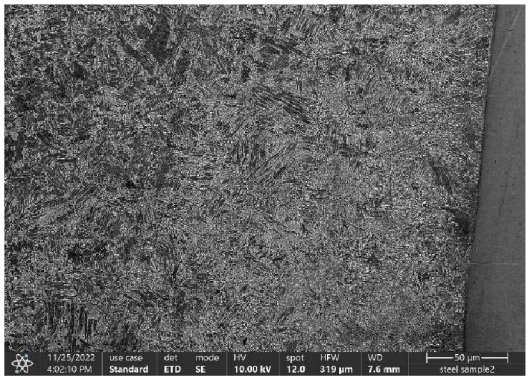

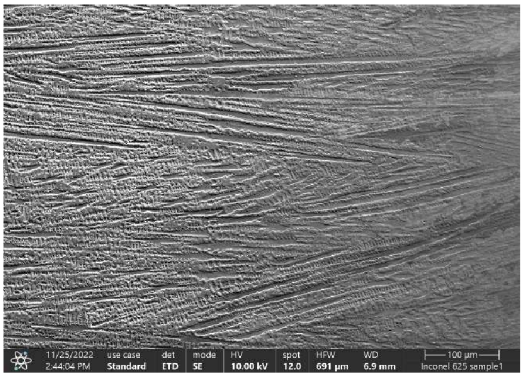

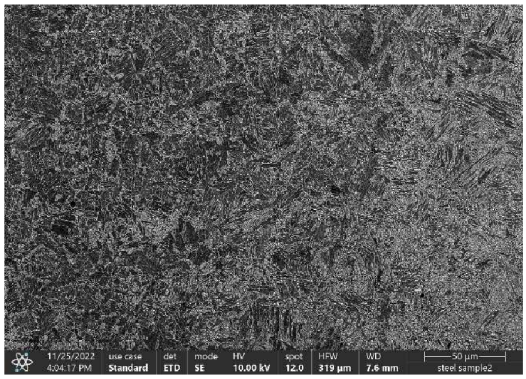

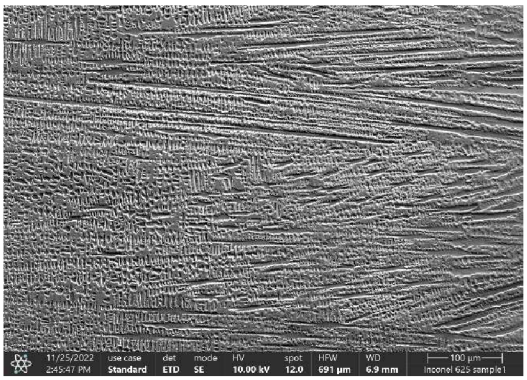

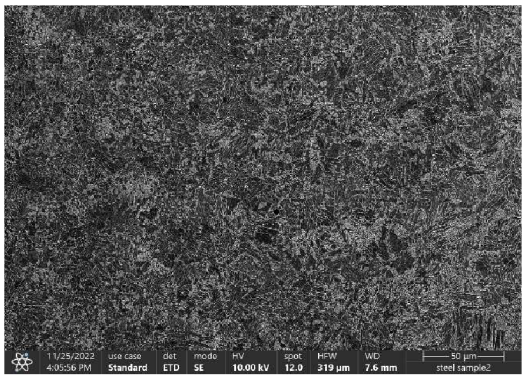

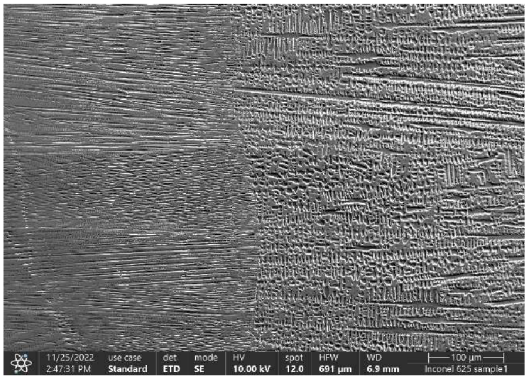

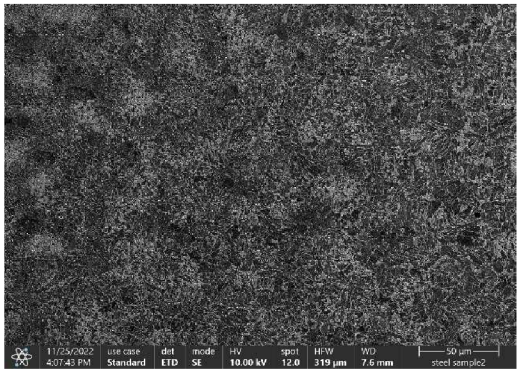

Attachement 7 2/3

Figures of structures of 16Mo3 and layer of Inconel 625

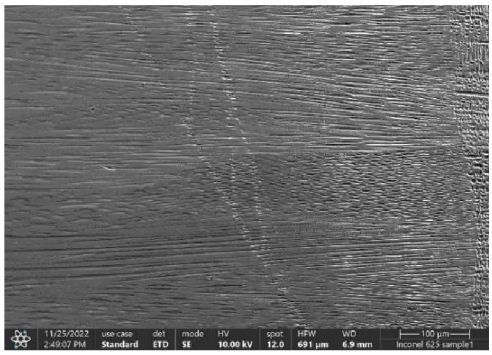

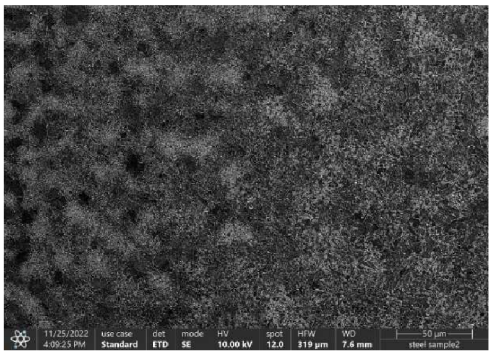

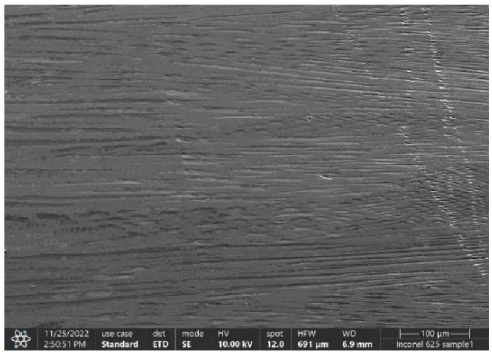

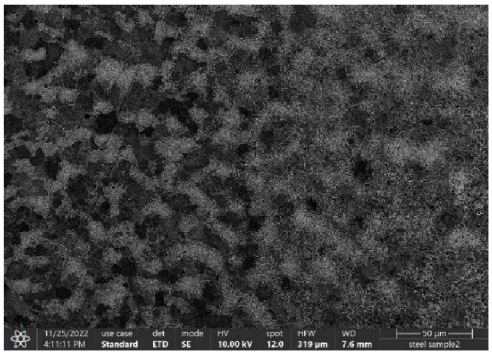

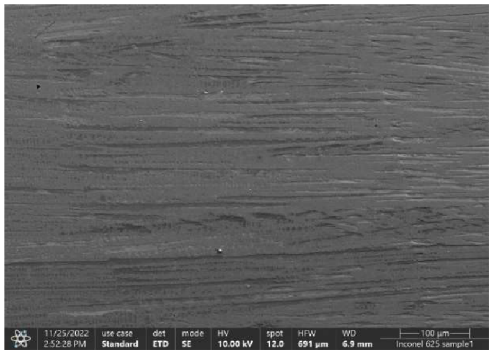

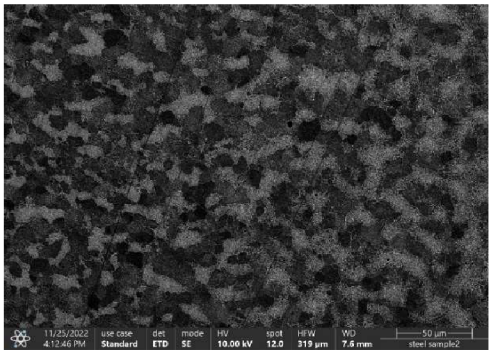

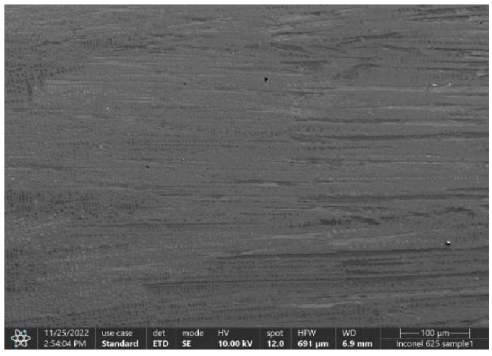

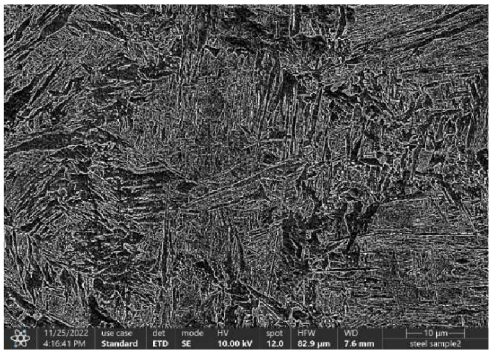

Attachement 7 3/3

Figures of structures of 16Mo3 and welded layer of Inconel 625

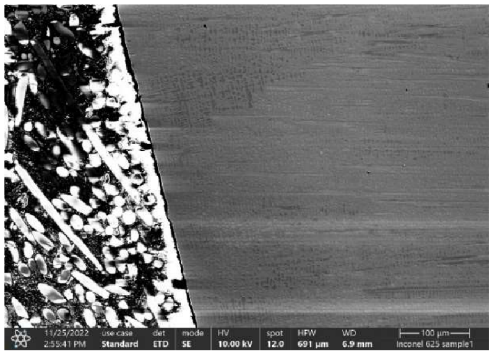
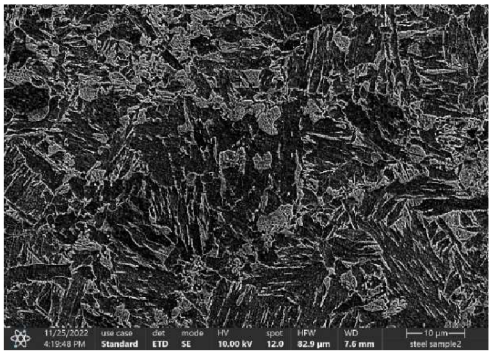
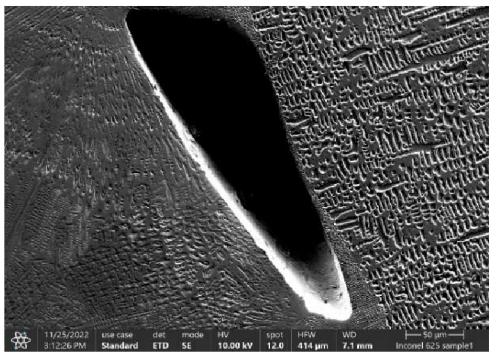
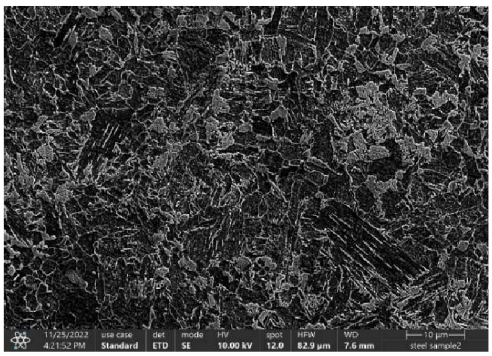
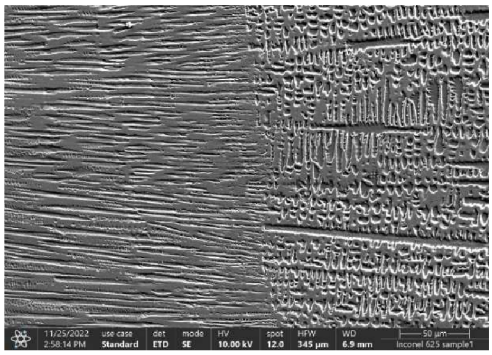
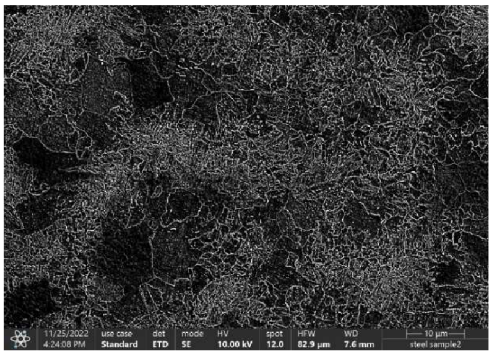
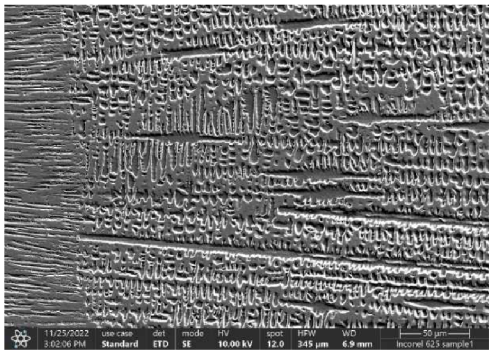
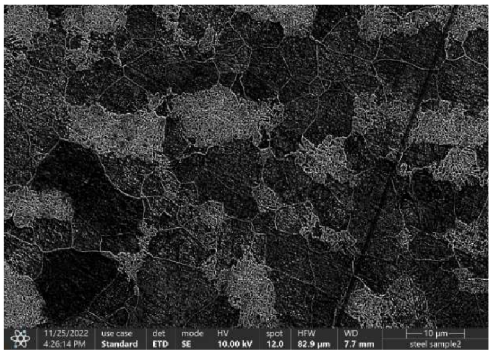

Attachement 8 1/5
Technical datasheet of LECO AMH55

AMH55 – Hardness Testing Systems

Maximise your productivity and easily measure impressions on various surface conditions for a wide number of applications with LECO's AMH55. The AMH55 introduces LECO's innovative CORNERSTONE® brand software to our hardness testing platforms, for increased usability, simplified reporting, and streamlined analysis times.

Supporting accurate and efficient microindentation and Macro/Vickers hardness testing in fully automatic, semi-automatic, and lite configurations, the AMH55 is a valuable resource for users needing precise and productive hardness testing while tailoring the data and results to their needs.

The AMH55 is ideal for:

Case Depth Analysis | Coating Hardness | Surface Analysis | Powdered Metals | Weld Profiles | Fasteners | Decarburisation

The AMH55 supports all standard loads for microindentation and Macro/Vickers hardness testing. The AMH55 conforms to ASTM E-384 for micro/macro hardness testing.

AMH55 Model Highlights and Features

Choose the model configuration that fits your needs. All models include our exclusive CORNERSTONE® brand software and the following functionality:

- Advanced image-recognition technology allows analysis of information not available with limited threshold-based methods
- Measures impressions with various surface conditions, including scratched or lightly etched

AMH55 Automatic

- Simultaneous automatic alignment and automatic parfocal tools
- Automatic pixel calibration
- Automatic shading correction
- Standard touch-screen interface with multi-touch capabilities
- Streamlined and simplified data reporting; customised spreadsheet generation tools
- Optional Advanced Analysis Module for color contoured mapping

AMH55 Semi-Automatic

- Automatically locates and analyses indents
- Automatic alignment
- Automatic pixel calibration
- Standard touch-screen interface with multi-touch capabilities
- Customisable data reporting
- Manual Focus
- Easily upgrade to AMH55 Automatic

AMH55 Lite

- Automatically locates and analyses indents within field of view
- Automatic pixel calibration
- Standard PC/monitor with keyboard and mouse interaction; optional touch-screen interface also available
- Customisable data reporting
- Easily upgrade to AMH55 Automatic or Semi-Automatic

Hardness Tester Options

The AMH55 supports all standard loads for microindentation and Macro/Vickers hardness testing.

LV-Series performs microindentations from 1 Kgf to 50 Kgf or 0.3 Kgf to 30 Kgf with Vickers, Knoop, or dual indenters.

LMV-50V Load Cell performs Macro/Vickers indentations from 10 gf to 50 Kgf.

Attachement 8 3/5
Technical datasheet of LECO AMH55

User-friendly CORNERSTONE® Brand Software

LECO's unique *Cornerstone* brand software sets the AMH55 apart from other automatic hardness testers. Designed through a collaboration of customer feedback and innovative engineering, *Cornerstone* gives the user complete control over their analysis parameters, method settings, calibrations, reporting, and more so that testing can be tailored to a specific application. A touch-screen interface and automatic software capabilities, such as simultaneous auto alignment and auto parfocal adjustment, deliver increased speed, ease-of-use, and repeatability to the analysis. Data output and reporting are simplified through *Cornerstone's* highly organised, immersive environment, which gives the user the ability to select the data conversions, method of testing, export options, report generation, and other settings that are best-suited for their samples.

Performing a Case Depth Analysis using the AMH55 Automatic

The AMH55 Automatic Micro/Macro Indentation Hardness Testing System combines the tasks of sample testing, measuring, converting, and documenting into one automated instrument operation. Just load the sample, select the indentation pattern(s), and initiate the test. This fully automated system makes the indentations, measures them, calculates their hardness, and then displays the results.

The AMH55 Semi-Automatic and Lite configurations offer the same great testing capabilities, but with less automatic functionality and features to meet your needs. Both can be easily upgraded to the fully Automatic version when the time is right.

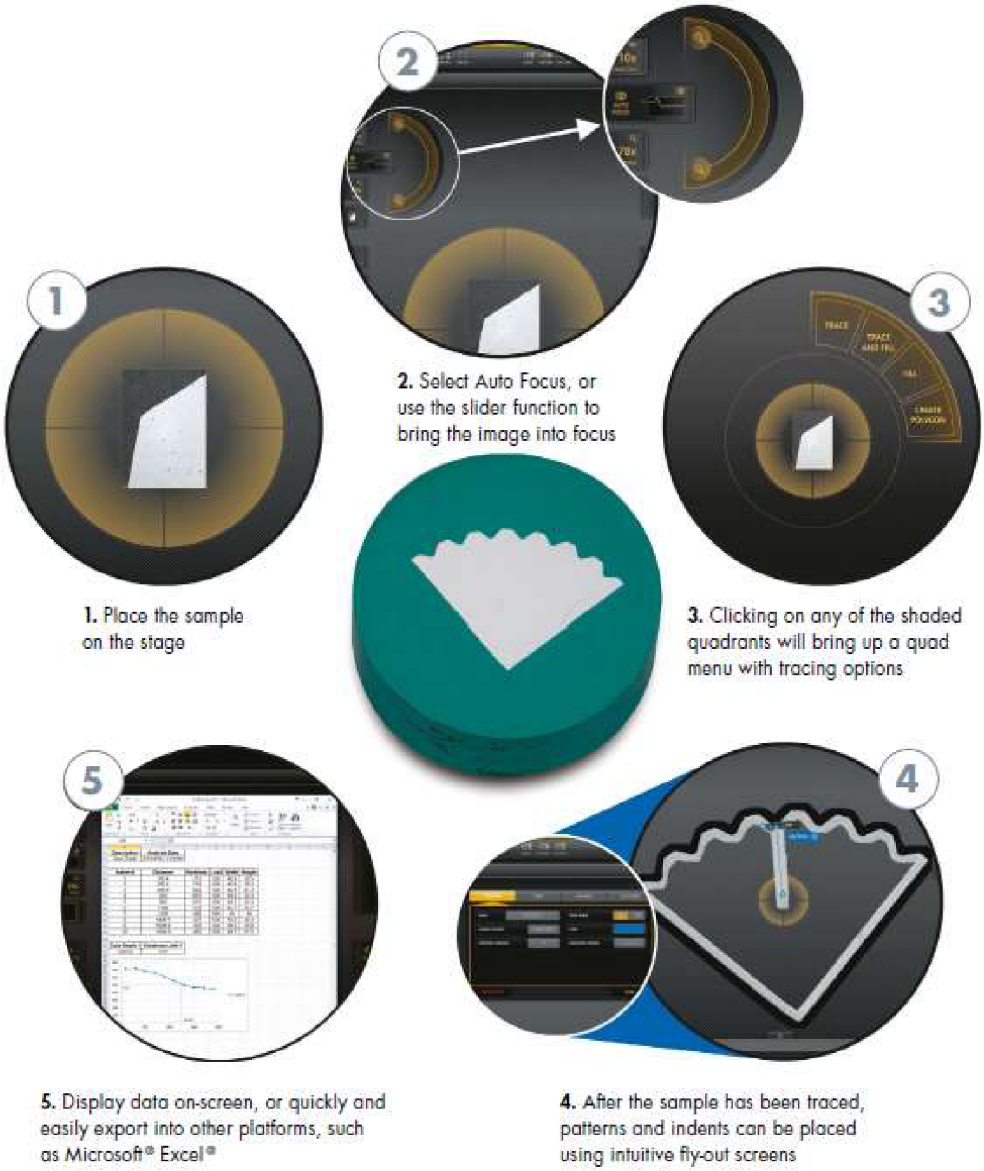

1. Place the sample on the stage

2. Select Auto Focus, or use the slider function to bring the image into focus

3. Clicking on any of the shaded quadrants will bring up a quad menu with tracing options

4. After the sample has been traced, patterns and indents can be placed using intuitive fly-out screens

5. Display data on-screen, or quickly and easily export into other platforms, such as Microsoft® Excel®

Package Configurations

Select one of the following hardness tester options with your AMH55 package.

LM110/310 Series Microindentation (refer to spec sheet 209-094-001)
LM248/810 Series Microindentation (refer to spec sheet 209-094-009)
LV110/810 Series Vickers (refer to spec sheet 209-094-002)
LMV-50V Load Cell Micro/Macro (refer to spec sheet 209-094-011)

Optional Advanced Analysis modules

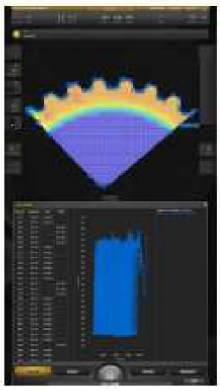

- Color Hardness/Contour Map (shown below)
- Auto Indent Placement
- Auto case depth

Optional Color Hardness Contour Map displays sample hardness and location with a color representation of hardness variances.

Options and Accessories

Stage Sample Holders

Anti-Vibration Table

Global Instrument Service & Support

We know that keeping your instrument running at optimal performance matters to you, which is why LECO instruments are assembled using the highest quality components and materials.

Sometimes downtime is unavoidable, however, and when that happens, our dedicated network of Global Service and Support technicians will help get you up and running as quickly as possible. Support is available at your facility or ours, by phone, and online.
Service and A2LA-accredited calibrations are also available for our LECO-supported optical equipment.
Visit our website for more information on how to access LECO Service:

eu.leco.com/contact/leco-contact-information

LECO Corporation
3000 Lakeview Avenue | St. Joseph, MI 49085
Phone: 269-985-5496
info@leco.com | www.leco.com

LECO Europe
eu.leco.com

LECO
EMPOWERING RESULTS

Form No. 209-246-EUW R1.53-RV1

Attachement 9 1/1
Technical datasheet of ZD40

Příloha č.1 Hydraulický zkušební stroj ZD40 /400kN/

Stroj umožňuje provádět tahové, tlakové a ohybové zkoušky materiálů do 400 KN s řízením rychlosti zatěžování a programovým zpracováním zkoušek. Je vybaven vestavěným inkrementálním délkovým snímačem polohy příčníku s rozlišením 0,01 mm a snímačem síly s řídící jednotkou EDC 60.

Řídící jednotka EDC 60 je vysoce precizní elektronické zařízení speciálně konstruované pro řízení servo-hydraulických zkušebních strojů. Je vyráběna speciálně pro aplikace řízení zkušebních strojů a využívají ji přední evropští výrobci universálních zkušebních strojů. Jednotka je opatřena programem pro zkoušky kovů s možností provádět zkoušky bez PC u jednoduchých aplikací bez použití průtahoměru.

Technické parametry:

- Výrobce: HBM /SRN/
- Měřící rozsah: 8 ÷ 400 kN
- Chyba měření síly: 1/100 jmenovitého rozsahu síly, tj. ± 1 % odpovídá třídě přesnosti 1
- Měřící rozsah měření dráhy: 0 ÷ 280 mm
- Chyba měření dráhy: ±0,01 mm
- sériové rozhraní RS 232 pro komunikaci s nadřazeným PC COM1 pro PC s FIFO s maximální rychlostí 115 KB
- inkrementální vstup pro napojení snímače dráhy

Počítač je vybaven programem TIRAtest v.2.1 pro tahovou, tlakovou a ohybovou zkoušku kovových materiálů dle EN 10 002 a EN ISO 6892 s vyhodnocením výsledků a grafickým zpracováním.

Řídící jednotka EDC 60

Attachement 10 1/2

Tensile diagrams of 16Mo3 and Inconel 625

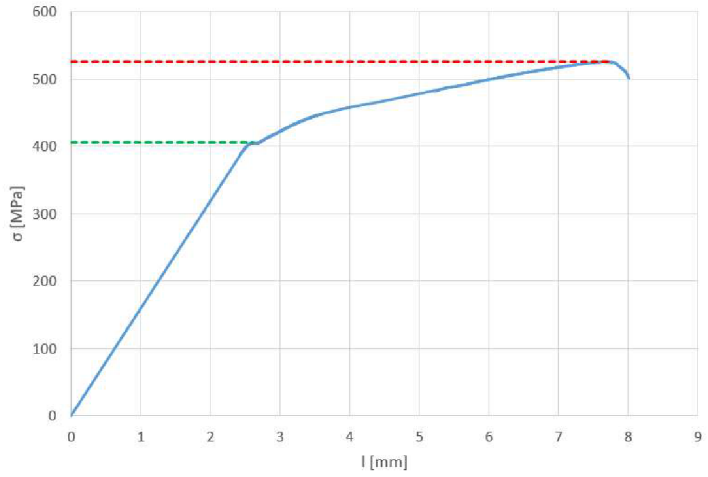

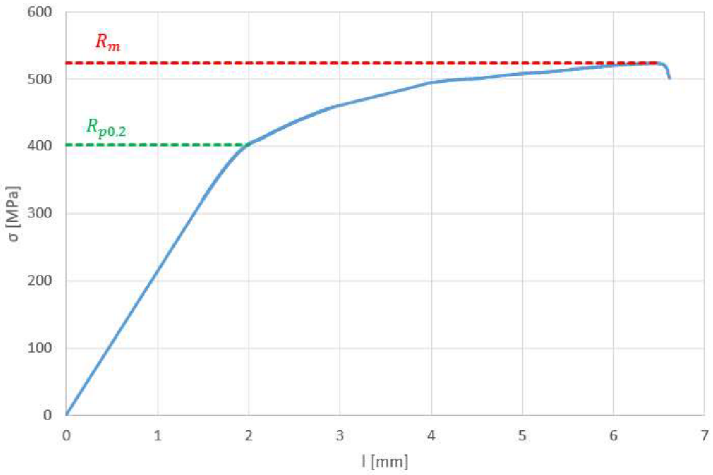

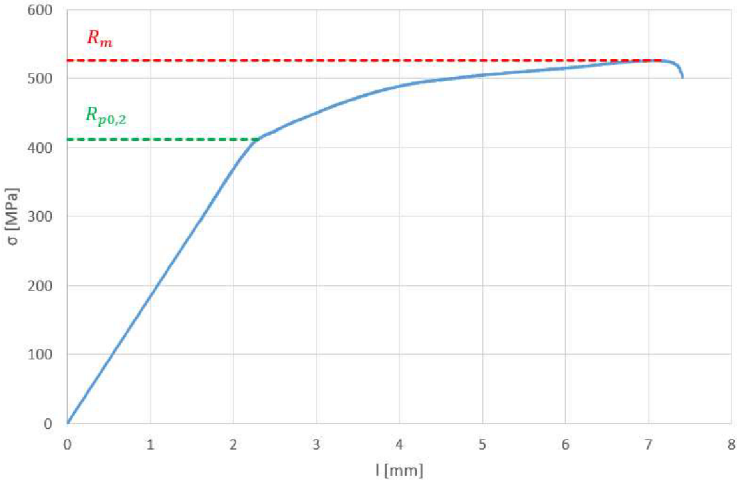

Attachement 10 2/2

Tensile diagrams of 16Mo3 and Inconel 625